

# Structure of atomic configurations and dynamic pathways in ion-conducting glass systems

Diplomarbeit

vorgelegt von

**Christian Müller**

Fachgebiet Theoretische Physik II

Institut für Physik

Fakultät für Mathematik und Naturwissenschaften

TU Ilmenau

Betreuer: Prof. Dr. Philipp Maaß

30. August 2007

## Abstract

Ion-conducting glasses are of great importance for many applications as, e.g. solid state batteries. A fundamental understanding of their conductivity mechanisms will support in the development of improved materials. For this purpose molecular dynamics (MD) and bond valence (BV) sum calculations are performed which both allow for a determination of diffusion paths of mobile ions in glasses. The BV method is tested against MD-simulations for a lithium silicate system and it turns out that it is not suitable to identify Li ion sites. However, it can determine parts of the diffusion paths of the mobile Li ions. It is also shown that this agreement with the MD-simulations originates mainly from hard-sphere constraints included in the BV scheme.

Density functional theory calculations of large LISON [ $\text{Li}_2\text{SO}_4(\text{N})$ ] and lithium metaborate [ $\text{Li}_2\text{O}-\text{B}_2\text{O}_3$ ] clusters are carried out in order to produce atomic configurations which are good representations of the local glass structure. These are evaluated by comparing calculated and measured vibrational spectra. Structural properties are discussed and a good agreement of calculated and measured spectra is achieved for various configurations. For the first time, it is revealed that nitrogen forms bridges between  $\text{SO}_3\text{N}^{2-}$  anions in the LISON clusters. It is likely that this mechanism is the underlying reason for the formation of the amorphous LISON thin films when sputtering lithium sulphate under a nitrogen atmosphere.

## Abstract

Ionenleitende Gläser haben für viele Anwendungen, wie beispielsweise Festkörperbatterien, eine grosse Bedeutung. Ein grundlegendes Verständnis ihrer Leitungsmechanismen unterstützt die Entwicklung verbesserter Materialien. Zwei Methoden, die dafür in den letzten Jahren verwendet wurden, sind Molekulardynamik (MD)-Simulationen und Bindungswalenz (BV)-Rechnungen, die beide eine Bestimmung von Diffusionspfaden der mobilen Ionen ermöglichen. Die Güte der BV-Methode ist mit Hinblick auf Gläser nicht klar, daher testen wir sie gegen MD-Simulationen von Lithium-Silikat-Gläsern. Es stellt sich heraus, dass die BV-Methode zwar ungeeignet ist um Li-Ionenplätze zu identifizieren, aber Teile des Diffusionspfades erfassen kann. Die teilweise Übereinstimmung von MD- und BV-Diffusionspfad beruht grösstenteils auf der Verwendung von Ausschlussradien um die Netzwerkatome. Zusätzlich werden Dichtefunktionalrechnungen von grossen LISON-  $[\text{Li}_2\text{SO}_4(\text{N})]$  und Lithium-Metaborat-  $[\text{Li}_2\text{O}-\text{B}_2\text{O}_3]$  Clustern durchgeführt, um molekulare Konfiguration zu erzeugen, die gute Repräsentanten lokaler Strukturen in Gläsern sind. Diese werden durch den Vergleich theoretischer und experimenteller Spektren evaluiert. Struktureigenschaften der Cluster werden untersucht und eine gute Übereinstimmung der verglichenen Spektren einiger Konfigurationen gezeigt. Erstmals wird gezeigt, dass Stickstoff in LISON Clustern Brücken zwischen  $\text{SO}_3\text{N}^{2-}$  Anionen ausbildet. Es ist wahrscheinlich, dass dieser Mechanismus verantwortlich ist für die Bildung einer amorphen LISON Dünnschicht beim Sputtern von Lithiumsulfat mit Stickstoff.

# Contents

<b>1</b>	<b>Introduction</b>	<b>1</b>
<b>2</b>	<b>Molecular dynamics simulations and bond valence sum calculations</b>	<b>5</b>
2.1	Molecular dynamics simulations . . . . .	5
2.1.1	Simulating glasses . . . . .	10
2.1.2	LAMMPS . . . . .	12
2.1.3	Setup of molecular dynamics simulations . . . . .	13
2.2	Determination of diffusion pathways and ion sites . . . . .	16
2.3	Bond valence sum calculations and BV path . . . . .	24
2.4	Comparison of MD and BV ion pathways . . . . .	29
<b>3</b>	<b>Raman spectroscopy on thin film salt glasses</b>	<b>35</b>
3.1	Basics of Raman spectroscopy . . . . .	35
3.2	Experimental procedure . . . . .	36
3.3	Results . . . . .	37
<b>4</b>	<b>Ab initio calculations</b>	<b>41</b>
4.1	Molecular orbital theory . . . . .	41
4.1.1	Hartree Fock . . . . .	43
4.1.2	PM3 . . . . .	46
4.1.3	Density functional theory . . . . .	49
4.1.4	Basis sets . . . . .	51
4.2	Simulating 'glass' cluster . . . . .	53
4.3	Creating glass cluster start configurations . . . . .	53
4.4	Calculation procedure . . . . .	55
4.5	Comparison of methods . . . . .	58
4.6	Evaluation of clusters by comparing vibrational spectra . . . . .	59
4.6.1	Li <sub>2</sub> SO <sub>4</sub> . . . . .	60
4.6.2	LISON . . . . .	63
4.6.3	Li <sub>2</sub> O-B <sub>2</sub> O <sub>3</sub> . . . . .	63
4.7	Structural properties . . . . .	65
4.7.1	LISON and the role of nitrogen . . . . .	65
4.7.2	Li <sub>2</sub> O-B <sub>2</sub> O <sub>3</sub> . . . . .	65
<b>5</b>	<b>Summary and Outlook</b>	<b>70</b>
5.1	Summary . . . . .	70
5.2	Outlook . . . . .	71
<b>A</b>	<b>List of clusters</b>	<b>73</b>
<b>B</b>	<b>References</b>	<b>74</b>

<b>C Publications and conference contributions</b>	<b>78</b>
<b>D Acknowledgment</b>	<b>79</b>
<b>E Erklärung</b>	<b>80</b>

## 1 Introduction

Fast ion conductors with room temperature ion conductivities up to  $10^{-2} \frac{1}{\Omega\text{cm}}$  have a wide range of applications. Examples are solid state batteries, electrochemical sensors and supercapacitors. There also exist crystalline electrolytes for such devices, but glassy materials have many advantages. As amorphous materials they are isotropic and their properties are not strongly affected by grain boundary effects. It is possible to tune their properties continuously by changing the composition, and glasses usually have a good workability. At temperatures lower than the glass temperature  $T_g$ , the conductivity in glasses in general follows an Arrhenius law:

$$\sigma_{\text{dc}}(T) = Ae^{-\frac{E_A}{k_B T}} \quad (1)$$

where  $E_A$  is the activation energy and  $k_B$  the Boltzmann constant. Variations in  $\sigma$  are usually due to variations of the activation energy  $E_A$ . For traditional glasses like borates and silicates typical values of  $E_A$  are usually larger than  $50 \text{ kJ mole}^{-1}$ . Several empirical rules are known how to lower  $E_A$  and hence increase the conductivity. One approach in oxide glasses is to increase the amounts of network modifier like  $\text{Li}_2\text{O}$  or  $\text{Na}_2\text{O}$ .

With respect to conductivity features there are two key effects which are not only interesting for their possible technical applications, but also pose a challenging problem from basic research's point of view. The first one is the so-called mixed alkali effect (MAE). Whenever a second alkali species is added to an ion-conducting alkali glass, the conductivity drops rapidly below the conductivity measured for either of the two pure alkali glasses. As this effect must be strongly linked to the conductivity mechanisms of the glass itself, understanding it is directly coupled to an understanding of the ion transport mechanisms in glasses. The second effect is the counterpart to the MAE, the mixed network former effect. In the 1980s, it was discovered that mixing two network formers (while keeping the network modifier content constant) can increase the ion conductivity above the level of the two pure systems. This effect is observed in many solid electrolyte systems.

For more than 20 years thin film applications have been topic of research in which also less conductive glasses (with  $\sigma_{\text{dc}} \simeq 10^{-6} - 10^{-4} \frac{1}{\Omega\text{cm}}$ ) can be used. While nowadays most of the materials are fabricated using sol-gel methods, sputtering techniques offer some interesting new possibilities. They can extend the glass forming region of a material composition, which allows the fabrication of amorphous thin films where no corresponding bulk materials exist. This has recently been observed in the ternary  $\text{Li}_2\text{O-B}_2\text{O}_3\text{-Li}_2\text{SO}_4$  systems [1], where the sulfate content could be increased to amounts that would lead to crystallisation when preparing the glass by melt quenching. In fact, the borate component can be fully eliminated by sputtering a  $\text{Li}_2\text{SO}_4$  target in a nitrogen containing plasma, leading to an

---

amorphous material referred to as LISON [2]. With respect to the target material one could speak of a 'salt glass'. It is also found that sputtering in argon plasma does not lead to an amorphous film, indicating that nitrogen plays a crucial role for the glass forming ability. Indeed, it was shown that nitrogen is incorporated into the material [2] with a sulphur to nitrogen ratio of about 2:1. At present, it is not clear how the structure of these salt glasses is built up, in particular in which way the incorporation of nitrogen takes place and how this leads to a stabilisation of the amorphous structure.

While this is just one example of new glass systems, generally the range of possible glass compositions is very broad. Beside the classical oxide glasses, sulfide glasses as for example  $\text{Li}_2\text{S-P}_2\text{S}_5\text{-LiI}$  or  $\text{Li}_2\text{S-GeS}_2\text{-LiI}$  are rather common materials. But also  $\text{O}^{2-}$  and  $\text{S}^{2-}$  free glasses exist, as for example  $\text{AgCl-AgI-CsCl}$  or  $\text{CuCl-CuI-RbCl-KCl}$ . Some of these systems do not even exist in a comparable crystalline phase. Through this great variability glasses offer a lot of possibilities for innovation. The question arises how one can design materials for specific applications in a target-oriented fashion.

So far material design is primarily based on phenomenological models and the knowledge of some general trends in glass systems. A quantitative understanding of the involved processes does not yet exist, although some qualitative (mostly phenomenological) models have been developed. The reason that glass sciences lack a detailed quantitative transport theory is that already basic components of a transport model are hard to define in amorphous materials. In contrast to crystalline materials there exist no well defined ion sites, traps, or defects in glasses. In fact, already detailed structure models are rare, as common experimental methods of structure analysis do not work well on amorphous systems.

It is necessary to develop new methods, in order to extend the existing phenomenological models based on hopping motion in disordered systems, to gain quantitative and material specific descriptions of transport mechanisms [3]. Currently research is under way to develop such models based on molecular dynamics (MD) simulations. Most of this work concentrates on silicate glasses, as these have seen the most comprehensive investigations regarding their structure during the last three decades, and the available MD potentials are well tested. During the last five years, some progress has been made in defining sites and diffusion paths in such systems [4, 5, 6, 7, 8, 9, 10], but the process of concept formulation is not yet finished.

Another approach to characterise diffusion paths and ion sites in glasses is based on a combination of reverse Monte-Carlo (RMC) simulations and bond valence (BV) calculations. RMC simulations are used to produce glass network configurations which are in agreement with neutron diffraction data. Then diffusion paths and ion sites in the host network are determined through BV calculations and investigated in order to gain insight into the transport mechanisms [11, 12, 13, 14]. So far, this was done without any evaluation of the quality of the diffusion paths. In the first part of this work

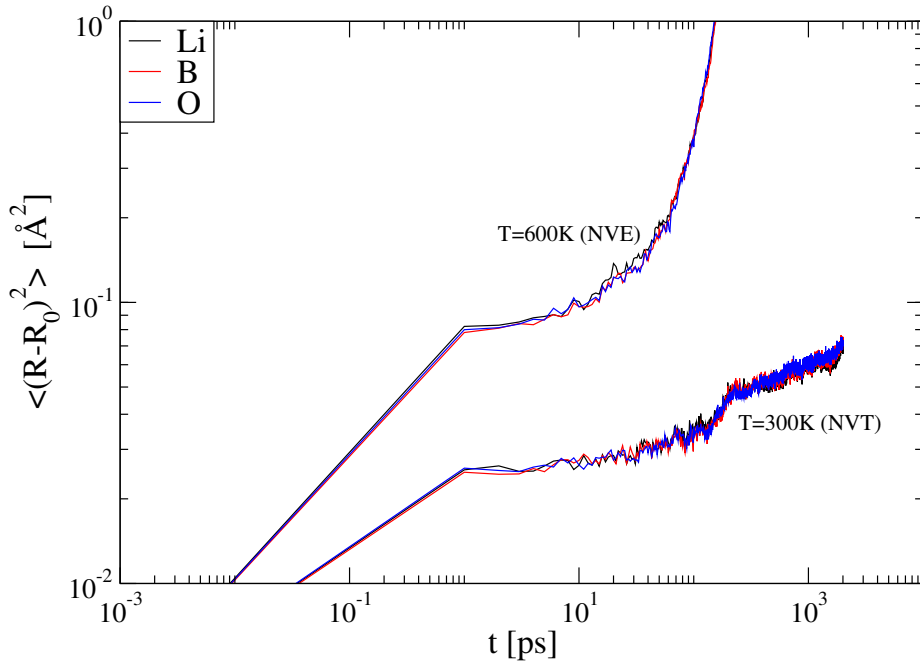


Figure 1:  $\text{Li}_2\text{O}-\text{B}_2\text{O}_3$  mean square displacement for two temperatures.

we therefore aim at testing the BV method against MD-simulations. It will be shown that one should take care whenever using BV methods which do not seem to work well when applied to amorphous systems.

Additionally, most of the available effective force fields were developed more than a decade ago and were mostly tested by checking the stability of crystalline structures during short MD runs of a few pico seconds. The reliability of these potential models is not clear.

For example, MD-simulations of borate systems were performed with a pairwise interaction potential, and the distribution of  $\text{BO}_4$  tetrahedra and trigonal  $\text{BO}_3$  structures was determined, as well as the percentage of non-bridging oxygens (oxygen atoms which only have a bond to one boron atom). While the structural data obtained from these simulations look reasonable, already simple dynamic properties cannot be accounted for. Figure 1 shows the mean square displacement of a  $\text{Li}_2\text{O}-\text{B}_2\text{O}_3$  system where the same interaction model is used as in [15]. One of the most basic properties of ion-conducting alkali glasses, namely the decoupling of the motion of the alkali ions from the slow rearrangements of the glassy network, is not reproduced. In fact, analysing the number density of the system reveals that the network is rapidly rearranging on the same time scale, on which the ionic motion takes place, and the system is liquid like.

Moreover, while the range of glass compositions of technical relevance is very broad, the number of glass systems for which potential models exist

---

is small. This makes it clear that it is of great interest to develop procedures for obtaining and evaluating new effective force fields. As discussed earlier, the available experimental data concerning microscopic structures is rather limited for glasses. Therefore one promising approach is to determine potential parameters from ab initio quantum mechanical calculations. A necessary requirement to do this is the ability to produce reasonably good representations of glass systems with ab initio calculations. We will show that it is possible to produce fairly large clusters with Hartree Fock (HF) and density functional theory (DFT) methods which reproduce vibrational spectra of measured glass systems. Thus they can be used for the determination of classical force fields for MD and MC simulations. The performed ab initio calculations also allow a first valuable insight into structural properties. Using these techniques it was possible to determine the role of nitrogen in the already mentioned glass forming process for thin film LISON glasses.

These calculations can also be seen as first steps in order to develop methods which allow a consistent multi scale approach for the modelling of glasses. Ab initio methods allow a detailed characterisation of the short range interactions of the atoms and structural units, and provide effective potential models for MD and MC simulations. Based on MD and MC simulations, quantitative, material specific transport models can be developed. These may allow for an improved design of new glass types and technical devices.

Most of the investigations were performed as part of the HI-CONDELEC EU project. Its goal is the development of thin films of a high conductive solid ionic conductor for lithium. Inspired by the promising results of K. H. Joo [1, 2] mixed alkali glass systems are investigated where lithium sulfate and lithium borate are the main components.

## 2 Molecular dynamics simulations and bond valence sum calculations

In order to model atomic and molecular systems, one successful and widely used method are molecular dynamics (MD) simulations. Based on a potential model, Newton's equations are used to classically simulate the time evolution of a system. Depending on the properties one wants to investigate, the interactions are modeled by potentials as simple as a Lennard Jones pair potential up to full quantum mechanical calculations. From the trajectories of all atoms, microscopic and macroscopic equilibrium properties of the system are calculated and the dynamics of the system are investigated directly. In ion-conducting glasses, one important application is to determine diffusion paths and sites of the mobile ion species in the disordered network. By this one can gain insight into the conduction mechanism. With the same goal another approach based on bond valence sum calculations has been followed. It allows the identification of favourable regions in space where the mobile ions reside from a known network structure. Such network structures can be determined from diffraction data by reverse Monte-Carlo (RMC) calculations.

While a model of a glass in MD-simulations does not necessarily fully represent the real system, it is a valid physical glass system in itself. Therefore it is possible to use the network structure generated by MD-simulations as input for the Bond Valence method. As we know the correct diffusion paths of the mobile ions in this model system, it allows us to directly test the quality of the diffusion paths determined from bond valence calculations. We will show that the diffusion paths determined by BV calculations do not compare very well with the MD diffusion paths, and that most of the coincidence is due to geometric constraints as given by a hard sphere model.

### 2.1 Molecular dynamics simulations

As the full set of Newton's equations is generally a nonlinear highly coupled one (in cases of non-bonded interactions as Coulomb potentials every atom potentially interacts with every other), it is not possible to find analytical expressions for the phase space trajectories of a system (that is location  $\mathbf{q}(t)$  and momentum  $\mathbf{p}(t)$  of every particle at any given time). In the framework of MD-simulations the problem is discretised in time, and the whole dynamics are approximated on this time grid and calculated numerical. The first MD-simulations were performed in the late 50ties and the 60ties, where small liquid systems with 100 to 200 atoms were investigated for their structural properties on time scales of picoseconds. Nowadays, typically MD-simulations are performed with several thousand atoms on time scales of some nanoseconds. The largest simulations already contain some billion particles, while for smaller systems time intervals of a millisecond

have been simulated.

Taylor expansion with respect to time yields the following formal equations:

$$\mathbf{q}(t + \Delta t) = \sum_{i=0}^{\infty} \frac{1}{i!} \left. \frac{d^i \mathbf{q}(\tau)}{d\tau^i} \right|_{\tau=t} (\Delta t)^i . \quad (2)$$

Truncating the expansion after the third term gives the most straightforward approach to calculate the position and velocity of a particle at time  $t + \Delta t$  from the acceleration  $\mathbf{a}(t)$ , velocity  $\mathbf{v}(t)$  and coordinates  $\mathbf{q}(t)$  at time  $t$ , the Euler integration scheme:

$$\mathbf{q}(t + \Delta t) = \mathbf{q}(t) + \mathbf{v}(t)\Delta t + \frac{1}{2}\mathbf{a}(t)\Delta t^2 + O(\Delta t^3) \quad (3)$$

$$\mathbf{v}(t + \Delta t) = \mathbf{v}(t) + \mathbf{a}(t)\Delta t + O(\Delta t^2) \quad (4)$$

where the acceleration is obtained from the forces as  $\mathbf{a}(t) = \frac{1}{m}\mathbf{F}(\mathbf{q}(t))$ . The basic Euler integration scheme is not time reversible. While one could calculate a set of coordinates  $\mathbf{q}(t)^*$  from the coordinates  $\mathbf{q}(t + \Delta t)$ , velocities  $\mathbf{v}(t + \Delta t)$ , and accelerations  $\mathbf{a}(t + \Delta t)$  by using a negativ timestep, these differ by  $1/2(\mathbf{a}(t + \Delta t) - \mathbf{a}(t))\Delta t^2$  from the original set of coordinates  $\mathbf{q}(t)$ .

A time reversible algorithm, which is also one order more accurate in  $\Delta t$ , is the so-called Verlet algorithm [16] which results from truncating the expansion after the fourth term and summing up  $\mathbf{q}(t + \Delta t)$  and  $\mathbf{q}(t - \Delta t)$ . As the Taylor coefficients are the same for both expansions the uneven terms in  $\Delta t$  vanish, which leads to

$$\mathbf{q}(t + \Delta t) = 2\mathbf{q}(t) - \mathbf{q}(t - \Delta t) + \frac{1}{2}\mathbf{a}(t)\Delta t^2 + O(\Delta t^4) . \quad (5)$$

The velocities of the particles can then be calculated as

$$\mathbf{v}(t) = \frac{\mathbf{q}(t + \Delta t) - \mathbf{q}(t - \Delta t)}{2\Delta t} + O(\Delta t^2) . \quad (6)$$

This method has drawbacks and is rarely used in practise. The velocities lag behind by one step and they are only correct in the first order of  $\Delta t$ . The latter problem is not as bad as it seems though, because the errors do not accumulate as the velocities are calculated each time step from the coordinates. More serious problems are numerical ones. Subtracting two values, which are almost equal, reduces the numerical precision considerable.<sup>1</sup> While this numerical problem only affects the velocities again, another one affects the positions. In eq. (5) a term of second order in  $\Delta t$  is added to one of zeroth order, which limits the accuracy of the iteration scheme due to precision limitations of the numerics.<sup>2</sup>

<sup>1</sup>As an example, if one subtracts two numbers from each other, which are exact in the 10 first digits but similar up to the 7th digit, the result is only reliable in the first 2 digits.

<sup>2</sup>Consider numbers with 10 digits precision and let  $\Delta t = 10^5$  in appropriate dimensionless units. Then  $\Delta t^2$  would equal already  $10^{-10}$  and thus reaching the precision limit of the computer numerics.

## 2 MOLECULAR DYNAMICS SIMULATIONS AND BOND VALENCE SUM CALCULATIONS

---

Two algorithms derived from the Verlet algorithm, which circumvent these problems, are the so-called Leap-frog algorithm and the velocity Verlet algorithm [17]. The expansion of  $\mathbf{q}(t)$  around  $t + \frac{1}{2}\Delta t$  yields:

$$\mathbf{q}(t + \Delta t) = \mathbf{q}\left(t + \frac{\Delta t}{2}\right) + \mathbf{v}\left(t + \frac{\Delta t}{2}\right) \frac{\Delta t}{2} + \frac{\mathbf{a}\left(t + \frac{\Delta t}{2}\right)}{2} \left(\frac{\Delta t}{2}\right)^2 + O(\Delta t^3) . \quad (7)$$

Using the same expansion with  $-\frac{\Delta t}{2}$  and subtracting  $\mathbf{q}(t)$  from eq. (7) gives the following expression for the positions:

$$\mathbf{q}(t + \Delta t) = \mathbf{q}(t) + \mathbf{v}\left(t + \frac{\Delta t}{2}\right) \Delta t + O(\Delta t^3) . \quad (8)$$

An analogous expression for the velocities is

$$\mathbf{v}\left(t + \frac{\Delta t}{2}\right) = \mathbf{v}\left(t - \frac{\Delta t}{2}\right) + \mathbf{a}(t) \Delta t + O(\Delta t^3) . \quad (9)$$

By splitting up this last equation into two steps one can calculate a value for  $\mathbf{v}(t)$ :

$$\mathbf{v}(t) = \mathbf{v}\left(t - \frac{\Delta t}{2}\right) + \mathbf{a}(t) \frac{\Delta t}{2} + O(\Delta t^3) \quad (10a)$$

$$\mathbf{v}\left(t + \frac{\Delta t}{2}\right) = \mathbf{v}(t) + \mathbf{a}(t) \frac{\Delta t}{2} + O(\Delta t^3) . \quad (10b)$$

Using (10) and (8) yields the velocity Verlet algorithm which is one of the commonly used integrators in practise due to several convenient properties:

- (i) It is self-starting.
- (ii) It is time reversible.
- (iii) It is symplectic (i.e. it does not violate Liouville's theorem).
- (iv) The errors for each time step are of  $O(\Delta t^3)$  for both positions and velocities.
- (v) Only terms are combined, which differ by one order in  $\Delta t$ .
- (vi) The positions, velocities, and accelerations only have to be kept for one step at the same time, reducing the necessary memory.
- (vii) It conserves the angular momentum exactly in case of spherical force fields.

In summary, the integration scheme starting from a given set of  $\mathbf{q}(t)$ ,  $\mathbf{v}(t)$ , and  $\mathbf{a}(t)$  for the velocity Verlet algorithm is:

$$\begin{aligned} \mathbf{v}\left(t + \frac{\Delta t}{2}\right) &= \mathbf{v}(t) + \mathbf{a}(t) \frac{\Delta t}{2} \\ \mathbf{q}(t + \Delta t) &= \mathbf{q}(t) + \mathbf{v}\left(t + \frac{\Delta t}{2}\right) \Delta t \\ \mathbf{a}(t + \Delta t) &= \frac{1}{m} \mathbf{F}(\mathbf{q}(t + \Delta t)) \\ \mathbf{v}(t + \Delta t) &= \mathbf{v}\left(t + \frac{\Delta t}{2}\right) + \mathbf{a}(t + \Delta t) \frac{\Delta t}{2} \end{aligned}$$

It is worth noting that the global error of a method is one order higher than that of a single time step. Let  $t$  be the simulation time and  $\Delta t$  the time step interval, then is  $t = N\Delta t$  with  $N$  being the number of time steps. As the errors accumulate the global error of  $N$  time steps for the velocity Verlet algorithm is:  $N O(\Delta t^3) = O\left(\frac{t}{\Delta t} \Delta t^3\right) = O(\Delta t^2)$ .

Other integration algorithms that are more accurate exist, but they require several force computations per time step. One class of such integrators are Runge Kutta methods. They are so-called multi-step methods, i.e. the slope of a function is calculated at several points within one interval  $\Delta t$ . For an ordinary first order differential equation  $y' = f(t, y)$  the integration scheme for RK4 (fourth order Runge Kutta method) which yields a global error of  $O(\Delta t^4)$  is:

$$y(t + \Delta t) = y(t) + \frac{\Delta t}{6}(k_1 + 2k_2 + 2k_3 + k_4) \quad (11)$$

where

$$\begin{aligned} k_1 &= f(t, y(t)) \\ k_2 &= f\left(t + \frac{\Delta t}{2}, y(t) + \frac{\Delta t}{2}k_1\right) \\ k_3 &= f\left(t + \frac{\Delta t}{2}, y(t) + \frac{\Delta t}{2}k_2\right) \\ k_4 &= f(t + \Delta t, y(t) + \Delta tk_3) . \end{aligned} \quad (12)$$

While a single time step computed with the Runge Kutta method consumes roughly four times as much computational time as a time step with the velocity Verlet algorithm (the forces have to be computed for four different positions), the higher accuracy of this algorithm allows the usage of a much larger time step interval without increasing the global error over that of the velocity Verlet algorithm. The true reason why it is not often used is therefore not necessarily the increased computational demand per time step, but another property: As most common multi-step methods, Runge

## 2 MOLECULAR DYNAMICS SIMULATIONS AND BOND VALENCE SUM CALCULATIONS

---

Kutta methods are neither symplectic nor time reversible. This holds also true for predictor corrector algorithms and other higher order integrators, and is the reason why the velocity Verlet algorithm is still the most common integrator for molecular dynamics simulations.

The equations presented above are sufficient to simulate atomic systems at constant total energy. In the case of using the velocity Verlet algorithm this corresponds to the micro-canonical ensemble. If one wants to couple the system to a heat bath with constant temperature  $T_0$ , it is necessary to introduce some kind of thermostat into the integration process.

The most straightforward approach is to simply scale the velocities at every time step. As known from basic thermodynamics the temperature of a system is given by

$$E_{\text{kin}} = \frac{3}{2} N k_B T \quad (13)$$

where  $E_{\text{kin}} = \langle \sum_i^N \frac{1}{2} m_i \mathbf{v}_i^2 \rangle$  is the kinetic energy of the system,  $N$  the number of particles, and  $T$  the temperature. This allows the computation of an 'instantaneous temperature' as:

$$T(t) = \frac{1}{3Nk_B} \sum_i^N m_i \mathbf{v}_i(t)^2 . \quad (14)$$

By scaling the velocities every time step with a factor of  $\sqrt{\frac{T_0}{T(t)}}$ , the temperature can be kept constant. In the velocity Verlet algorithm this scaling factor would be introduced in equation (10a).

Such a brute force temperature scaling perturbs the dynamics of the system and is rarely used today. A better solution is the Nose-Hoover (NH) thermostat which dates back to two works of Nosé [18] and Hoover [19]. Nosé introduced an additional degree of freedom in the system, a variable  $\xi(t)$ . The new equations of motion are

$$m_i \dot{\mathbf{v}}_i = \mathbf{F} - \nu \xi m_i \mathbf{v}_i \quad (15)$$

$$\dot{\xi} = \nu \left( 1 - \frac{T(t)}{T_0} \right) . \quad (16)$$

Thus the NH thermostat acts as friction where the friction coefficient depends on the difference of the temperature of the system to the temperature of the heat bath. The additional parameter  $\nu$  gives a time scale on which the temperature relaxes. Note that not  $\xi(t)$  itself is given by the instantaneous temperature, but its time derivative.

Nosé showed that when using these equations of motion, the system approaches the canonical ensemble (i.e. the ensemble average of an observable  $A(\mathbf{v}, \mathbf{q})$  of a system following eqs. (15) and (16) over an infinite time interval is the same as for the canonical ensemble).

It is straightforward to implement the NH thermostat in the velocity Verlet algorithm by propagating  $\xi$  similar to  $\mathbf{v}$  with two half steps. The altered integrator is still time reversible and symplectic.

### 2.1.1 Simulating glasses

Glasses have been studied by MD-simulations for more than 30 years. A pioneering work was that of Woodcock, Angell, and Cheeseman in 1976: *Molecular dynamics studies of the vitreous state: Simple ionic systems and silica* [20]. They discussed various basic concepts regarding the simulation of glasses. In particular they simulated a  $\text{SiO}_2$  system, where they guessed the parameters for the used Born-Mayer-Huggins potential (which is in essence equal to the Gilbert Ida type potential used in our simulation, see eq. (17)). These parameters were optimised based on the comparison of calculated pair distribution functions from a first simulation with experimental ones from x-ray diffraction measurements. They showed that it is possible to get the effect of permanent densification of a  $\text{SiO}_2$  glass in the MD-simulation.<sup>3</sup> Additionally, Woodcock *et al.* showed that there exist many different configurational energy minima which is presumably necessary to see a glass forming process. Later the parameters for the simulation of glasses were often derived by determining force constants from experiments of corresponding crystalline systems with the same composition.

A mayor step was the determination of potential parameters from ab initio Hartree Fock calculations in 1988. Tsuneyuki *et al.* obtained parameters for a  $\text{SiO}_2$  crystal from ab initio calculations of a single  $\text{SiO}_4$  tetrahedron [21]. By fitting the parameters to the energy of the cluster for different Si-O distances they obtained a potential, which allowed them to reproduce different silica phases ( $\alpha$ -quartz,  $\alpha$ -cristobalite, coesite, and stishovite), and their respective elastic properties. As there are a lot of possible sets for the potential parameters, which fit well the calculated energies of the cluster for the 16 different Si-O distances, they performed MD calculations for several of them and chose the one which best reproduced  $\alpha$ -quartz. One should note that the partial charges were scanned for optimal parameters and not obtained from the Hartree Fock calculations.

The most commonly used potential for silicate systems was developed in a similar way. In 1990 B. van Beest, G. Kramer, and R. van Santen reported a set of potential parameters [22] for the same type of potential as Tsuneyuki *et al.*. They carried out Hartree Fock calculations on a single  $\text{SO}_4$  unit, but included more experimental data from  $\alpha$ -quartz as well as an additional bending mode into the fitting procedure. This so-called BKS potential was shown to reproduce all silica crystal phases, and is currently the best studied potential model for network glasses.

---

<sup>3</sup>After compressing a silicate glass by applying high pressures, the relaxed material has a higher density than it had before the compression.

Other groups used the Tsuneyuki or the BKS model as basis for potential parameter sets including alkali ions. One of these sets was determined by J. Habasaki and I. Okada in 1992 and will be applied in this work [23].

Similar approaches have been followed for other network glasses. Potential parameters (again for a Born-Mayer-Huggins type potential with additional Coulomb interaction) for borates, for example, have been proposed by Soules and Varshneya [24]. They assumed that the atoms are fully ionised and used empirically determined ion radii. Later Verhoef and den Hartog modified these parameter sets in order to obtain correct vibrational properties of the vitreous  $B_2O_3$  system [25]. They extended the model to include lithium atoms in the simulation. As all parameters in the original potential are already decomposed into atomic parameters, namely the partial charges and the ionic radii, they made the assumption that the lithium ions carry one elementary charge, and took the ion radii value for lithium published by Tosi and Fumi. Additionally, they introduced a three body harmonic interaction, in order to narrow the distribution of B-O-B angles.

The potentials are obviously only approximations of the real interatomic interactions. The question how accurate they actually represent reality is of crucial importance. For example it is questionable whether pure spherical pair interactions are sufficient to describe glass networks accurately. In fact, it is generally accepted that partial covalency exists in Si-O bonds. Such covalent character of a bond is usually connected with a directional order which may not be caught by purely spherical force fields. Additionally, it is worth thinking about whether deriving potential parameters from experimental crystalline data is the best way to get optimal force fields for the simulation of glasses. Finally, even if the potentials would be perfect, there would still be some clear differences in the simulated glasses compared to real ones. The cooling rates in the computer experiment are much higher than in reality. These cooling rates can have an important influence on the physical properties of the resulting glass. For example, the glass temperature  $T_G$  depends on the cooling rate, as it is the temperature where the relaxation time of the system becomes long with respect to the cooling rate. As a consequence, the glass temperature of MD glasses is much higher than the one observed in the laboratory. It is also observed that glasses produced from liquids by cooling are less compact when cooled faster. In summary it is possible that deviations of the properties of simulated glasses from experimental data are not due to poor potential models, but are just a result of the unphysical high quenching rates used in computer experiments.

In the beginning most of these potentials were only used to investigate structural properties. One of the main reasons for this was the lack of computational power which is necessary to simulate time scales relevant for dynamic properties. About 10 years ago this changed, and first investigations dealing with conduction mechanisms were reported.

### 2.1.2 LAMMPS

We performed molecular dynamics simulations by using a modified version of the LAMMPS program suite [26, 27]. This program is published by Sandia National Laboratories in USA under the GNU General Public License.

LAMMPS is an acronym for Large-scale Atomic/Molecular Massively Parallel Simulator. It is an extensive program package (100.000 lines of C++ code) with a good performance for parallel processing. It already has a wide range of potential types implemented and can be used via a comfortable scripting system. LAMMPS has several advantages,

1. It is free.

Published under the GNU GPL there is no need to buy licenses. Additionally the source code is available (in fact one can only download the source code) which allows one to make necessary changes for specific purposes.

2. It is maintained well.

LAMMPS is maintained by a group of the Sandia National Laboratories, USA. Frequent new releases increase the functionality of the program.

3. It is easy to modify.

Due to its object orientated design LAMMPS is rather easy to extend. The source code is structured well and can be understood despite its enormous scope. With moderate C++ knowledge it is possible to add new functionality to the program, and to make these functions accessible via the script system. For our purposes this was necessary to introduce the possibility of tracking the particle number densities as well as analysing the hopping motion.

LAMMPS uses the velocity Verlet algorithm as the standard integrator for atomic systems. An NH thermostat is implemented for temperature control. The parallelisation scheme is based on spatial decomposition, i.e. the simulation box is divided into  $n$  subdomains where every processor handles the short range interactions of the atoms in one subdomain. The long range Coulomb interactions are treated by a particle-particle-particle-mesh (pppm) algorithm using fast Fourier transformation. This algorithm is up to 100 times faster for the systems we simulated than the alternatively implemented Ewald summation.<sup>4</sup>

---

<sup>4</sup>That is only valid when using one node of the computer cluster, as the ppm algorithm is much more dependent on fast inter-processor communication than the Ewald algorithm.

## 2 MOLECULAR DYNAMICS SIMULATIONS AND BOND VALENCE SUM CALCULATIONS

---

Table 1: Potential parameters for the MD-simulations (cf. eq. (17)).

Ion	$z$	$a$ [Å]	$b$ [Å]	$c$ [Å <sup>3</sup> √kJ/mol]
Li <sup>+</sup>	0.87	1.0155	0.07321	22.24
Si <sup>4+</sup>	2.40	0.8688	0.03285	47.43
O <sup>2-</sup>	-1.38	2.0474	0.17566	143.98
		$f_0 = 4.186 \text{ kJÅ}^{-1} \text{ mol}^{-1}$		$r_c = 1.3 \text{ Å}$

### 2.1.3 Setup of molecular dynamics simulations

We perform MD-simulations of a lithium silicate glass with the chemical formula Li<sub>2</sub>SiO<sub>3</sub> using the potential model of J. Habasaki and I. Okada [23]. The cubic simulation box has a length  $L = 50.04 \text{ Å}$  and contains 11664 atoms (3888 Li, 1944 Si, 5832 O) corresponding to a density of  $2.27 \frac{g}{cm^3}$ . Periodic boundary conditions are used. The simulations are performed in the NVE ensemble (micro canonical ensemble where the number  $N$  of particles, the volume  $V$  of the simulation box, and the total energy  $E$  are kept constant). The energy  $E$  was adjusted so that the temperature of the system fluctuates around a mean value of 615 K with deviations of 10 K. The systems are equilibrated for about 1 ns and the runs for obtaining data have a duration of 2 ns, using a time step interval of  $\Delta t = 1 \text{ fs}$ .

The effective interatomic interactions between two atoms of type  $i$  and  $j$  at distance  $r$  are:

$$U_{ij}(r) = \frac{e^2}{4\pi\epsilon_0} \frac{z_i z_j}{r} + f_0(b_i + b_j) \exp\left(\frac{a_i + a_j - r}{b_i + b_j}\right) - \frac{c_i c_j}{r^6} \quad (17)$$

where the parameters listed in table 1 have been optimised [23] and shown to give good agreement with experimental data [23, 28, 29, 30]. The interaction potential in eq.(17) is composed of three terms. The first one in (17) is the Coulomb interaction with effective charge numbers for the species. The second term is a Born-Meyer type potential, which takes the short-range repulsive interactions into account, and the third is a dispersive van-der-Waals interaction. It is only used for interactions involving oxygen [31].

The system was prepared by putting the atoms on a cubic crystal lattice and assigning to every atom random velocities drawn from a Maxwell-Boltzmann distribution corresponding to a temperature of 2500 K. This temperature is well above the glass temperature of the system. From this liquid state the system is cooled down in several steps with intermediate periods of equilibration, in between as shown in figure 2. First an NVT run (canonical ensemble, where the number  $N$  of particles, the volume  $V$  and the temperature  $T$  are fixed) of 10 ps at 2500 K is performed, followed by an NVE run of the same duration. After simulating another 20 ps in the NVT

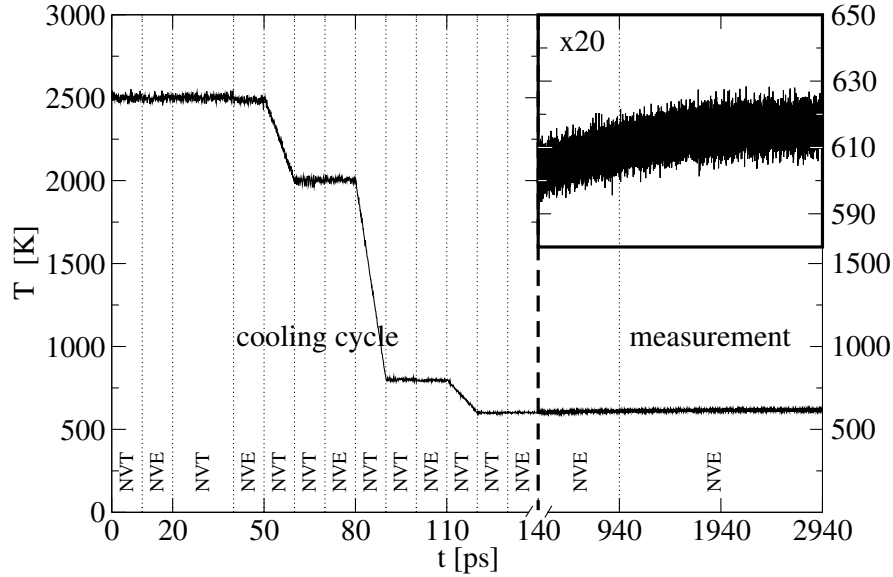


Figure 2: Temperature of the system for the cooling process and the measurement run. Note the change of scale on the time axis at 140 ps. The inset shows a magnification of the temperature development from 140 ps to 2.94 ns.

ensemble and 10 ps under NVE conditions the temperature is decreased in three subsequent sequences down to 600 K. Each cooling cycle consists of a 10 ps run using a thermostat to decrease the temperature linearly, a 10 ps NVT run at the target temperature, and a 10 ps NVE run to verify that there are no temperature drifts. The configurations at the end of the 600 K cooling cycle are used as starting points for a 800 ps long equilibration run using the NVE ensemble. The measuring runs are 2 ns long.

The mean square displacement of the lithium, oxygen, and silicon ions shown in figure 3(b) demonstrate a clear decoupling of the motion of the lithium ions and the glass network. While the lithium ions are still mobile in the case of the 600 K simulation, the network is practically frozen. The lithium ions show normal diffusive behaviour on time scales larger than 100 ps. The relaxation of the network due the ageing processes is negligibly small within the simulated time interval. That some ageing actually takes place can be seen from the magnified temperature plot in the inset of figure 2. The slow increase of temperature from a mean value of 603 K before equilibration run starts ( $t = 140$  ps) to 616 K at the end of the measurement run ( $t = 2.940$  ns), corresponds to a relaxation of the network, where potential energy is transformed into kinetic energy. The average temperature during the measurement run was 615 K with a standard deviation of 3.8 K.

## 2 MOLECULAR DYNAMICS SIMULATIONS AND BOND VALENCE SUM CALCULATIONS

---

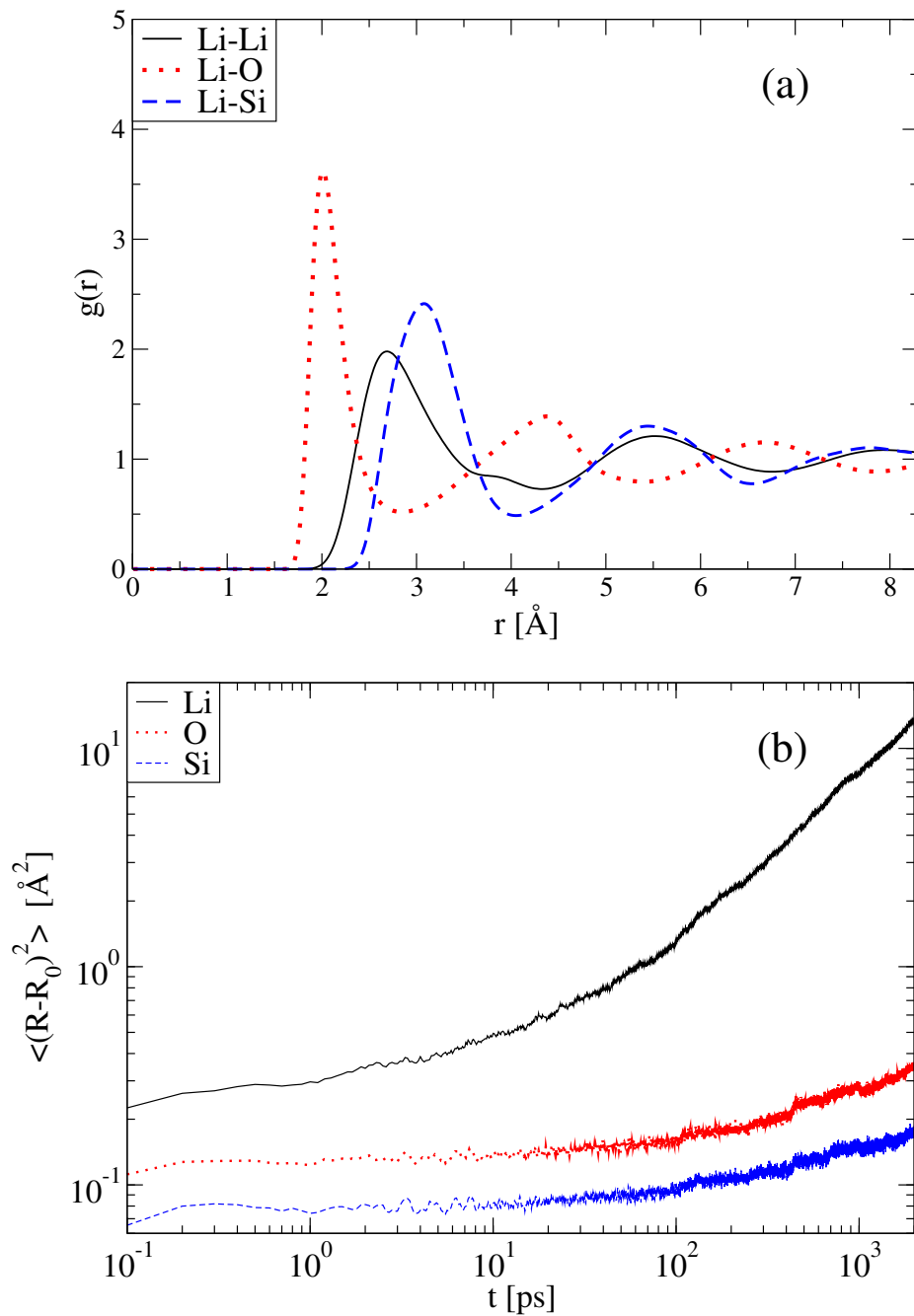


Figure 3: (a) Pair correlation function of Li-Li, Li-Si and Li-O and (b) time-dependent mean square displacements of Li, O and Si ions at  $T = 600$  K.

## 2.2 Determination of diffusion pathways and ion sites

The dynamics of mobile ions in glasses can be described by a hopping motion [4, 7, 8]. One speaks of a hopping motion if there exist localised regions called ion sites, where the mobile ions reside most of the time, while transitions between two neighbouring sites take negligible small times. This corresponds to an ion number density  $\rho(\mathbf{x})$  which exhibits pronounced local maxima.

First we will describe a way of how to identify diffusion paths and ion sites based on an analysis of  $\rho(\mathbf{x})$  obtained from MD-simulations respectively by using the BV method, before comparing these MD and BV paths in the next subsection. Using a density threshold  $\rho_{\text{th}}$  we define a path  $\mathcal{P}(\rho_{\text{th}}) = \{\mathbf{x} | \rho(\mathbf{x}) > \rho_{\text{th}}\}$  as the region in space where  $\rho(\mathbf{x}) > \rho_{\text{th}}$ . A subsequent cluster analysis depending on  $\rho_{\text{th}}$  allows the identification of the favourable sites of the ions. As the molecular dynamics simulations provide the whole particle trajectories  $\rho(\mathbf{x})$  can be determined by subdividing the simulation box into a grid of cubic cells with a length  $\Delta$  and registering the time  $t_i$  (the number of simulation steps multiplied by the time step interval  $\Delta t = 1$  fs) for each cell  $i$ , where it is occupied by a lithium ion. Dividing this occupation time by the total simulation time  $t_{\text{sim}}$  and the cell volume gives its average number density  $\rho(\mathbf{x}_i) \simeq \rho_i = (t_i/t_{\text{sim}})\Delta^{-3}$ .

In order to identify sites we perform a connectivity analysis of the cells in dependence of  $\rho_i$ . Using the Hoshen-Kopelman algorithm [32] we determine clusters of connected (face sharing) cells  $i$  with  $\rho_i > \rho_{\text{th}}$ . As long as the grid spacing is fine enough, one can expect that the same clusters are identified independent of  $\Delta$ . Figure 4 shows the number of clusters  $N_{\text{cl}}(\rho_{\text{th}})$  in dependence of  $\rho_{\text{th}}$  for five grid spacings  $\Delta$ . The three curves belonging to values  $\Delta < 1$  Å show the same behaviour: Starting from large  $\rho_{\text{th}}$  an increasing number of clusters is found with decreasing  $\rho_{\text{th}}$  because more and more local maxima in  $\rho(\mathbf{x})$  are identified. At some point the maximal number of clusters is reached. Decreasing  $\rho_{\text{th}}$  further eventually leads to a sudden decrease in the number of clusters. This can be understood as follows: For large  $\rho_{\text{th}}$ , the only cells found are the ones belonging to regions in space where the ions stay relatively long. These form the core of sites in a hopping model. As jumps between these sites only take a comparably small amount of time, the cells belonging to the connecting pathways only have a small occupation probability. One could expect that there exists a 'typical' ion number density on such pathways. As soon as the threshold value  $\rho_{\text{th}}$  falls below that typical value, a lot of clusters coalesce and the number of clusters drops rapidly.

For  $\Delta > 1$  Å the maximal number of clusters is much lower than the number of lithium ions in the system. This indicates that the grid is not fine enough, and the maxima of  $\rho(\mathbf{x})$  cannot be resolved properly.

Indeed, looking at figure 5, which shows the lithium number density of a 1.564 Å thick slice of the system with different grid spacings  $\Delta$ , one can

## 2 MOLECULAR DYNAMICS SIMULATIONS AND BOND VALENCE SUM CALCULATIONS

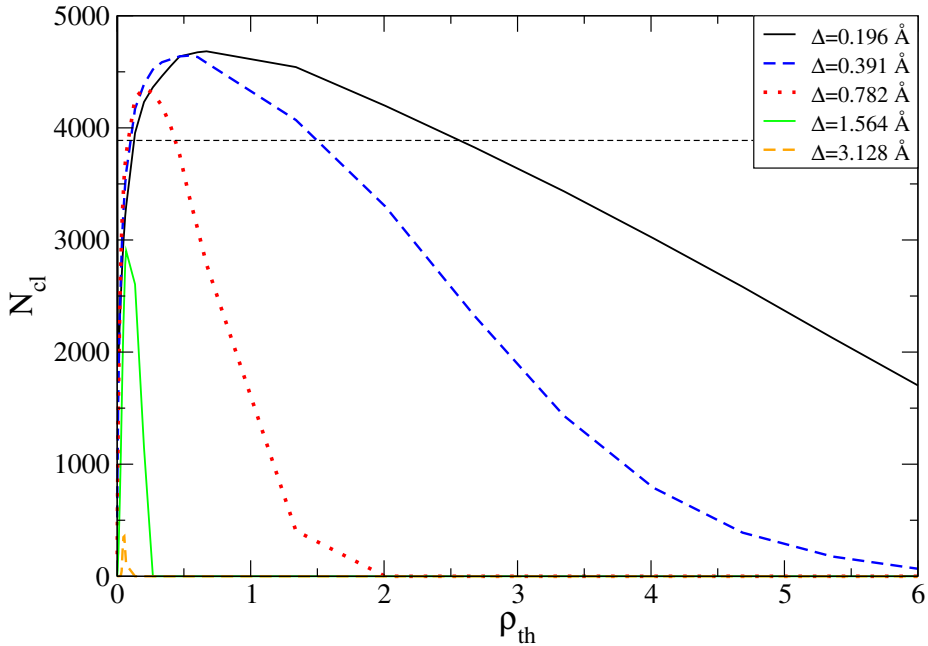


Figure 4: Number of clusters  $N_{cl}$  in dependence of  $\rho_{th}$  for three different five spacings  $\Delta$ . Note that the mean number density of Li ions is only  $3888/(50.04 \text{ \AA})^3 \cong 0.031 \text{ \AA}^{-3}$  which - in comparison with the relevant scale of  $\rho_{th}$  - implies that the Li ions are strongly localised on the clusters. The dashed line marks the number of Li ions in the system.

easily see this grid size effect. In figure parts 5(c)-(e) sites could be assigned quite easily. This is not the case for figure parts 5(a) and 5(b) where most of the details of  $\rho(\mathbf{x})$  are lost. As an approximation for a critical  $\Delta$  a value of half of the typical lithium site distance seems to be reasonable.

From the discussion above it is clear that there exists an interval  $\rho_{path} < \rho_{th} < \rho_{sites}$ , where all maxima in  $\rho(\mathbf{x})$  are found and where they do not merge as long as the grid spacing is small enough. This is indeed the case as can be seen from figure 4. The two curves with  $\Delta < 0.5 \text{ \AA}$  go through a plateau with the same number of clusters which corresponds to the number of possible sites in the system. Above  $\rho_{sites}$  some maxima are not resolved, below  $\rho_{path}$  different maxima start to merge. Within this interval one can use any value for  $\rho_{th}$  to define the clusters which are candidates for sites. In order to identify as much volume of the site candidates as possible we use  $\rho_{path}$  (strictly speaking one should use  $\rho_{path}$  in the limit  $\Delta \rightarrow 0$ , as  $\rho_{path}$  weakly depends on  $\Delta$ ). The strong dependence on the grid spacing at large  $\rho_{th}$  shows that the maxima in  $\rho(\mathbf{x})$  are sharp. For large  $\Delta$  the average density  $\rho_i$  of a cell containing a maxima can fall below  $\rho_{th}$  and therefore the local maxima is not resolved. Our choice of  $\rho_{th} = 0.54$  yields a total

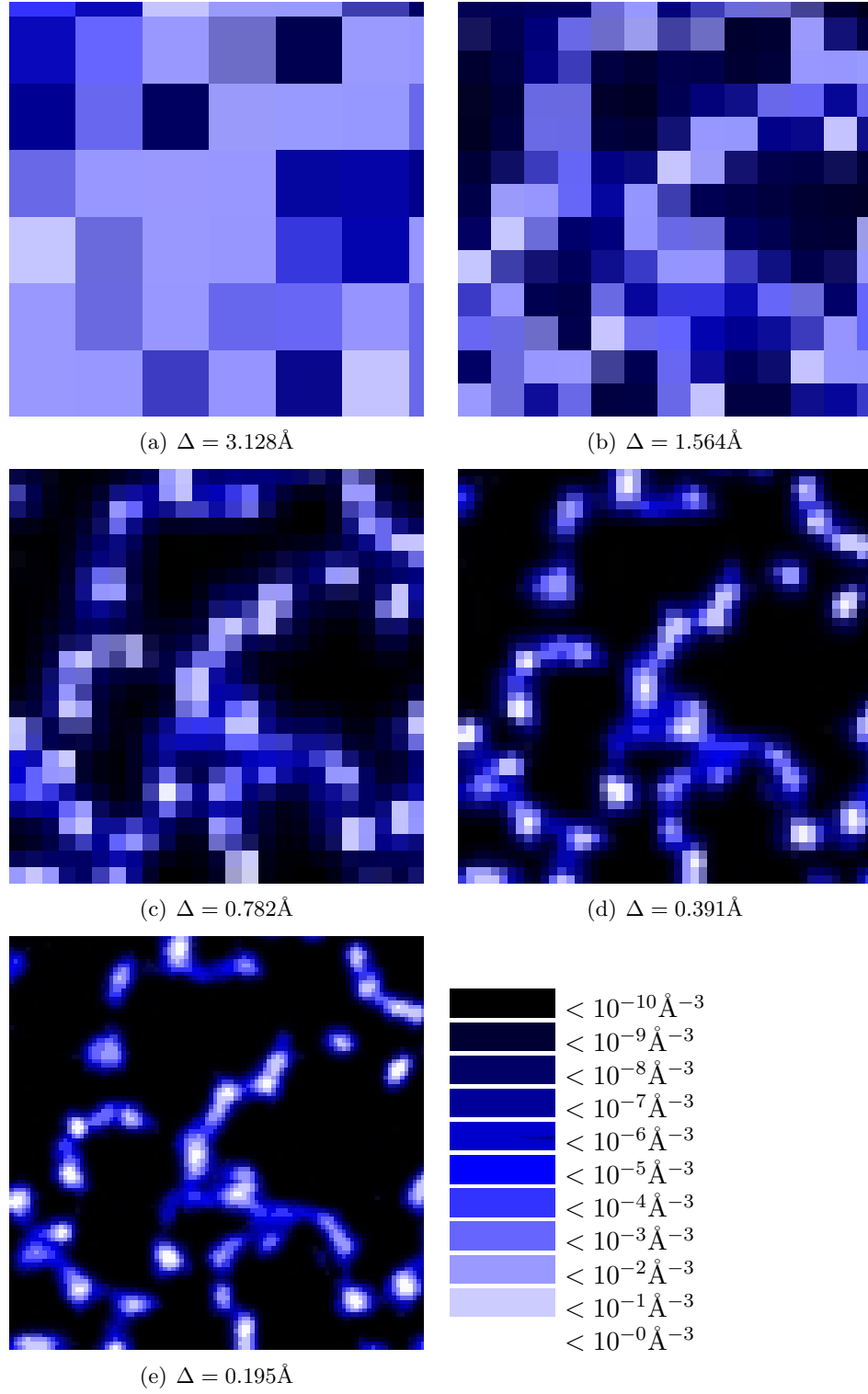


Figure 5: Number density of Li ions in a  $1.564\text{\AA}$  thick slice of the system for various grid spacings  $\Delta$  decreasing from (a) to (e).

## 2 MOLECULAR DYNAMICS SIMULATIONS AND BOND VALENCE SUM CALCULATIONS

---

number of 4608 clusters which is 1.185 times the number of lithium ions in the system.

The question arises whether all of the identified clusters are sites in view of a hopping motion. We only want to consider such clusters as sites where the residence time of lithium ions on them is large compared to the time these ions need to jump to adjacent clusters. Therefore we have to characterise the clusters further. First we determine the mean number density of Li ions of a cluster as  $\rho_{cl} = \sum_{i \in cl} \rho_i / n_{cells}$  where we sum over all cells, which belong to a given cluster according to the cluster analysis, and  $n_{cells}$  denotes its number of cells. Then the clusters are numbered in order of increasing  $\rho_{cl}$  and their volume  $V_{cl} = n_{cells} \Delta^3$  and their occupation probability  $t_{cl}/t_{sim} = \sum_{i \in cl} t_i / t_{sim} = \rho_{cl} V_{cl}$  is calculated. The results for  $\rho_{cl}$ ,  $V_{cl}$ , and  $t_{cl}/t_{sim}$  are shown in figure 6.

Most of the clusters with a number below 500 have an occupation probability of less than 0.1. Clusters with numbers larger than 500 show a wider distribution of cluster volumes and occupation probabilities. Their volume lies between  $0.25 \text{ \AA}^3$  and  $0.6 \text{ \AA}^3$ , and occupations probabilities lie between 0.5 and 0.9 for most of the clusters. Summing up the occupation probabilities of all clusters, one gets a total occupation probability  $\sum_{cl} t_{cl}/t_{sim}$  of 75%. This is rather low for an interpretation in terms of a hopping model which on the other hand is supported by the fact that the total volume of all clusters is only 1.41% of the system's volume. The first 500 clusters have different characteristics than the rest which seem not to fit to the picture of sites in a hopping model. Problem (i) can be explained as follows: The criterion  $\rho(\mathbf{x}) > \rho_{th}$  cuts off the outer regions of a site. While the lithium number density on these fringes is low, their volume is not. Therefore they cannot be neglected if one wants to calculate the occupation probability of a site. The second problem is more subtle. The Hoshen-Kopelman algorithm identifies all isolated maxima in  $\rho(\mathbf{x})$  which are higher than the threshold value. Not all of them are necessarily sites in view of a hopping model. Some of them are just due to small fluctuations in  $\rho(\mathbf{x})$  in regions where  $\rho(\mathbf{x})$  is close to the threshold value, others may be caused by artifacts due to the discretised dynamics in the MD-simulation or the discretisation of  $\rho(\mathbf{x})$ . Other clusters could be due to maxima on the diffusion paths which are just regions of somewhat increased number density (e.g. an intersection in the path network) without Li ions residing there for longer times before going to another site. One has to use some exclusion criterion to get rid of those clusters which cannot be associated with a site.

In ref. [4] it was suggested to use a minimum occupation probability of 10% as a criterion for a cluster to be a site:

$$t_{cl}/t_{sim} > 0.1 . \quad (18)$$

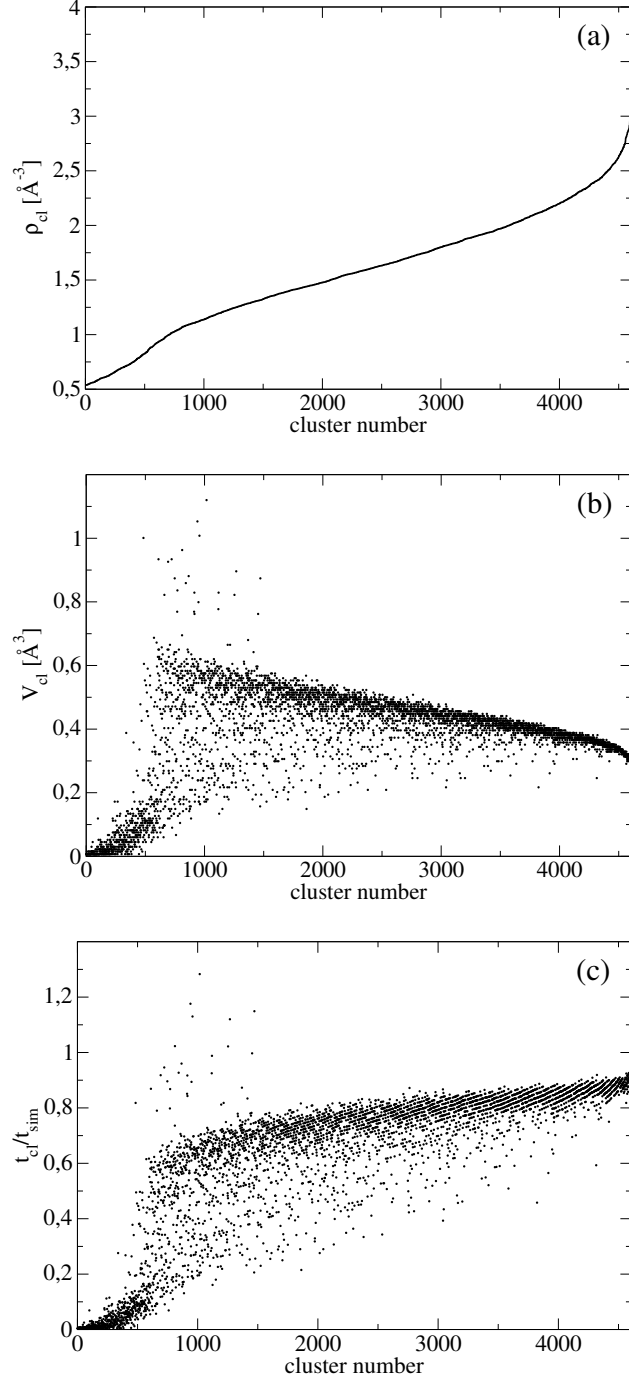


Figure 6: (a) Mean number density  $\rho_{cl}$  of Li ions on the 4608 clusters identified by the Hoshen-Kopelman algorithm; (b) Volume  $V_{cl}$  and (c) Li occupation probability  $t_{cl}/t_{sim}$  of the clusters. The clusters are sorted by increasing  $\rho_{cl}$ .

## 2 MOLECULAR DYNAMICS SIMULATIONS AND BOND VALENCE SUM CALCULATIONS

---

As it is possible that there are sites which are rarely visited but still show a long residence time of the visiting ions compared to the transition time to the neighbouring sites, we introduce another criterion for the assignment of clusters to sites. The total residence time  $t_{\text{res}}$  of lithium ions on a site is required to be 10 times larger than the total hopping time  $t_{\text{hop}}$  to any of its neighbours. In order to determine both the time that lithium ions spend outside of a cluster is counted. If it returns to the last cluster, which it had visited, that time is added to the residence time  $t_{\text{res}}$  of that cluster in addition to  $t_{\text{cl}}$ . Accordingly, the hopping time is determined by the time that ions spend between leaving one cluster and entering another cluster. This time is added to the total hopping time of the initial cluster.

As can be seen in figure 7,  $t_{\text{hop}}$  fluctuates from cluster to cluster, but in only one case it exceeds one tenth of the simulation time. For 3266 clusters the residence time is larger than  $0.9 t_{\text{sim}}$ . By summing over the residence times of all clusters it can be shown that a hopping model is indeed appropriate to describe the system as the total residence probability  $t_{\text{res}}/t_{\text{sim}}$  of the Li ions on the clusters is now 99%. The inclusion of the fringes of the clusters solves the problem with the low occupation probability of the clusters.

Clusters can now be assigned to sites by requiring that  $t_{\text{hop}}$  is at least an order of magnitude smaller than  $t_{\text{res}}$ :

$$t_{\text{res}}/t_{\text{hop}} > 10 . \quad (19)$$

Condition (19) is fulfilled by most clusters (see figure 7), only 368 fail to satisfy it. The majority of them have a small number corresponding to a low  $\rho_{\text{cl}}$  (see figure 6) and fulfil the alternative criterion (18) as well. To compare the different criteria more quantitative it is necessary to choose such threshold values that all conditions yield the same number of excluded clusters. When keeping condition (19) unchanged, the threshold value for the mean number density is 0.724 and the occupation probability has to be lower than 0.05.

Figure 8 shows the comparison of the criterion based on  $t_{\text{cl}}/t_{\text{sim}}$  and condition (19). All clusters in sector II satisfy both conditions, while the clusters in sector IV fail to satisfy either. The clusters in sector I and III are only sites according to one of the criteria. The distribution shown in the figure makes it clear that it is hard to define a unique criterion for the assignment of sites. The properties of the cluster change gradually from being occupied the whole time without any hopping taking place to being occupied less time than the ions spend with hopping to the neighbouring cluster. Table 2 lists the number of clusters, which satisfy the various combinations of conditions. 75% of the clusters excluded by (19) are also identified via the mean density threshold and criterion (18). This shows that there is actually not much difference between a criterion based on a threshold number

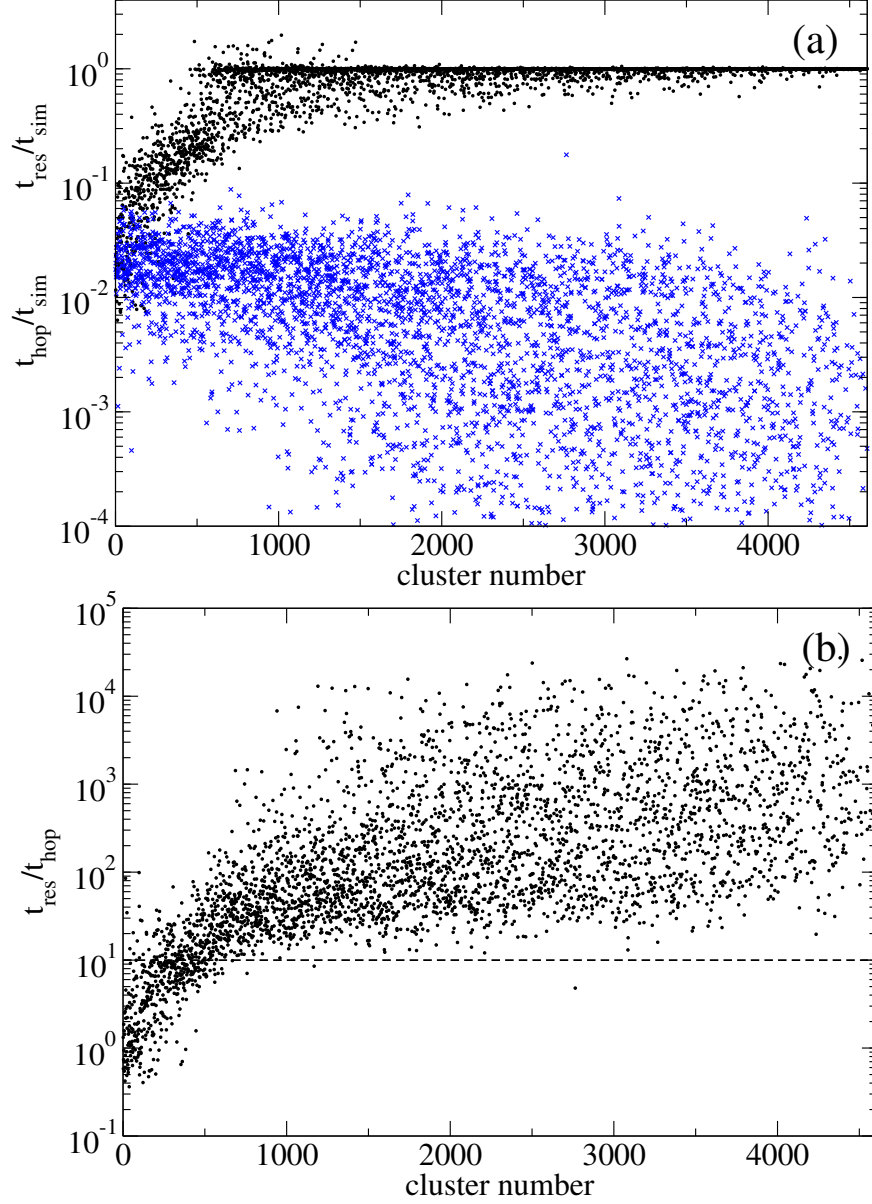


Figure 7: (a) Total residence time (black dots) and hopping time (blue cross) normalised with respect to the simulation time  $t_{\text{sim}}$ , and (b) their ratio for the 4608 clusters determined by the Hoshen-Kopelman algorithm. The dashed line marks the threshold above which clusters are identified as sites (cf. eq. (19)).

## 2 MOLECULAR DYNAMICS SIMULATIONS AND BOND VALENCE SUM CALCULATIONS

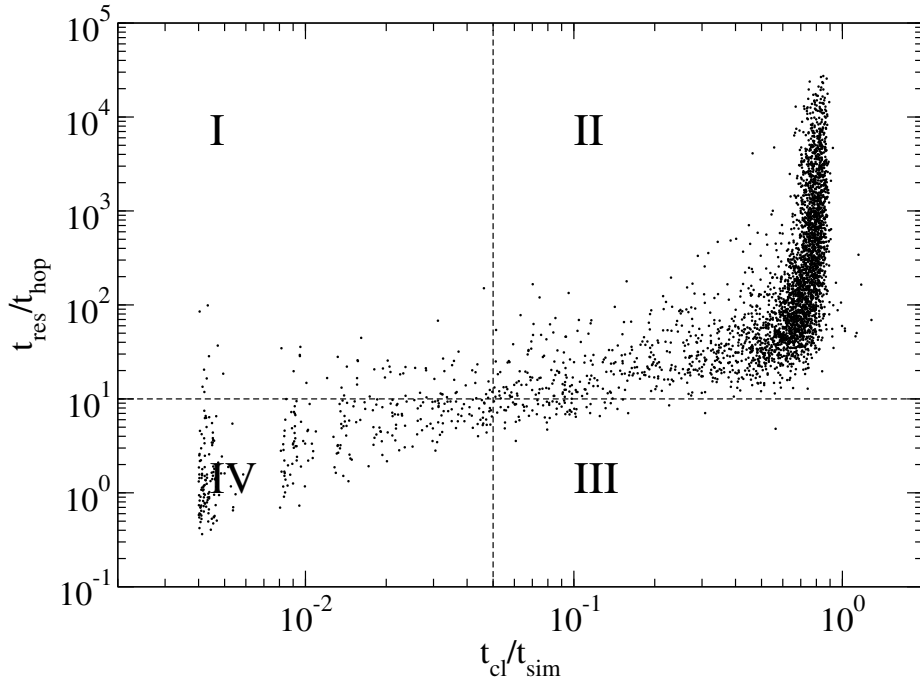


Figure 8: Comparison of threshold criteria for the assignment of sites based on  $t_{\text{res}}/t_{\text{hop}}$  and  $t_{\text{cl}}/t_{\text{sim}}$ . Clusters in sector II are sites according to both criteria, while clusters in sector IV are sites according to neither. Clusters in sector I and III are identified as sites by one of the criteria.

density, condition (18) and eq.(19). This confirms as well that the sites are determined essentially by the equilibrium quantity  $\rho(\mathbf{x})$  (when disregarding small non-equilibrium aging processes of the glass former network).

In the end we find 4240 sites which is 9% more than Li-ions in the system. This fraction is in accordance with numbers reported in other works. In contrast to crystalline systems this number is not only determined by the material composition but is largely determined by the cooling process and should not change anymore below the glass transition temperature.

After having determined the lithium sites we now address the question of how to identify the conduction pathway where long range diffusion of

Table 2: Number of clusters which fail to satisfy the various criteria to assign sites [ (i)  $\rho_{\text{cl}} < 0.724$  ; (ii)  $t_{\text{cl}}/t_{\text{sim}} > 0.05$  ; (iii)  $t_{\text{res}}/t_{\text{hop}} > 10$  ]

$(i);(ii);(iii)$	$(i)\wedge(ii)$	$(i)\wedge(iii)$	$(ii)\wedge(iii)$	$(i)\wedge(ii)\wedge(iii)$
368	330	296	302	276

Li ions is possible. Again  $\rho(\mathbf{x})$  is the quantity which allows us to do this. A straightforward definition of a diffusion path is given by the percolation threshold value for  $\rho_{\text{th}} = \rho_{\text{perc}} = 0.016 \text{ \AA}^{-3}$ . It is given by the largest  $\rho_{\text{th}}$  which produces a cluster with cells on two opposing sides of the system when performing the cluster analysis without periodic boundary conditions. Confining the Li motion to exactly the critical percolation path would yield anomalous subdiffusion, but in our case the percolation threshold is not sharp due to the finite system size. More important, such issues have no influence on an investigation of spatial overlap with BV paths as this criticality plays no role for it (the connectivity properties of the path are of no interest for the spatial overlap).

### 2.3 Bond valence sum calculations and BV path

The bond valence (BV) method is a pseudo-potential method which should allow one to determine favourable regions in space where particles reside within a matrix of other atoms. Its origins lie in the search of correlations between bond lengths, chemical valence and binding energies [33], and it has been applied to crystals with covalent and ionic bonds as well as metals. Especially ionic crystals have been investigated with good success. This motivates the application of the BV method to ionic glasses as well. In such amorphous systems it has been used to determine diffusion paths of the mobile ion species based on the knowledge of the glass network structure. In our lithium silicate systems this means that we determine the regions, where lithium ions can be favourably accommodated in a given Si-O host network. It is required that the valence of a Li ion is close to its 'natural value'. Additionally, constraints for its coordination number and for the minimal distances to the network ions have to be taken into account.

The basic idea of the Bond Valence method is to describe polar atom bonds. The different electronegativities of two atoms in close proximity induces charges of opposite sign in them. These induced partial charges are associated with the bond that connects the atoms and are called bond valence. They have been introduced by Pauling. In an equilibrated system they should add up to the ideal valence of an atom (i.e. +1 for a Li ion). Noting that the overlap of the electronic orbitals of two atoms decreases exponentially with the distance of the atomic nuclei, the partial valence  $s_j(\mathbf{x})$  of a Li ion at position  $\mathbf{x}$  induced by an oxygen ion  $j$  at position  $\mathbf{x}_j^O$  is determined by [34]

$$s_j(\mathbf{x}) = \exp \left[ \frac{r_0 - |\mathbf{x} - \mathbf{x}_j^O|}{\xi} \right], \quad (20)$$

where  $r_0$  is the ideal bond length depending on the types of atoms involved and  $\xi$  is the so-called softness parameter that determines how fast the bond

## 2 MOLECULAR DYNAMICS SIMULATIONS AND BOND VALENCE SUM CALCULATIONS

---

Table 3: Parameters used in the BV analysis.

$R_{\text{LiO}}$ [Å]	$R_{\text{LiSi}}$ [Å]	$\xi$ [Å]	$r_0$ [Å]	$s_{\text{min}}$	$C_{\text{min}}$	$C_{\text{max}}$	$\bar{V}$
1.70	2.48	0.516	1.17096	0.04	4	6	0.814

valence varies with distance. The total valence  $V(\mathbf{x})$  of a Li ion is computed as the sum of the bond valences  $s_j(\mathbf{x})$ :

$$V(\mathbf{x}) = \sum_j s_j(\mathbf{x}) = \sum_j \exp \left[ \frac{r_0 - |\mathbf{x} - \mathbf{x}_j^{\text{O}}|}{\xi} \right]. \quad (21)$$

Because of the exponential decay with distance the sum can be extended over all oxygen ions in the computational domain (taking into account the minimum image convention for periodic boundary conditions [35]). Here the principle of the BV method can easily be understood. If a lithium ion has one bond with the ideal bond length it prefers that all other bonds are so large that they do not contribute anymore to the valence sum, as the bond valence of that single bond is already +1, corresponding to the ideal valence. If there were two oxygen atoms nearby, the Li ion would prefer both of them to be a little bit further away than an ideal bond length would require. Both oxygen atoms then get a part of the spare electron density of the Li ion.

Using the partial valences a coordination number  $C(\mathbf{x})$  of a Li ion at position  $\mathbf{x}$  can be defined. It is given by the number of oxygens which are within a certain distance. As  $s(\mathbf{x})$  is a monoton function this distance can be directly mapped onto a minimum value  $s_{\text{min}}$  for the partial valence. The coordination number of a Li ion is then defined as the number of partial valences which exceed  $s_{\text{min}}$ :

$$C(\mathbf{x}) = \sum_j \theta(s_j(\mathbf{x}) - s_{\text{min}}) \quad (22)$$

where  $\theta(\cdot)$  is the Heaviside jump function ( $\theta(x) = 1$  for  $x > 0$  and zero otherwise). The parameters  $r_0$ ,  $\xi$ , and  $s_{\text{min}}$  are derived from a variety of crystal phases[36, 37] and are given in table 3.

While the ideal value for the valence of a Li ion is  $V_{\text{id}} = 1$  in crystalline systems, it is not clear whether that value is a valid choice in glass systems as well. In fact, the use of partial charges for the different ion species in MD-simulations of glasses make it plausible that it does not have to be whole-numbered.

As we know the trajectories of all ions from the MD-simulations we can directly determine an optimal value for the Li valence. From an instantaneous configuration we can calculate the distribution of valences for the

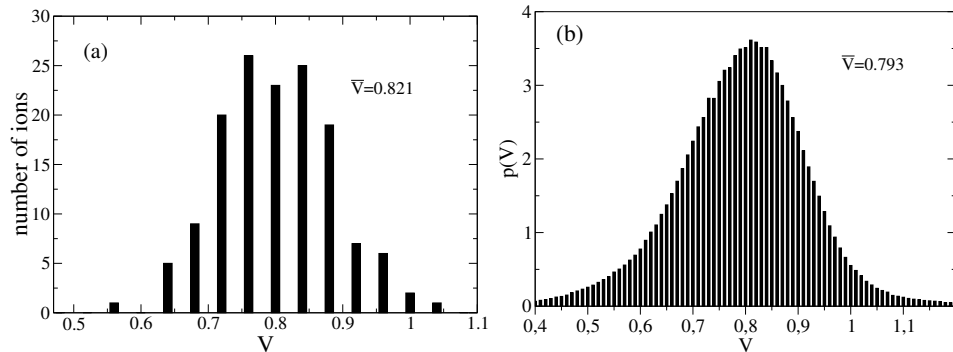


Figure 9: (a) Histogram of of bond valence sums for an instantaneous configuration of the equilibrated  $\text{Li}_2\text{SiO}_3$  glass; (b) Probability density of bond valence sums with respect to the time-averaged structure of network forming O and Si ions.

3888 lithium ions. Its histogram is shown in figure 9(a). The mean value  $V_{\text{inst}} = 0.821$  is smaller than the ideal value. Generally the BV analysis is used with structural data obtained from RMC calculations on the basis of neutron diffraction data. The RMC calculations provide atomic configurations which are in agreement with the diffraction data. As the diffraction data is a time averaged quantity in itself (at least on time scales of atomic vibrations) it is closer to the usual application of the Bond Valence method if we use time averaged data from the MD-simulations as well. Therefore we will determine the mean positions of the oxygen and silicon ions over a time interval of 2 ns and calculate the valences of the lithium ions with respect to these mean positions.

We can take all configurations of the system into account to determine the optimal valence in our MD-glass. To this end we calculate the valences  $V_i = V(\mathbf{x}_i)$  of a lithium ion placed at the centre  $\mathbf{x}_i$  of cell  $i$  as introduced in section 2.2 and calculate a distribution of valences  $p(V)$  under consideration of weighting factors given by the occupation probabilities  $\rho(\mathbf{x}_i)\Delta^3$  of the cells. The mean of this distribution shown in figure 9(b) is  $\bar{V} = 0.793$  and even smaller than that for the instantaneous configuration, supporting the conjecture that the ideal value  $V_{\text{id}} = 1$  is not the preferred one in amorphous glass structures. The distribution  $p(V)$  also reflects the correspondence of the bond valence method to other effective potential methods. It shows an asymmetry with a steeper decrease from the maximum to the side of larger valences. This corresponds to the asymmetry in the lithium-oxygen pair potentials, where a strong repulsive part prevents the undershooting of the minimal interatomic distances. Small distances yield large valences and are therefore less likely. In contrast small valences correspond to large distances, where the potential barrier is not as steep.

In the following we will analyse the data with respect to the time-

## 2 MOLECULAR DYNAMICS SIMULATIONS AND BOND VALENCE SUM CALCULATIONS

---

averaged network structure and consider  $\bar{V}$  as the 'optimal value' of the bond valence sum. The valence mismatch of a Li ion at position  $\mathbf{x}$  is then given by

$$d(\mathbf{x}) = |V(\mathbf{x}) - \bar{V}| . \quad (23)$$

We can also define a BV-path  $\mathcal{P}_{\text{BV}}(d_{\text{th}})$  as the union of all cells which are accessible for lithium ions according to the Bond Valence method, according to the following conditions [38]:

- (i) As the BV sum only involves interactions with the oxygen anions it is necessary to introduce an additional constraint to prevent unphysical proximity of lithium and silicon ions. Therefore we require that lithium cations have minimum distances to the silicon cations:

$$\min_j \{ |\mathbf{x} - \mathbf{x}_j^{\text{Si}}| \} > R_{\text{LiSi}} \quad (24)$$

where  $R_{\text{LiSi}} = 2.48 \text{ \AA}$  is chosen to be the sum of the Li and Si ion radii. One should note that this number is in agreement with the correlation hole of the pair distribution function as shown in fig. 3(a).

- (ii) Lithium cations must have minimum distances to the oxygen anions with  $R_{\text{LiO}} = 1.7 \text{ \AA}$ , in agreement with the correlation hole of the pair distribution function shown in fig. 3(a):

$$\min_j \{ |\mathbf{x} - \mathbf{x}_j^{\text{O}}| \} > R_{\text{LiO}} . \quad (25)$$

This prevents that the majority of the valence sum is contributed by a single bond, and therefore helps to achieve more symmetric coordination shells of oxygen ions around a lithium. The chosen minimum distance restricts the partial valence of a lithium-oxygen pair to values below 0.36.

- (iii) The coordination number of a lithium ion must lie between a maximum and a minimum value:

$$C_{\text{min}} \leq C(\mathbf{x}) \leq C_{\text{max}} \quad (26)$$

where  $C_{\text{min}} = 4$  and  $C_{\text{max}} = 6$ . This condition has previously been assumed for sites only [14].

- (iv) The valence mismatch must be smaller than a threshold value  $d_{\text{th}}$ :

$$d(\mathbf{x}) = |V(\mathbf{x}) - \bar{V}| < d_{\text{th}} . \quad (27)$$

As an alternative to the three conditions (ii-iv) one can use just one condition (v) which is a modification of (iv). It takes into account that a

Table 4: Volume fractions [%] of the various subsets specifying sites and diffusion paths.

$\mathcal{P}_{\text{sites}}$	$\mathcal{P}_{\text{perc}}$	$\mathcal{P}_{\text{ex}}^{\text{BV}}$	$\mathcal{P}_{\text{cn}}^{\text{BV}}$	$\mathcal{P}_{\text{ex+cn}}^{\text{BV}}$
1.4	7.5	10.0	80.0	7.7

Li ion is better accommodated to the local network environment at position  $\mathbf{x}$  if the valences  $s_j(\mathbf{x})$  are more symmetrically distributed among the neighbouring oxygen ions. The effect can be described by defining an “ideal partial valence”  $s_{\text{id}}$  by  $C_{\text{min}}s_{\text{id}} = V_{\text{id}}$  [14, 39], corresponding to a Li ion that, when symmetrically connected to  $C_{\text{min}}$  oxygen ions, has the ideal total valence  $V_{\text{id}}$ . The deviation from the symmetric situation is quantified by the penalty function

$$p(\mathbf{x}) = \sqrt{\sum_j \left( \frac{s_j(\mathbf{x})}{s_{\text{id}}} - 1 \right)^{2\mu}} . \quad (28)$$

where the sum is taken over all oxygen ions with  $s_j(\mathbf{x}) > s_{\text{id}}$  and we choose  $\mu = 3$  as suggested in ref. [39]. A modified valence is then defined by  $d'(\mathbf{x}) = d(\mathbf{x}) + p(\mathbf{x})$  and we require:

- (v) The modified valence mismatch must be smaller than a threshold value  $d_{\text{th}}$ :

$$d'(\mathbf{x}) = |V(\mathbf{x}) - \bar{V}| + p(\mathbf{x}) < d_{\text{th}} . \quad (29)$$

As a consequence of replacing conditions (ii) and (iii) with condition (v), instead of the four parameters  $R_{\text{LiO}}$ ,  $C_{\text{min}}$ ,  $C_{\text{max}}$ , and  $s_{\text{min}}$  the parameter  $\mu$  enters the calculation. Thus we get an alternative definition of the BV path by applying conditions (i) and (v) which we refer to as  $\mathcal{P}'_{\text{BV}}(d_{\text{th}})$ .

For a more detailed analysis of the influence of these conditions it is useful to define different supersets of the BV-path by applying conditions (i-iii) separately.  $\mathcal{P}_{\text{ex}}^{\text{BV}}$  denotes the subset of cells which fulfil the purely geometric conditions (i) and (ii). It corresponds to a hard sphere model. Applying condition (iii) defines  $\mathcal{P}_{\text{cn}}^{\text{BV}}$ . A third subset  $\mathcal{P}_{\text{ex+cn}}^{\text{BV}}$  is given by the intersection of  $\mathcal{P}_{\text{ex}}^{\text{BV}}$  and  $\mathcal{P}_{\text{cn}}^{\text{BV}}$  respectively by applying conditions (i-iii) at the same time. It is also the BV path  $\mathcal{P}_{\text{BV}}(d_{\text{th}})$  in the limit  $d_{\text{th}} \rightarrow \infty$ .

Already the geometric constraints (i,ii) limit the accessible space for the mobile ions to 10% of the total volume, see table 4. It is the most restrictive limitation. In contrast, condition (iii) alone restricts the accessible volume only to 80%. Interestingly, conditions (i,ii) and (iii) seem to be uncorrelated as the volume of  $\mathcal{P}_{\text{ex+cn}}^{\text{BV}}$  is 7.7% of the total system volume. This is surprising as one would expect the spatial regions within the exclusion radius around the oxygen atoms to have a bad coordination for the lithium ions. Replacing

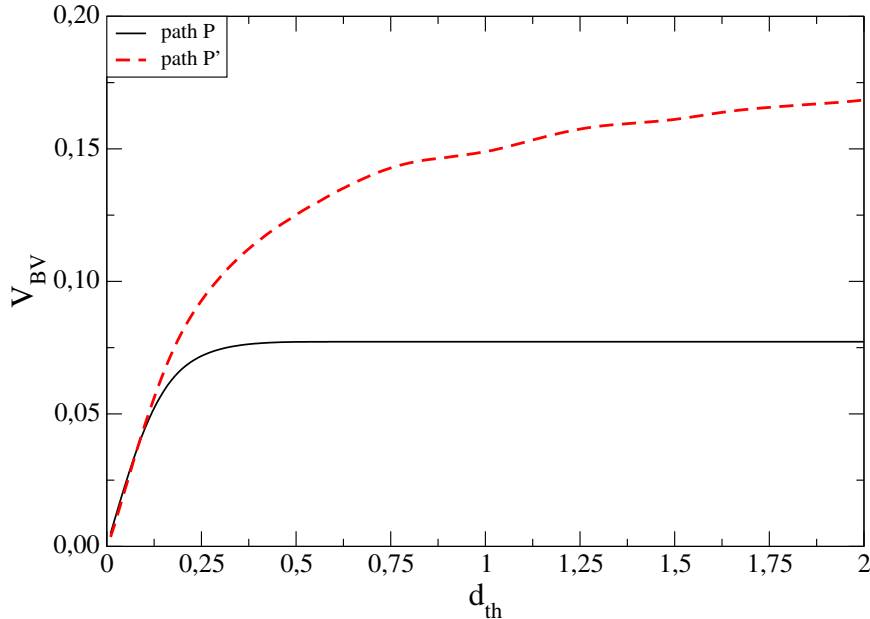


Figure 10: Volume fraction  $v_{BV}$  of the BV path as a functions of the mismatch threshold  $d_{th}$ .

constraints (ii-iv) with condition (v) yields a path which includes 18.8% of the system volume in the limit  $d_{th} \rightarrow \infty$  (also see fig. 10). If one expects  $\mathcal{P}_{BV}(d_{th})$  to be a good representation of the favourable regions in the glass network where lithium ions reside, the BV-paths  $\mathcal{P}_{\star}^{BV}$  ( $\star = \text{ex}; \text{cn}; \text{ex} + \text{cn}$ ) should entail the MD-paths  $\mathcal{P}_{\text{perc}}$  and  $\mathcal{P}_{\text{sites}}$ , as they are supersets of  $\mathcal{P}_{BV}(d_{th})$ .

## 2.4 Comparison of MD and BV ion pathways

In order to quantify the agreement between the MD and BV paths we calculate two quantities which we call the sensitivity and specificity. The sensitivity is the conditional probability  $\psi(\mathcal{P}_{\star}^{BV} | \mathcal{P}_{\star\star})$  that a cell belonging to one of the subsets identified in the MD-simulations belongs to one of the subsets of the BV analysis ( $\star = \text{cn}, \text{ex}, \text{cn} + \text{ex}$ ;  $\star\star = \text{sites}, \text{perc}$ ). In other words, it gives the fraction of how much of the MD paths  $\mathcal{P}_{\star\star}$  is part of the BV path  $\mathcal{P}_{\star}^{BV}$ . Conversely, the specificity of the BV analysis is quantified by calculating the conditional probabilities  $\psi(\mathcal{P}_{\star\star} | \mathcal{P}_{\star}^{BV})$ . It tells us how much of the BV path  $\mathcal{P}_{\star}^{BV}$  actually belongs to the MD path [40].

In table 5 the sensitivity and specificity are shown for the three supersets of  $\mathcal{P}^{BV}$ . Let us first consider  $\mathcal{P}_{cn}^{BV}$ . The sensitivity is higher than 0.9 for both MD paths. But this is not very surprising as  $\mathcal{P}_{cn}^{BV}$  entails 57 times more volume than  $\mathcal{P}_{\text{sites}}$  and still 11 times as much volume as  $\mathcal{P}_{\text{perc}}$ . Accordingly,

Table 5: Comparison of the subsets determined by the BV analysis according to criteria (*i-iii*) with the sites and diffusion paths identified from the MD-simulations. Upper part: Sensitivities  $\psi(\mathcal{P}_\star^{\text{BV}}|\mathcal{P}_\star)$ ; lower part: specificities  $\psi(\mathcal{P}_\star|\mathcal{P}_\star^{\text{BV}})$ .

	$\mathcal{P}_{\text{ex}}^{\text{BV}}$	$\mathcal{P}_{\text{cn}}^{\text{BV}}$	$\mathcal{P}_{\text{ex+cn}}^{\text{BV}}$
$\mathcal{P}_{\text{sites}}$	0.80	0.89	0.71
$\mathcal{P}_{\text{perc}}$	0.57	0.84	0.48
$\mathcal{P}_{\text{sites}}$	0.11	0.02	0.13
$\mathcal{P}_{\text{perc}}$	0.43	0.09	0.48

the specificities are very low and actually not much higher than the values one would expect for uncorrelated behaviour.

A strong correlation can be seen between the MD paths and  $\mathcal{P}_{\text{ex}}^{\text{BV}}$ . Still, it might be surprising that the sensitivity for the percolation path is only 0.57. This means that the exclusion radius constraints are violated rather often. But here we should consider that we used time averaged positions of the network ions for the comparison. This can lead to the troublesome violation of exclusion radii, as it does not take into account the possibility of network atoms moving aside to let lithium atoms slip through to the next site.

Applying condition (*i-iii*) at the same time improves the results only slightly. The highest increase can be seen in the specificity against the percolation path  $\mathcal{P}_{\text{perc}}$ . It is increased from 0.43 to 0.48. The question is whether the specificity can be improved without significant reduction in the sensitivity by applying condition (*iv*) in addition to (*i-iii*). Investigating the volume fraction  $v_{\text{BV}}$  of  $\mathcal{P}^{\text{BV}}(d_{\text{th}})$  of the full system yields that already at a threshold mismatch of  $d_{\text{th}} = 0.3$  the saturation limit for the volume given by applying constraints (*i-iii*) is reached after a linear increase between  $d_{\text{th}} = 0$  and  $d_{\text{th}} = 0.1$  (see Fig. 10). Accordingly, the sensitivities shown in figures 11(a) and (b) saturate for  $d_{\text{th}} > 0.3$  as well, a value in fair agreement with typical choices used in BV analyses of RMC models [41]. Between  $d_{\text{th}} = 0.15$  and  $d_{\text{th}} = 0.03$  an almost exponential decay of the sensitivity can be seen for both the comparison with  $\mathcal{P}_{\text{sites}}$  as well as  $\mathcal{P}_{\text{perc}}$ . Accepting such a strong loss in sensitivity does not yield a significant increase in the specificity. For the sites it is increased from 0.13 in the limit  $d_{\text{th}} \rightarrow \infty$  to 0.15 for  $d_{\text{th}} \rightarrow 0$ , for the diffusion path it is increased from 0.48 to 0.51.

Summarising the above, we note that most of the agreement between the MD paths and the BV path is gained by applying the purely geometric constraints (*i*) and (*ii*).

To find an optimal value for  $d_{\text{th}}$  nevertheless we calculate Cohen's kappa

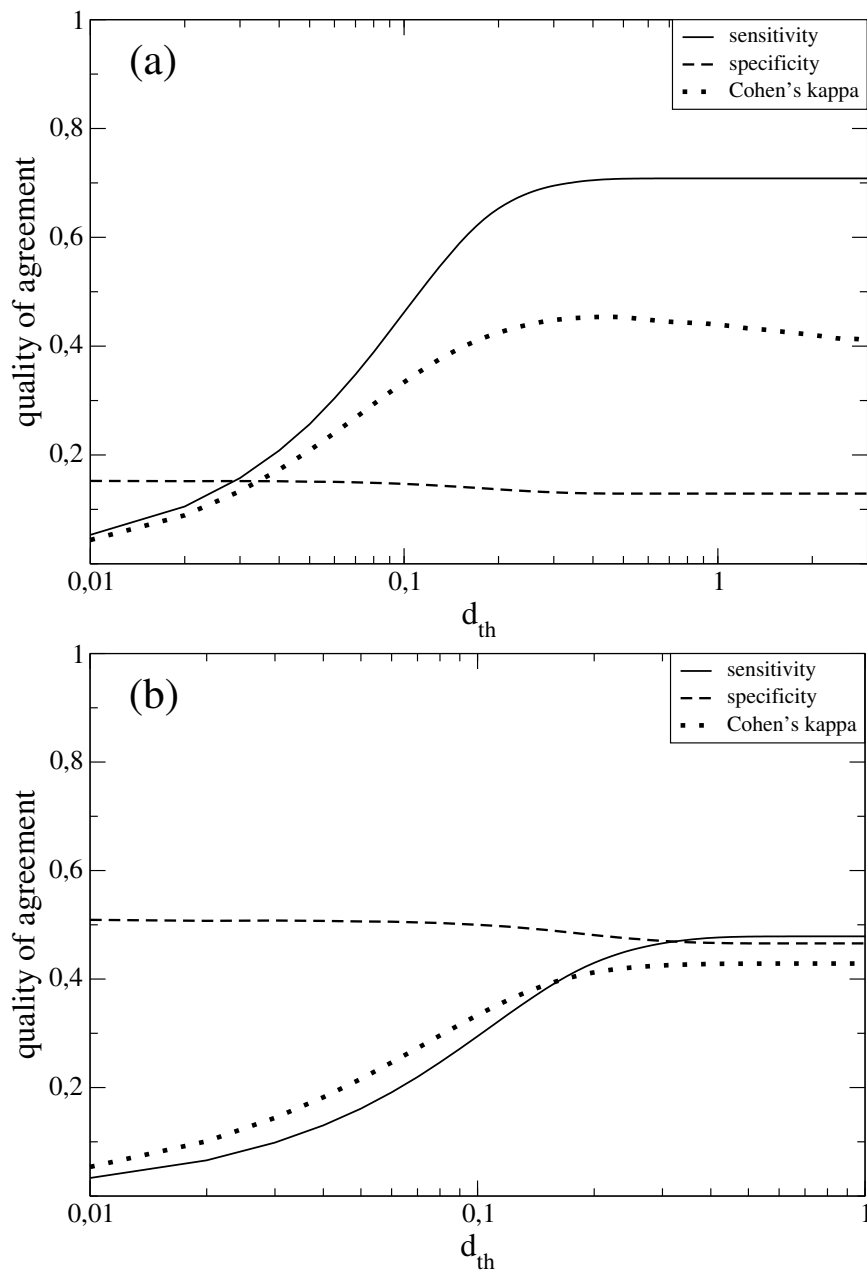


Figure 11: Quality of agreement between (a) the subsets  $\mathcal{P}_{sites}$  and  $\mathcal{P}_{BV}(d_{th})$ , and (b) the subsets  $\mathcal{P}_{path}$  and  $\mathcal{P}_{BV}(d_{th})$ .

value which is also a measure for the agreement of two sets [42]. The kappa value for the sets  $\mathcal{A} = \mathcal{P}^{\text{BV}}(d)$  and  $\mathcal{B} = \mathcal{P}_\star$  is defined by

$$\kappa = \frac{(p(\mathcal{A} \cap \mathcal{B}) + p(\bar{\mathcal{A}} \cap \bar{\mathcal{B}})) - (p(\mathcal{A})p(\mathcal{B}) + p(\bar{\mathcal{A}})p(\bar{\mathcal{B}}))}{1 - (p(\mathcal{A})p(\mathcal{B}) + p(\bar{\mathcal{A}})p(\bar{\mathcal{B}}))}, \quad (30)$$

where  $p(\cdot)$  denote the probabilities of the corresponding sets (for example,  $p(\mathcal{A} \cap \mathcal{B})$  is the probability that a cell belongs to both the sets  $\mathcal{A}$  and  $\mathcal{B}$ ). A value of  $\kappa = 1$  denotes complete agreement between the two sets, while  $\kappa = 0$  corresponds to a random overlap of the two sets (negative values indicate an anti-correlation). The maximum of  $\kappa$  occurs for the sites at  $d_{th} = 0.09$  and is only 25%. Such a low value shows, as well as the low specificity, that the BV method is not suitable for identifying sites. This is slightly different for the diffusion path. Here a maximum value  $\kappa = 0.42$  is reached for  $d_{th} > 0.25$ . While this value shows a promising agreement between the BV path and the percolation path one should note that this is mainly caused by the exclusion radii and therefore is a rather trivial result.

The alternative condition (*v*), which replaces (*ii-iv*), can increase the sensitivity and the specificity by softening the exclusion radius constraint around the oxygen atoms. This can be seen in fig. 10 where the volume of  $\mathcal{P}'_{\text{BV}}(d_{th})$  already increases to 0.12 for  $d_{th} = 0.4$ . Accordingly, the sensitivity for this path in comparison with  $\mathcal{P}_{\text{perc}}$  plotted in fig. 12 reaches much higher values of up to 0.8 for very large  $d_{th} > 2$ . While this value is as large as the sensitivity obtained for  $\mathcal{P}_{\text{cn}}^{\text{BV}}$  with respect to the percolation path, the specificity is still 0.33 and therefore almost 4 times as large as for  $\mathcal{P}_{\text{cn}}^{\text{BV}}$ . This shows that the penalty function introduced in eqs.(28,29) softens the constraint for a Li ion to exhibit minimal distances to all neighbouring oxygen ions, while putting more emphasis on good overall chemical bonding conditions to the oxygen ions. Accordingly, one may expect that further enhancements of kappa may be achieved by replacing the hard sphere exclusion criterion (*i*) with a penalty function as well.

One can still ask whether it is possible to identify sites with the BV method by using a cluster analysis similar to the one used in sec. 2.2 despite the low specificity. While we searched for maxima in  $\rho(\mathbf{x})$  we now want to find minima in  $d(\mathbf{x})$ . Accordingly, one expects a coalescence of clusters for large  $d_{th}$  while small values of  $d_{th}$  correspond to large ones of  $\rho_{th}$ . Figure 13 shows the number of clusters in dependence of  $d_{th}$ . For small  $d_{th}$ , ten times as many clusters are found as lithium atoms are in the system. Increasing  $d_{th}$  to 0.1 leads to a strong reduction to about 10000 clusters due to coalescence. This is still more than two times as many clusters as were found in the analysis of  $\rho(\mathbf{x})$ . The reason for this behaviour is that the valence mismatch  $d(\mathbf{x})$  is a rather rapidly varying function. One measure to quantify this is to find the number of extrema in a function.

In fig. 14 the local minima of  $d(\mathbf{x})$  and the local maxima of  $\rho(\mathbf{x})$  from a 1.564 Å thick layer of the simulation box projected on a reference plane are

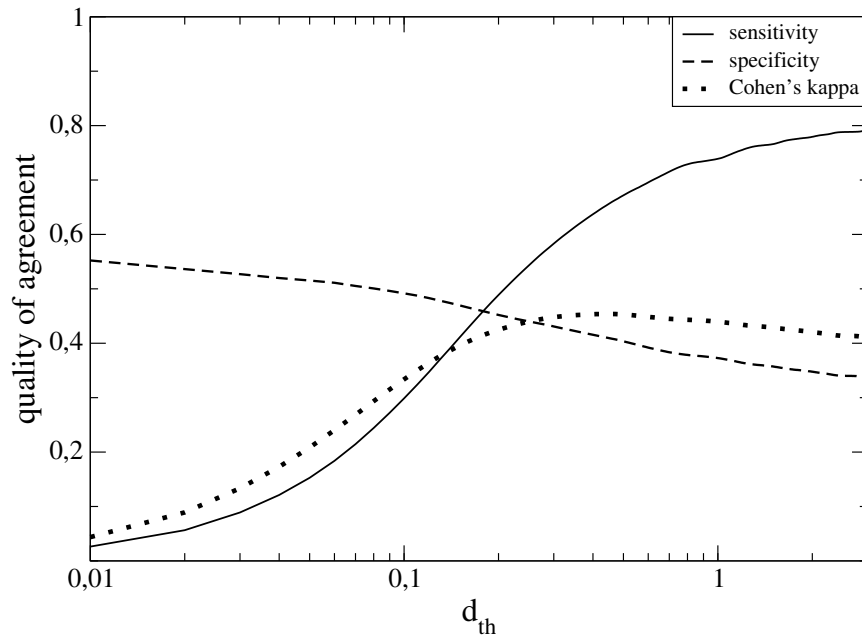


Figure 12: Quality of agreement between the percolation path  $\mathcal{P}_{perc}$  and  $\mathcal{P}'_{BV}(d_{th})$  as a function of the BV mismatch threshold  $d_{th}$ .

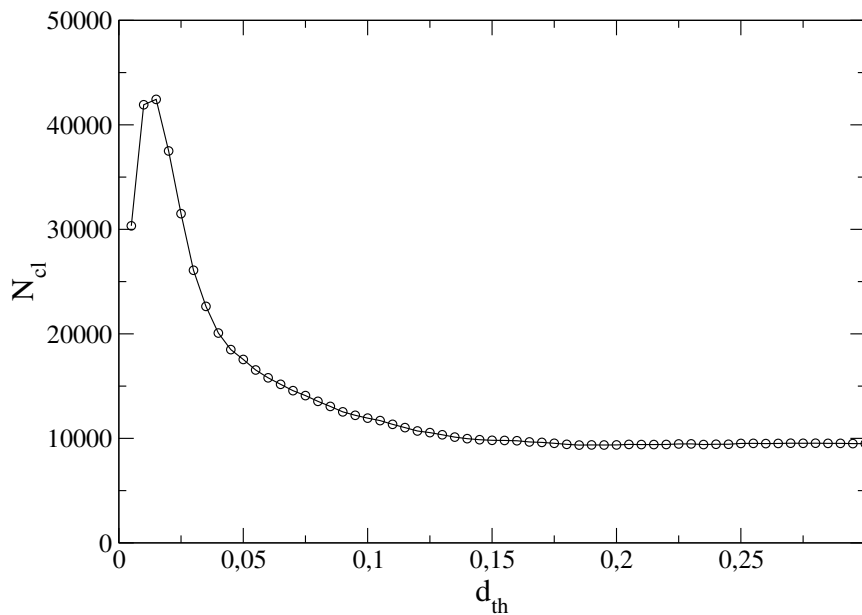


Figure 13: Number of BV clusters as a function of the threshold mismatch  $d_{th}$ .

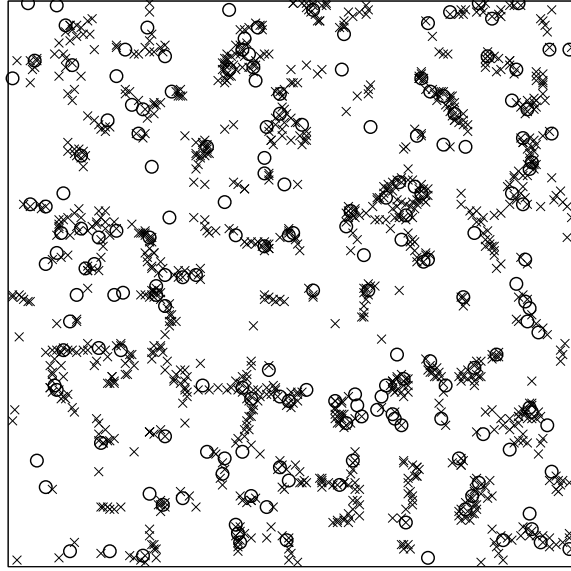


Figure 14: Projection of local maxima of  $\rho(\mathbf{x})$  ( $\circ$ ) and local minima of  $d(\mathbf{x})$  ( $\times$ ) in a three-dimensional layer with thickness  $1.564 \text{ \AA}$  (corresponding to 3.1% of the simulation box) onto a reference plane.

shown (the same layer as in fig. 5). It is found that there are more than five times as many minima in  $d(\mathbf{x})$  (37470 in the total system) as there are maxima in  $\rho(\mathbf{x})$  (6790 in the total system). Interestingly, the percolation threshold of the BV path is  $d_{\text{perc}} = 0.09$  and the percolation cluster includes 95% of  $v_{\text{BV}}(d_{th} = 0.1)$ . Accordingly, almost all found clusters are very small. Due to the rapid spatial fluctuations in  $d(\mathbf{x})$  there are still several thousands of clusters found but 80% of them consist only of a single cell, and only 85 of them are larger than 100 cells and therefore as large as typical clusters in the MD path analysis. As a consequence the cluster analysis is not successful in identifying sites based on  $d(\mathbf{x})$ .

### 3 Raman spectroscopy on thin film salt glasses

#### 3.1 Basics of Raman spectroscopy

Raman spectroscopy is based on the homonymous effect which was found by the Indian physician Raman in 1928. Most photons scattered by molecules or solid state materials are scattered elastically, i.e. the energy of the incident photon  $E_0 = \hbar\omega_0$  equals the energy of the scattered photon. However, a small fraction (approximately  $10^{-10}$ ) of the photons is scattered inelastically and gives rise to photons with lower or higher energy than the incident photon:

$$E_\nu = \hbar(\omega_0 \pm \omega_\nu) . \quad (31)$$

When the light source is monochromatic (more exactly if the spectral width of the incident light beam is smaller than  $\omega_\nu$ ) the inelastic photons can be observed as Stokes lines ('-' in eq. (31) ) and anti-Stokes lines ('+' in eq. (31) ) in the scattered spectrum. They result from inelastic scattering involving the excitation or deexcitation of the molecule respectively the creation or annihilation of phonons in a solid state material. Thus  $\omega_\nu$  provides information about the possible vibrational states of a material and can be used to analyse its structure.

The anti-Stokes lines are less intense than the Stokes lines as the probability to find a molecule in an excited vibrational state is lower than to find it in its ground state. Therefore the intensity ratio of an anti-Stokes line to the corresponding Stokes line is (in a first approximation) given by

$$\frac{I_{\nu,as}}{I_{\nu,s}} = e^{-\frac{\hbar\omega_\nu}{k_B T}} . \quad (32)$$

Not all molecular vibrations give rise to Raman scattered photons. The selection rules for Raman scattering state that the square of the derivative of the polarisability  $\alpha$  in respect to the normal coordinates  $q$  of a normal mode is proportional to the intensity of the corresponding Raman line

$$I_\nu \propto \left( \frac{\partial \alpha}{\partial q} \right)^2 . \quad (33)$$

As most vibrations in a material are directly defined by its local structure, an analysis of the Raman spectra allows insight into structural properties. In crystalline materials the Raman lines are very sharp, in glasses they are much broader. The amorphous character of glasses leads to variable local surroundings of the basic units of the structure, and therefore slightly different frequencies of the same basic type of vibrations. Nevertheless most structural models for glasses have been developed based on Raman and infrared spectroscopy, as diffraction methods, which also provide information about structural properties, do not work well with glasses.

The direct dependency of the Raman and infrared spectra on (mainly) the local structure also make this the best experimental data available which one can compare with data obtained from simulations in order to test the quality of the simulated structures.

Here Raman spectra of a LISON thin film glass are measured which were prepared by Y. Hamon at the École Nationale Supérieure de Chimie et Physique de Bordeaux. These measurements shall allow for the evaluation of LISON clusters calculated with *ab initio* methods (see sec. 4).

### 3.2 Experimental procedure

The experiment was performed using a standard micro Raman setup as shown in fig. 15. The light of an argon-krypton laser was mono-chromatised by a lattice monochromatiser and then linearly polarised. It was guided into a microscope that focuses the incident laser light onto the sample surface. The sample table could be moved vertically with a resolution of  $0.1 \mu\text{m}$  which allows one to focus the laser light within the thin films. The reflected light is collected by the microscope and guided into a second spectrometer. Using a camera, the intensity of the scattered light in dependence of the wavelength is measured and sent to a computer. Since the intensity is very low it is necessary to cool down the camera to liquid nitrogen temperature to reduce the dark current in the ccd elements of the camera. The laser was tuned to the 514 nm excitation line with a nominal output power of 300 mW. The power at the samples was 21 mW for the depolarised configuration, where the polarisation direction of the incoming beam is perpendicular with respect to the polarizer in front of the detector. For the polarised setup, where the polarisation direction of the incoming beam is parallel with respect to the polarizer in front of the detector, it was 7 mW. All samples have been kept under inert gas (Argon) conditions. From their storage within a glove box they were transferred into an inert gas sample box in which they were kept during the measurements.

Due to the limited thickness of the films ( $4 - 6 \mu\text{m}$ ) a strong signal of the substrate was observed. While this poses no problem for the films on gold, the silicon substrate has a very strong Raman response which renders it difficult to identify the Raman lines of the thin film glasses. Therefore it was necessary to perform measurements on a reference silicon sample, using the same experimental setup. This enabled us to subtract the substrate signal from the measured spectra later and thus to obtain the pure film signal.

Using the polarisation dependency of the  $521 \text{ cm}^{-1}$  Raman line intensity of silicon<sup>1</sup> it was ensured that the samples with a silicon substrate always

---

<sup>1</sup>The  $521 \text{ cm}^{-1}$  Raman line intensity is minimal for a  $45^\circ$  orientation of the sample with respect to the polarisation direction of the incoming light, when using the parallel polarisation setup.

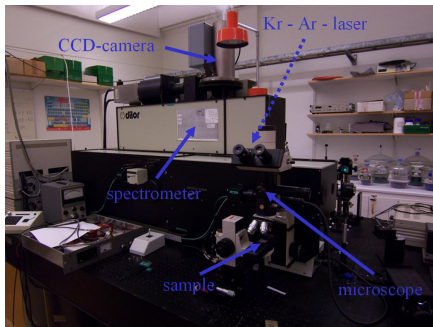


Figure 15: Photo of the Raman setup.

had the same orientation with respect to the incident polarisation.

### 3.3 Results

Figure 16 shows (a) the polarised and (b) depolarised Raman spectra for the LISON film. The bare silicon (dashed line) and the sample spectrum (film plus substrate, solid line) are shown in the insets of figs. 16(a),(b). The bare silicon spectrum was scaled to fit the characteristics between  $250\text{ cm}^{-1}$  and  $350\text{ cm}^{-1}$ . Measurements on different spots of the sample gave the same spectrum (see fig. 17). The main feature of the resulting difference spectra in figs. 16(a),(b) is a band between  $900\text{ cm}^{-1}$  and  $1035\text{ cm}^{-1}$ . A second weaker band is found at  $1225\text{ cm}^{-1}$ , with a shoulder at slightly lower frequencies around  $1150\text{ cm}^{-1}$  in the polarised spectrum in fig. 16(a). In addition, two more bands may be discerned at  $415\text{ cm}^{-1}$  and at  $645\text{ cm}^{-1}$ , in particular in the case of the polarised spectrum, where the intense silicon mode at  $521\text{ cm}^{-1}$  is absent and does not hamper the subtraction procedure. The intensity gap between  $440\text{ cm}^{-1}$  and  $500\text{ cm}^{-1}$  in the depolarised spectrum results from the fact that the integration time had to be chosen sufficiently large, in order to resolve the weak difference signals. As a consequence, the intensity of the silicon mode at  $521\text{ cm}^{-1}$  in the depolarised spectrum (see inset in fig. 16(b)) saturates the detector in this spectral region.

In order to interpret the bands originating from the LISON film in the difference spectra in fig. 16, we compare the results to the Raman modes

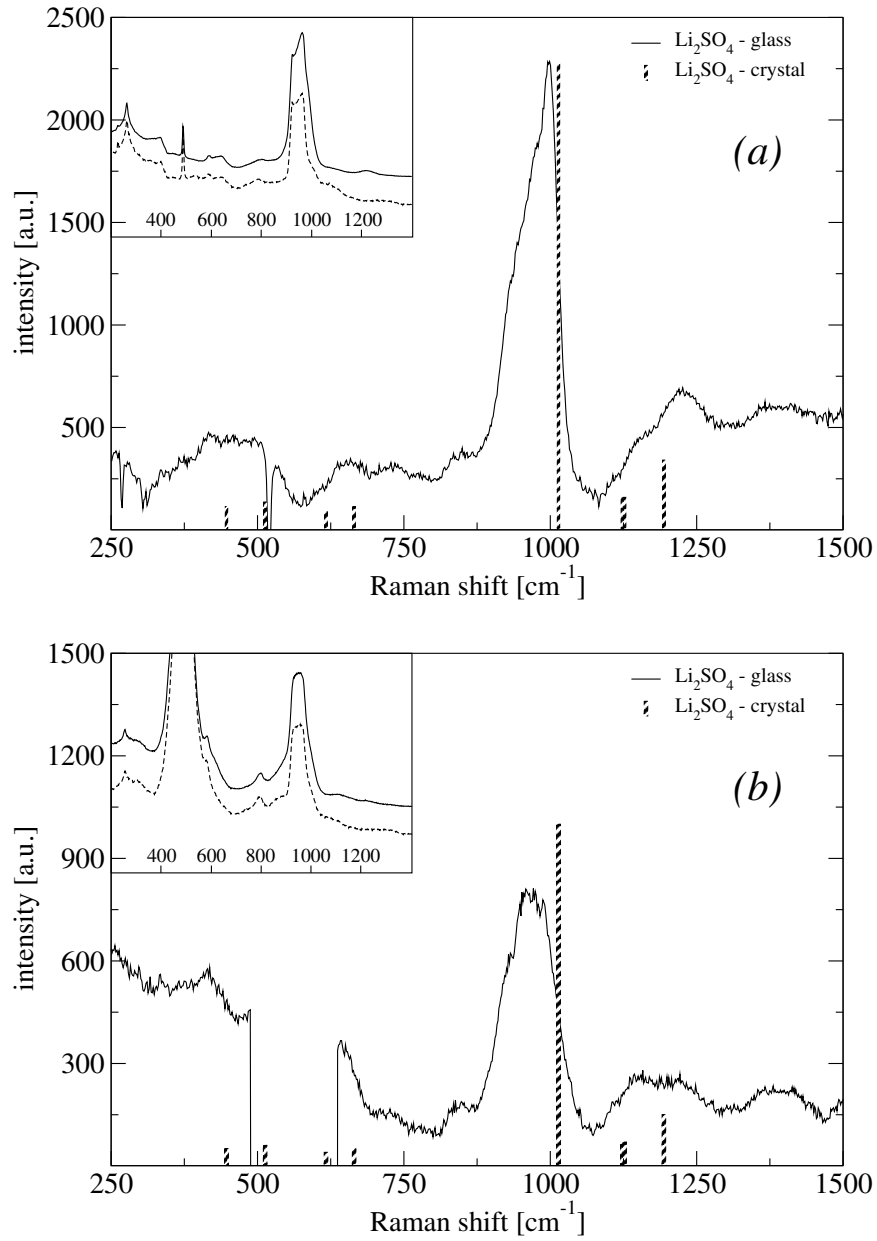


Figure 16: (a) Polarized and (b) depolarised difference Raman spectra of LISON films on a silicon substrate. The difference signal is obtained by subtracting the spectrum of a bare silicon substrate from the spectrum of the sample. The insets show the raw data from the sample and the substrate (dashed lines: silicon, solid lines: LISON film sample). The spectra have been offset for clarity.

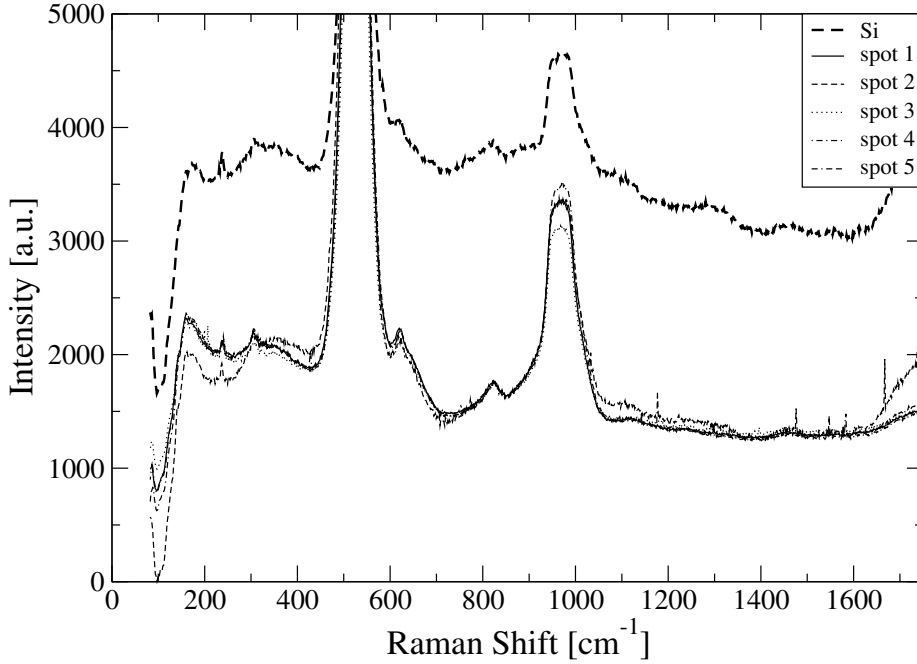


Figure 17:  $Li_2SO_4$  depolarised spectrum on different spots.

found in crystalline  $Li_2SO_4$  [43], marked as bars in the figure. The Raman spectrum of the crystal is dominated by the symmetric breathing mode of  $SO_4^{2-}$  at  $1014\text{ cm}^{-1}$  which either is very weak or found at lower frequencies in the glassy film. That this main band covers a range of frequencies where there are no corresponding modes from the crystal suggests that the structure of the amorphous LISON film and the  $Li_2SO_4$  crystal are different on short length scales, too. The modes at  $1123\text{ cm}^{-1}$  and  $1127\text{ cm}^{-1}$  in the crystal (appearing as a single bar in figs. 16(a), (b) due to their small separation), as well as the mode at  $1194\text{ cm}^{-1}$  seem to be shifted to higher frequencies and can be related to the bands around  $1150\text{ cm}^{-1}$  and around  $1225\text{ cm}^{-1}$  in the experimental spectrum. Similarly, the two bands in the film around  $415\text{ cm}^{-1}$  and  $645\text{ cm}^{-1}$  likely have their origin in the pair of modes at  $447\text{ cm}^{-1}$ ,  $513\text{ cm}^{-1}$  and the pair of modes at  $617\text{ cm}^{-1}$ ,  $665\text{ cm}^{-1}$  in the crystal respectively.



## 4 Ab initio calculations

### 4.1 Molecular orbital theory

Molecular orbital theory addresses the task of calculating properties of atomic configuration based on quantum mechanics. Electrons are represented by wave functions, the so-called molecular orbitals. The nature of molecules makes this a many-particle problem as interactions between the nuclei of the atoms and the electrons are involved.

The fundament for any molecular orbital theory is the time independent Schrödinger equation

$$H\Phi = E\Phi \quad (34)$$

where  $H$  is the Hamiltonian operator and  $E$  the energy of the system in the eigenstate described by the wave function  $\Phi$ . In order to describe molecular systems, typically five contributions are taken into account in the molecular Hamiltonian operator: the kinetic energy of the nuclei and the electrons, the internuclear and interelectronic repulsion and the attraction of the electrons to the nuclei

$$H = - \sum_k \frac{\hbar^2}{2m_K} \nabla_k^2 - \sum_i \frac{\hbar^2}{2m_e} \nabla_i^2 + \sum_{k<l} \frac{e^2 Z_k Z_l}{r_{kl}} + \sum_{i<j} \frac{e^2}{r_{ij}} - \sum_k \sum_i \frac{e^2 Z_k}{r_{ki}} . \quad (35)$$

In more complicate situations, e.g. where external electro-magnetic fields have to be taken into account, additional terms are required. Approximations are needed to find solutions (the eigenvalues and eigenvectors of  $H$ ) for such many-particle systems. The most important one is the Born-Oppenheimer approximation. Considering that the mass of the nucleus of an atom is three to five orders of magnitude larger than that of the electrons, one can assume that the relaxation of the electrons is instantaneous with respect to that of the nuclei. Thus the electronic Schrödinger equation is obtained, where the nuclei coordinates  $\mathbf{q}_k$  enter as parameters instead of being independent variables as the coordinates of the electrons  $\mathbf{q}_i$ :

$$(H_{\text{el}} + V_N)\Phi_{\text{el}}(\mathbf{q}_i; \mathbf{q}_k) = E_{\text{el}}(\mathbf{q}_k)\Phi_{\text{el}}(\mathbf{q}_i; \mathbf{q}_k) . \quad (36)$$

The electronic Hamiltonian  $H_{\text{el}}$  only includes the second, fourth, and fifth term on the r.h.s of eq. (35), while the (classical) nuclear-nuclear repulsion is included in  $V_N$ . Note that  $V_N$  is a constant for a given set of nuclei coordinates. This equation also provides the concept of the potential energy surface (PES) which is the electronic energy  $E_{\text{el}}(\mathbf{q}_k)$  with  $\mathbf{q}_k$  as independent variables. This allows for terms such as 'nearby minimum' when speaking of the energy of a molecule in dependence of the nuclei coordinates. In principle a distance between two configurations of the same molecule can be defined as the length of the difference vector between the two supervectors of all nuclei coordinates.

In the following only the electronic Schrödinger equation will be discussed. For the ease of notation the subscript 'el' will be dropped and only real valued wavefunctions are discussed. The latter is motivated by the fact that only real valued wavefunctions are used for computational ground state calculations, as the ones performed in this work.

Let us define the following functional:

$$\xi(\Phi) = \frac{\int \Phi H \Phi d\mathbf{r}}{\int \Phi^2 d\mathbf{r}} . \quad (37)$$

The variational principle of quantum mechanics states that

$$\xi(\Phi) \geq E_0 \quad (38)$$

where  $E_0$  is the ground state energy. Furthermore,  $\xi(\Phi) = E_0$  is only the case if  $\Phi$  is the ground state wavefunction of the system.

This Ritz inequality allows us to judge the quality of a candidate ground state wave function in comparison with another. The lower  $\xi(\Phi)$  is the better is the real ground state wave function approximated by the candidate wave function. It is important to note that eq. (38) holds true not only for eigenfunctions of  $H$  but for any arbitrary wave function  $\Phi$ .

Before discussing how to obtain many electron wave functions, it is instructive to consider the one-electron problem. One of the most common approaches to construct one-electron trial wave functions is the so-called linear combination of atomic orbitals (LCAO) approach. It means that the molecular electron wave functions  $\Phi$  are described as linear combinations of  $N$  atomic orbitals (AO)  $\phi_i$ , with  $\phi_i$  associated with the same atom being orthogonal:

$$\Phi = \sum_i a_i \phi_i . \quad (39)$$

One should note that the atomic wave functions are not orthogonal when centred at different atoms. Furthermore, a wave function  $\Phi$  constructed in this way is not necessarily an eigenfunction of  $H$ . This implies that a value  $E = \frac{\int \Phi H \Phi d\mathbf{r}}{\int \Phi^2 d\mathbf{r}}$  is not the corresponding eigenvalue of  $H$  applied to  $\Phi$ . The inequality (38) is valid nevertheless.

From eq. (37) and (39) we get

$$\epsilon(\{a_i\}, \{\phi_i\}) = \frac{\int (\sum_i a_i \phi_i) H (\sum_j a_j \phi_j) d\mathbf{r}}{\int (\sum_i a_i \phi_i) (\sum_j a_j \phi_j) d\mathbf{r}} = \frac{\sum_{ij} a_i a_j \int \phi_i H \phi_j d\mathbf{r}}{\sum_{ij} a_i a_j \int \phi_i \phi_j d\mathbf{r}} = \frac{\sum_{ij} a_i a_j H_{ij}}{\sum_{ij} a_i a_j S_{ij}} . \quad (40)$$

The integrals  $H_{ij} = \int \phi_i H \phi_j d\mathbf{r}$  are called resonance integrals. For  $i = j$  they give the energy of an electron which occupies the atomic orbital  $\phi_i$  in the surrounding molecule. The integrals  $S_{ij} = \int \phi_i \phi_j d\mathbf{r}$  are called overlap

integrals as they give the fraction of overlap of the atomic orbitals  $\phi_i$  and  $\phi_j$ .

It is a consequence of eq. (38) that of two wave functions the one with the lower energy is closer to the ground state wave function. Therefore we want to find a set of coefficients  $a_i$  for our basis set which minimises  $\epsilon$ . This requires that

$$\frac{\partial \epsilon}{\partial a_i} = 0 \quad \text{for } i = 1, \dots, N . \quad (41)$$

Performing the partial differentiations gives rise to a set of  $N$  equations which must be satisfied:

$$\sum_j a_j (H_{ij} - \epsilon S_{ij}) = 0 \quad \text{for } i = 1, \dots, N . \quad (42)$$

This set of equations only has a non-trivial solution if the determinant of the matrix  $H_{ij} - \epsilon S_{ij}$  is zero:

$$\begin{vmatrix} H_{11} - \epsilon S_{11} & \cdots & H_{1N} - \epsilon S_{1N} \\ \vdots & \ddots & \vdots \\ H_{N1} - \epsilon S_{N1} & \cdots & H_{NN} - \epsilon S_{NN} \end{vmatrix} = 0 . \quad (43)$$

Generally there are  $N$  energies  $\epsilon_\alpha$  which can be found from this secular equation with associated sets of coefficients  $a_j^{(\alpha)}$  that solve (42). These coefficients define one-electron wave functions within the chosen basis set:

$$\Phi_\alpha = \sum_{j=1}^N a_j^{(\alpha)} \phi_j \quad (44)$$

where the one associated with the lowest energy is the ground state and the other represent excited states.

#### 4.1.1 Hartree Fock

In order to solve a many-electron problem Hartree Fock theory introduces another approximation. The idea is that the system of interacting electrons is approximated by an effective one-particle problem, where an electron moves in the mean field of all other.

Many-electron wave functions, which have the correct symmetry<sup>5</sup> and take the principle of indistinguishability of quantum particles into account, can be constructed as Slater determinants from the one-electron eigenfunctions  $\Phi_\alpha$  associated with  $h_\alpha$ . In order to take spin into account as well, the spatial orbitals  $\Phi_\alpha$  are multiplied with spin-eigenfunctions  $\chi_\alpha(i, s)$ :

$$\Psi_{\text{SD}} = \frac{1}{\sqrt{n!}} \det [\Phi_\alpha(\mathbf{x}_i) \chi_\alpha(i, s)] \quad (45)$$

---

<sup>5</sup>Electrons have antisymmetric wave functions.

where  $n$  is the number of electrons and the notation  $\Phi_\alpha(\mathbf{x}_i)\chi_\alpha(i, s)$  denotes that electron  $i$  with spin  $s$  occupies the spin-orbital  $\chi_\alpha(i, s)$ .

Through variational calculus [44] it can be shown that in order to minimise  $\langle \Psi_{\text{SD}} | H | \Psi_{\text{SD}} \rangle$ , the  $\Phi_\alpha(\mathbf{x}_i)\chi_\alpha(i, s)$  each have to be eigenfunctions of their own one-electron Hamiltonian

$$h \Phi_\alpha(\mathbf{x}_i)\chi_\alpha(i, s) = \left[ -\frac{\hbar^2}{2m_e} \nabla^2 - \sum_k \frac{e^2 Z_k}{r_{ik}} + \int \rho(\mathbf{x}_j) \frac{e^2}{r_{ij}} d\mathbf{x}_j d\omega_j \right] \Phi_\alpha(\mathbf{x}_i)\chi_\alpha(i, s) - \int \rho(\mathbf{x}_i, \mathbf{x}_j) \frac{e^2}{r_{ij}} \Phi_\alpha(\mathbf{x}_j)\chi_\alpha(j, s) d\mathbf{x}_j d\omega_j = \epsilon_\alpha \Phi_\alpha(\mathbf{x}_i)\chi_\alpha(i, s) \quad (46)$$

where

$$\rho(\mathbf{x}_j) = \sum_{\beta}^n \Phi_\beta(\mathbf{x}_j)\chi_\beta(j, t)\Phi_\beta(\mathbf{x}_j)\chi_\beta(j, t) \quad (47)$$

is the electron density and

$$\rho(\mathbf{x}_i, \mathbf{x}_j) = \sum_{\beta}^n \Phi_\beta(\mathbf{x}_j)\chi_\beta(j, t)\Phi_\beta(\mathbf{x}_i)\chi_\beta(i, t) \quad (48)$$

is the density matrix.

In principle the eigenfunctions  $\Phi_\alpha$  can now be calculated from the secular equation (43). Hereafter only the special case of closed shell systems is discussed, i.e. every spin orbital is occupied by two electrons, which leads to the formalism of restricted Hartree Fock (RHF) theory. A consequence of this restriction is that it is not necessary to take spin into account directly, and therefore only spatial orbitals will be used. Furthermore we will now apply the LCAO approach and replace the one-electron wave functions  $\Phi$  with the basis functions  $\phi$  (see eq. (44)). In this case the resonance integrals are given by

$$\begin{aligned} \int \phi_s(\mathbf{x}_i) h \phi_t(\mathbf{x}_i) d\mathbf{x}_i &= \int \phi_s(\mathbf{x}_i) \left[ -\frac{\hbar^2}{2m_e} \nabla^2 - \sum_k \frac{e^2 Z_k}{r_{ik}} \right] \phi_t(\mathbf{x}_i) d\mathbf{x}_i \\ &+ \sum_{u,v} P_{u,v} \int \int \phi_s(\mathbf{x}_i) \phi_u(\mathbf{x}_j) \frac{e^2}{r_{ij}} \phi_v(\mathbf{x}_j) \phi_t(\mathbf{x}_i) d\mathbf{x}_j d\mathbf{x}_i \\ &- \frac{1}{2} \sum_{u,v} P_{u,v} \int \int \phi_s(\mathbf{x}_i) \phi_u(\mathbf{x}_j) \frac{e^2}{r_{ij}} \phi_v(\mathbf{x}_i) \phi_t(\mathbf{x}_j) d\mathbf{x}_j d\mathbf{x}_i \end{aligned} \quad (49)$$

where  $P_{u,v}$  is the density matrix in AO representation:

$$P_{u,v} = 2 \sum_{\alpha}^{\text{occupied}} a_u^{(\alpha)} a_v^{(\alpha)}. \quad (50)$$

The two double integrals are usually called two-electron or 'four index integrals' (as they involve four basis functions and two electrons). The first of those is the Coulomb integral, because it is directly equivalent to calculating the Coulomb interaction of two charge densities. The second four index integral is called exchange integral. In computational chemistry these are sometimes written as

$$\int \int \phi_a(\mathbf{x}_i)\phi_c(\mathbf{x}_j)\frac{e^2}{r_{ij}}\phi_d(\mathbf{x}_j)\phi_b(\mathbf{x}_i)d\mathbf{x}_j d\mathbf{x}_i = v_{ab,cd} \quad (51)$$

where the comma implies that wave function  $a$  and  $b$  are occupied by one electron and  $c$  and  $d$  by another.

The factor  $\frac{1}{2}$ , which precedes the exchange integral in eq. (49), is a consequence of explicitly calculating the integral over the spin eigenfunctions. As these are orthonormal the integrals  $\int \chi_\alpha(i, s)\chi_\beta(i, t)d\omega_i$ , which only occur in the last term of eq. (46) and (49), vanish if  $s \neq t$ . As there are two spin states for the electrons, with the same number of electrons occupying each of them, this results in a factor of  $\frac{1}{2}$ .

Another problem occurs in this prescription to obtain the resonance integrals. In order to calculate them one has to know  $P_{u,v}$ , and hence the wave functions, which shall in return be calculated from the secular equation. Hartree proposed a self-consistent method to solve this problem. One uses a guess for the wave functions  $\Phi_\alpha$  (respectively for the coefficients  $a_i^{(\alpha)}$  which determine  $\Phi_\alpha$ ) that allows for the calculation of the resonance integrals and consequently allows the calculation of a set of new  $a_i^{(\alpha)}$ . These can again be used to calculate new resonance integrals, where the  $\frac{n}{2}$  orbitals with the lowest energies are assumed to be occupied. This procedure is repeated until the  $a_i^{(\alpha)}$  do not change anymore (according to some arbitrary threshold value) and a self-consistent solution is found.

The energy of the molecular orbital is then calculated as

$$E = \sum_{\alpha=1}^n \epsilon_\alpha - \frac{1}{2} \sum_{a,b,c,d} P_{a,b}P_{c,d}(v_{ab,cd} - \frac{1}{2}v_{ad,bc}) \quad (52)$$

where  $\epsilon_\alpha$  is the corresponding eigenvalue to  $\Psi_\alpha$  and  $h_\alpha$  and the second term on the r.h.s compensates for the double-counting of the electron-electron interaction.

To summarise, the HF scheme is:

1. Choose a basis set and a molecular configuration (i.e. the coordinates of the nuclei).
2. Compute all overlap, one-electron, and two-electron integrals.
3. Guess an initial density matrix  $P_{u,v}^{(0)}$ .

4. Construct and solve the HF secular equation.
5. Compute the new density matrix  $P_{u,v}^{(n)}$ .
6. Compare  $P_{u,v}^{(n)}$  and  $P_{u,v}^{(n-1)}$ . If their differences are larger than a chosen threshold, return to step 4.
7. Compute HF energy.

In case of a geometry optimisation procedure, there is another loop around steps 2-7 for the optimisation of the positions of the nuclei.

### 4.1.2 PM3

PM3 is a semiempirical molecular orbital theory which makes several approximations to reduce the computational effort necessary to construct and solve the secular equation in the Hartree Fock scheme. It is based on the model of modified neglect of differential overlap (MNDO). To understand PM3 one should have a short look on the history of semiempirical molecular orbital theory. The goal always was to avoid the very demanding calculation of all the integrals which are the elements of the HF secular matrix. To this end a number of approximations were introduced. The most rigorous model is the so-called complete neglect of differential overlap (CNDO). It was developed by Pople, Santry and Segal in 1965. Their idea was to parametrise the matrix elements in the HF secular equation and thus to avoid the time consuming calculation of the involved integrals. They used the following conventions:

1. Every valence electron is represented by one Slater type orbital (STO) (see also subsection 4.1.4).
2. The overlap matrices are set to be delta functions (this is the reason for the name of the method)

$$S_{ij} = \delta_{ij} . \quad (53)$$

3. The two-electron integrals are set to be zero if they involve integrating over different basis functions occupied by the same electron. Otherwise they are each given a value  $\gamma_{IJ}$  which only depends on the types of the atoms  $I$  and  $J$  at which the two involved basis functions are centred:

$$v_{ab,cd} = v_{aa,cc} \delta_{ab} \delta_{cd} = \gamma_{IJ} . \quad (54)$$

4. For the two-electron one-centre integrals (i.e. the integrals over basis functions of two electrons which are centred at the same atom  $I$ ) the Pariser-Parr approximation is invoked:

$$\gamma_{II} = IP_I - EA_I \quad (55)$$

where  $IP_I$  is the ionisation potential of atom  $I$  and  $EA_I$  is its electron affinity.

5. The two-centre integral parameters  $\gamma_{IJ}$  are calculated from the one-centre integral parameters by

$$\gamma_{IJ} = \frac{\gamma_{II} + \gamma_{JJ}}{2 + r_{IJ}(\gamma_{II} + \gamma_{JJ})} . \quad (56)$$

This so-called Mataga-Nishimoto formalism has two intuitive limits. At short distances, it approaches the average of the one-centre values, while at large distances it approaches  $r_{IJ}^{-1}$  as expected for two charge clouds.

6. The one-electron integrals for diagonal matrix elements are calculated by

$$v_{ii} = -IP_i - \sum_k^{atoms} (Z_k - \delta_{Ik})\gamma_{Ik} \quad (57)$$

where  $IP_i$  is the energy needed to lift an electron occupying orbital  $i$  to the vacuum level and  $Z_k$  is the charge number of atom  $k$ .

7. The remaining off-diagonal one-electron integrals are calculated as

$$v_{ij} = \frac{(\beta_i + \beta_j)S_{ij}}{2} \quad (58)$$

where  $S_{ij}$  is explicitly calculated, and  $\beta_i$  and  $\beta_j$  are empirical parameters.

CNDO has a quite strong impact on the complexity of the original problem. The number of integrals is reduced from  $N^4$  to  $N^2$  and the remaining integrals are calculated by simple algebraic formulas. One can say that CNDO is the basis for most semiempirical methods that were developed later. In these the quality of the calculations was improved by relaxing the restrictions with respect to the remaining integrals.

An important development for modern semiempirical calculations was the introduction of the neglect of diatomic differential overlap (NDDO) method. The key change is made concerning the question which two-electron integrals to keep. In contrast to CNDO the integrals are kept for different basis functions of the same electron as long as those are centred on the same atom (the notation implies that basis function  $a$  is centred at atom  $A$ , basis function  $b$  at atom  $B$  and so on):

$$v_{ab,cd} = v_{ab,cd}\delta_{AB}\delta_{CD} . \quad (59)$$

The problem is somewhat less complex than it looks at first, as permutations of  $a$  and  $b$ , as well as  $c$  and  $d$  give the same value. Therefore one

has to deal with 100 integrals for every atom pair, if only s and p functions are used. Including d functions increases that number to 2025 which is still considerably less than in a full HF calculation.

Based on this formalism Dewar and Thiel reported a method for the elements C, H, N, and O in 1977 which they called modified neglect of differential overlap (MNDO). Instead of calculating the necessary integrals directly, they replaced the continuous charge clouds given by the electron wave functions with classical multipoles. Through that trick, the evaluation of the integrals and the determination of their analytic derivatives with respect to nuclear motion is made quite easy. The nuclear repulsion energy is calculated as

$$V_N = \sum_{\substack{\text{nuclei} \\ k < l}} Z_k Z_l v_{s_k s_k, s_l s_l} (1 + \tau e^{-\alpha_k r_{kl}} + e^{-\alpha_l r_{kl}}) \quad (60)$$

where  $\alpha$  is an atom type specific parameter and  $\tau = r_{kl}$  for O/H or N/H pairs, and  $\tau = 1$  in every other case. The double indices  $s_k$  and  $s_l$  imply that the two-electron two-centre integrals over the s orbitals on each atom are used.

In 1985 Dewar and his co-workers reported a modified functional form for the nuclear repulsion:

$$V_N(A, B) = V_{AB}^{MNDO} + \frac{Z_A Z_B}{r_{AB}} \sum_{i=1}^4 (a_{A,i} e^{-b_{A,i}(r_{AB}-c_{A,i})^2} + a_{B,i} e^{-b_{B,i}(r_{AB}-c_{B,i})^2}). \quad (61)$$

Initially they only optimised parameters for the elements C, H, O, and N and called that new model AM1 (Austin Model 1). Later parametrisations for B, F, Mg, Al, Si, P, S, Cl, Zn, Ge, Br, Sn, I and Hg were reported.

J. Stewart, one of the co-workers of Dewar, was not satisfied with the parameter optimisation method used in AM1. On the one hand the parameters had been optimised in a step-wise fashion, on the other hand a lot of human intervention had occurred. Additionally, the scanned parameter space was smaller than might have been desirable. Stewart felt that it would be better to optimise all parameters simultaneously. The result of his work for the atoms H, C, N, O, F, Al, Si, P, S, Cl, Br and I was the PM3 model (parametrisation model 3, the third model of its kind after MNDO and AM1). Later parameters for Li, Be, Na, Mg, Ca, Zn, Ga, Ge, As, Se, Cd, In, Sn, Sb, Te, Hg, Tl, Pb, and Bi were reported, too.

While AM1 is already doing much better than an MNDO calculation, PM3 was found to outperform AM1 slightly for lighter atoms and by a larger margin for calculations involving heavier atoms. Both AM1 and PM3 are still commonly used in today's research, and many molecular modelling packages include these methods. While the results for energies and geometries for systems close to the training sets used for the parameter optimisation are satisfying, one has to be careful with systems which are less

similar to these training sets. For that reason even unphysical behaviour can be observed sometimes, when applying PM3 or AM1 calculations to new molecular systems.

Unfortunately, this might apply for the glassy systems studied in this work. As AM1 does not include parameters for lithium atoms, PM3 was used. The motivation to use such a semiempirical method at all is the fact that our initial guesses for a structure are typically far away from a relaxed configuration. This makes the geometry optimisation of these atomic configurations rather time consuming. Our hope is that by using the very fast PM3 calculations, the structure can be preoptimised and the most unrealistic configurations are already eliminated before starting the much more computational demanding HF and DFT calculations.

### 4.1.3 Density functional theory

The basic idea behind density functional theory is that instead of using the wave functions to predict properties of a system one could use the electron density. Hohenberg and Kohn showed that the ground state electron density defines the ground state energy of a system or in other words that the energy is a functional of the density:  $E[\rho(\mathbf{x})]$ . This is known as the Hohenberg-Kohn existence theorem. An alternative formulation is that there exists a one to one mapping from the ground state electron density to the ground state wave function of a system.

The second Hohenberg-Kohn theorem is equivalent to the variational principle (38) of molecular orbital theory:

$$E[\rho(\mathbf{x}) \neq \rho_0] \geq E_0 . \quad (62)$$

However these two theorems do not provide a way of how to go about calculating the energy of a system. The crucial breakthrough came from Kohn and Sham in 1965. The idea is that one evaluates the energy functional of a fictitious system of non-interacting electrons which has the same ground state density as the real system of interest (note the similarity to the idea behind HF theory where the many-particle problem is approximated by an effective one-particle problem):

$$E[\rho(\mathbf{r})] = T_{\text{ni}}[\rho(\mathbf{r})] + V_{\text{ne}}[\rho(\mathbf{r})] + V_{\text{ee}}[\rho(\mathbf{r})] + \Delta T[\rho(\mathbf{r})] + \Delta V_{\text{ee}}[\rho(\mathbf{r})] . \quad (63)$$

The five terms on the r.h.s. are the kinetic energy of the non-interacting electron system, the nuclear-electron interaction, the classical electron-electron repulsion, the correction to the kinetic energy due to the interacting nature of the electrons and all non-classical corrections to the electron-electron repulsion. The last two terms are usually merged together into the so-called exchange correlation functional  $E_{\text{xc}}[\rho(\mathbf{r})]$ . One should note that this energy functional is still exact. Furthermore, the density is expressed through

orbital wave functions  $\rho = \sum \langle \chi_i | \chi_i \rangle$ . The corresponding Hamiltonian is

$$\sum_i h_i^{KS} = \sum_i \left( -\frac{\hbar^2}{2m_e} \nabla_i^2 - \sum_k^{nuclei} \frac{eZ_k}{|\mathbf{r}_i - \mathbf{r}_k|} + \int \frac{\rho(\mathbf{r}')}{|\mathbf{r}_i - \mathbf{r}'|} d\mathbf{r}' + V_{xc} \right) \quad (64)$$

with  $V_{xc} = \partial E_{xc} / \partial \rho$ . One can calculate the eigenfunctions of this Hamiltonian in exactly the same way as it was done in Hartree Fock theory.

So far DFT contains no approximations, but the problem with treating the complicated interelectronic correlations is only moved, not solved. The difficult question is how the exchange correlation functional looks like. The problem is that it is not possible to determine an exact functional and therefore the involved equations can only be solved approximately.

Usually one adopts a form

$$E_{xc}[\rho(\mathbf{r})] = \int \rho(\mathbf{r}) \epsilon_{xc}[\rho(\mathbf{r})] d\mathbf{r} \quad (65)$$

for the exchange correlation functional where  $\epsilon_{xc}$  is the energy density which is mostly treated as a sum of an exchange part  $\epsilon_x$  and a correlation part  $\epsilon_c$ . Spin can be included by using two electron densities for the different spins, and expressing the functionals in terms of those. Even in the most simple case the terms developed for the exchange and the correlation energy density are complicated so that we do not discuss them in detail some general properties are of interest.

The first approach to find an expression for  $\epsilon_x$  and  $\epsilon_c$  is the so-called Local Density Approximation (LDA). This means that the energy functionals at position  $\mathbf{r}$  are not depending on the functional form of the electron density but only on its local value at this position. The corresponding methods taking into account spin are called Local Spin Density Approximation (LSDA). The functional forms usually make use of a number of empirical constants which are derived from fitting routines. While this makes DFT in essence a semiempirical method, the number of empirically determined constants is usually far less than that for semiempirical molecular orbital theories.

An obvious improvement of LDA functionals is to include a dependence on the (local) value of the gradient of  $\rho(\mathbf{r})$ . This defines the generalised gradient approximation (GGA). In table 6 common functional abbreviations are listed (mostly named after the authors and the year of publication). Most of the GGA functionals just add a correction to the LDA terms for the exchange energy and the correlation energy. One often used exception is LYP which gives a total new term for the correlation energy density.

When referring to a DFT method, a combination of the abbreviations for the exchange and the correlation term are used: e.g. PWLYP for the combination of an exchange energy functional published by Perdew and Wang and a correlation energy functional developed by Lee, Yang, and Parr.

Table 6: Common GGA-functionals

$\epsilon_x$	B, CAM, FT97, O, PW, <i>m</i> PW, X, B86, PBE
$\epsilon_c$	B88, P86, PW91, LYP

The most often used DFT method is neither a GGA nor a LSDA form. B3LYP is a so-called hybrid functional which mixes a GGA functional with the Hartree Fock exchange term:

$$E_{xc}^{\text{B3LYP}} = (1 - a)E_x^{\text{LSDA}} + aE_x^{\text{HF}} + bE_x^{\text{B}} + (1 - c)E_c^{\text{LSDA}} + cE_c^{\text{LYP}} \quad (66)$$

where a,b, and c are three empirical parameters. The merit of such hybrid functionals (of which the B3LYP is the most widely used due to its superior quality/computational effort ratio) is that the systematic errors from Hartree Fock and DFT due to exchange and correlation effects are typically of opposite sign and can cancel each other to some extent. For instance barrier heights in chemical reactions are often overestimated by Hartree Fock calculations and underestimated by GGA-DFT methods.

Typically, the performance of B3LYP and HF calculations is rather similar for the prediction of molecular geometries (given a reasonably sized basis set). For energies and vibrational properties this is different. Here B3LYP calculations usually provide the better results (errors of calculated energies are typically an order of magnitude smaller). As the B3LYP calculations take more time and SCF convergence is often more problematic than in an HF calculation, the latter will be used for the main geometry optimisation, while B3LYP DFT calculations are performed in order to compute Raman and IR spectra. It is nevertheless necessary to optimise the HF structures again using the DFT calculations, as the atomic configuration must be in an energetic minimum with respect to the theory applied to the computation of the spectra.

#### 4.1.4 Basis sets

As the computational effort as well as the precision of molecular orbital theory calculations depend on the number of basis functions to a great extent, considerable work has been undertaken to find optimal basis sets. Most of them apply basis functions which are centred at the nuclei. One class of such basis functions are the so-called Slater type orbitals (STO) which are based on the exactly known hydrogen orbitals. They have the correct exponential decay with distance  $r$  from the nucleus, the 1s orbital has a cusp at  $r = 0$ , and the angular component is the same as in the hydrogen atoms:

$$\phi_{\text{STO}}^{(\eta,n,l,m)} = Cr^{n-1}e^{-\eta r}Y_l^m(\theta, \varphi), \quad (67)$$

where  $n$ ,  $l$ ,  $m$  are the usual quantum numbers,  $\eta$  is a atom type specific parameter, and  $C$  is a normalisation constant. If exactly one STO is used for every atom orbital up to the period of the atom, one speaks of a minimal basis set.

While STOs are a good intuitive choice to represent AOs, for computational reasons Gaussian basis functions (GTO) are mainly used. The merit of Gaussian functions is the existence of analytical solutions for the general four-index integrals  $v_{ab,cd}$  which do not exist for STOs. A drawback are their bad physical properties, as for example the exponential decay with  $r^2$  instead of  $r$ . In order to combine the best properties of STOs and GTOs, Gaussian basis sets were developed where a linear combination of several Gaussian functions (referred to as contracted Gaussian) is used to mimic one STO. Such basis sets were developed by Hehre, Stewart, and Pople in 1969. They called them STO-MG, for 'Slater-type orbitals approximated by  $M$  Gaussians':

$$\phi_{\text{STO-MG}}(\alpha_a, i, j, k) = \sum_{a=1}^M c_a x^i y^j z^k e^{-\alpha(x^2+y^2+z^2)}, \quad (68)$$

where  $i$ ,  $j$ , and  $k$  are positive integer numbers which determine what type of orbital the STO-MG is ( $i + j + k = l$ , with  $l$  being the usual quantum number). The coefficients  $c_a$  are optimised to mimic the STO which is equivalent to the choice of  $i$ ,  $j$ , and  $k$ .

In order to increase the flexibility of a basis set, one can decontract the STO-MG basis functions again. While the number of primitive Gaussian functions is not increased, the secular equation becomes more complex, as more individual basis functions are used. Usually not all basis functions are decontracted but only those which represent valence orbitals. The most widely used so-called 'split-valence' basis sets are those of Pople *et al.*. An example is the 6-31G basis set. The nomenclature means that each core orbital is represented by a single basis function consisting of 6 contracted primitive Gaussian functions, while each valence orbital is represented by two basis functions with a total of 4 primitive Gaussians of which 3 are contracted.

In order to achieve even more flexibility, polarisation functions can be added. In basis sets of Pople *et al.* d orbitals are added for second row and third row atoms (indicated by one star '\*') and p orbitals for H and He (indicated by a second star '\*\*'). This is especially necessary for system including atoms in formally hypervalent bonding situations, e.g. sulfoxides and siliconates. For more details regarding computational aspects and the used methods see [45].

## 4.2 Simulating 'glass' cluster

The number of available works regarding ab initio calculations of glass systems is rather limited. As in the case of the MD-simulations silicate systems were investigated in most of these works. The earliest ab initio calculations were motivated by the search for effective force fields for MD-simulations, e.g. that of Tsuneyuki *et al.* in 1988 in order to determine potential parameters for a silica glass (already mentioned in section 2.1.1). Only a single  $\text{SiO}_4$  tetrahedron was simulated. In the mid of the next decade first HF calculations of larger clusters involving 15-30 atoms (not counting saturating hydrogen atoms) appeared. T. Uchino and T. Yoko for example presented results of HF calculations of small borate and sodium borate clusters (one of the very few works which exist at all for alkali glasses) using the basis sets 3-21G\* and 6-31G\*. They calculated structural properties, as bond lengths and bond angles, as well as some selected vibrational bands [46, 47].

Until recently, only the number of atoms has been increased slightly. Now also DFT calculations are performed. R. Ginhoven *et al.* for example performed DFT molecular dynamics of a silicate glass. They used periodic systems of 72 atoms which were first equilibrated by classical MD-simulations using the BKS potential before being simulated for a few ps using DFT methods. They showed that it is possible to achieve similar distributions of bond lengths and bond angles by averaging over several small samples (using DFT), as are found in MD-simulations of large systems and in neutron scattering experiments [48]. In 2006 J. Du and L.R. Corrales (who also was co-author of the paper of Ginhoven) published results for similar simulations of lithium disilicate. In addition to structural properties they also reported that the dynamics of the lithium ions were decoupled from that of the SiO network during their DFT-MD-simulations [49].

The development of effective force fields for MD-simulations was topic of some recent works as well. J. Mauro and A. Varshneya for example determined an MD potential for  $\text{GeSe}_2$  from ab initio calculations of a single tetrahedron. While the size of the system is as small as that of the first ab initio calculations concerning glasses, they used fourth-order Møller-Plesset perturbation theory (MP4) and the aug-cc-pVQZ basis set which is several orders of magnitude more demanding in terms of computational resources than the simple HF calculations performed 20 years earlier [50].

## 4.3 Creating glass cluster start configurations

As the used molecular orbital theories are zero temperature methods, a geometry optimisation with respect to the energy of a given atomic configuration leads to the next minimum in the PES. Furthermore, a geometry optimisation is a rather time consuming procedure. Therefore it is necessary to use structures as input for the electronic structure calculations which

are already close to a relaxed configuration. Three approaches seem to be promising:

1. using known structures
2. making an educated guess
3. taking input data from other simulations like MD or RMC (Reverse Monte Carlo).

Obviously, 'using known structures' is only possible if detailed information is available about the atomic structure of a material. This information can come from different sources. Often a concept of the material structure can be derived from spectroscopic and diffraction data by using group theory and the involved symmetry principles. This approach works rather well for molecules with high symmetry or crystals, but unfortunately it does not work for amorphous materials like glasses. Nevertheless there have been several suggestions for medium range order structures as, for example, the possible existence of boroxol rings in borates. Such structures can be checked for their spectral fingerprint with electronic structure calculations.

The second approach is to guess a reasonable start configuration. All  $\text{Li}_2\text{SO}_4$  clusters are produced this way and most of the borate clusters up to a size of about 60 atoms. We make the assumption that the lithium sulfate salt glass consists of intact  $\text{SO}_4$  units with lithium ions in the areas in between. Using the GaussView3.0 [51] program  $\text{SO}_4$  tetrahedra are constructed with random orientation in space. Lithium ions are added, taking minimal distances of 1.6 Å into account. The  $\text{Li}_2\text{SO}_4$  clusters constructed that way have sizes between 7 (one unit) and 56 (8 units) atoms.

In case of the borate cluster our basic assumption is that the glass network is formed by trigonal  $\text{BO}_3$  and tetrahedral  $\text{BO}_4$  units with two neighbouring units sharing a common oxygen. Using this principle clusters with up to 7 boron ions are built. The appropriate number of lithium ions is incorporated into the cluster, taking minimal interatomic distances of 1.6 Å into account. For all clusters a nominal stoichiometry of metaborate ( $\text{Li}_2\text{O}-\text{B}_2\text{O}_3$ ) is taken as target composition. Due to the surface of the cluster, and the associated truncation of the network, the number of oxygen atoms exceeds the nominal number. An additional problem caused by the truncation is the fact that a priori all oxygens on the surface of a cluster are non-bridging ones (for clusters up to 60 atoms this is more than 50%).

To reduce the impact of these problems we use two saturation schemes. The first one is to use hydrogen atoms to saturate truncations of the network. The idea is to add positive counter charges to take into account the effect of the surrounding network. The second approach is to give the cluster a negative net charge according to the approximated number of missing bonds. An advantage of the hydrogen saturation is that one can decide

where the network is virtually continued. A disadvantage is the introduction of additional atoms (and thereby computational complexity) and a number of new vibrational modes. Fortunately, these typically have considerably higher frequencies than the real metaborate vibrations. By using a net charge instead, these additional vibrations can be avoided. But such a charge can be distributed in any way over the whole cluster. One cannot decide how this is done, as it is a result of the SCF calculations. For most of the metaborate clusters up to the size of 60 atoms we used both schemes to compare the influence.

A third approach is to use input structures taken from other types of simulations. The idea behind this scheme is that other types of simulations might provide already reasonably good structures, so that a geometry optimisation using ab initio methods can successfully converge into a realistic structure. As the construction of glass networks by hand is getting much more difficult with increasing size of a cluster, we use this method to get start configurations for the large borate clusters. They are taken from MD-simulations based on an effective potential of A. H. Verhoef and H. W. den Hartog [25] which was later modified by Kamitsos *et al.* [15]. While this potential is not suitable for the simulation of atom dynamics on time scales much larger than the time of molecular vibrations, there are good indications that it is doing reasonably well in predicting structures for lithium borate systems. For example the fraction of non bridging oxygens, as well as the fraction of triangular and tetrahedral coordinated boron atoms are in agreement with experimental data. Furthermore, the near infrared spectrum could be reproduced, indicating that the coordination shell of lithium atoms is reasonable.

One goal of this work is to check the influence of nitrogen on the structure of LISON films, modified  $\text{Li}_2\text{SO}_4$  clusters are produced later. These are based on pure lithium sulfate clusters, by taking geometry optimised configurations (on a HF/6-31G\* level) and by replacing oxygen atoms with nitrogen. In clusters of 28 atoms two oxygen ions are replaced, in clusters of 56 atoms four oxygen ions.

A full list of the produced configurations and which method has been used can be found in the appendix.

#### 4.4 Calculation procedure

The semi-empirical, HF, and DFT calculations are performed using the Gaussian 03 suite of quantum chemistry programs [52].

The first stage of the computations is a PM3 and in case of the borate clusters and additional HF/3-21G geometry optimisation run. Starting with the resulting clusters, a HF calculation is performed for further geometry optimisation and a subsequent computation of the vibrational spectra. The basis set for this step is 6-31G\*.

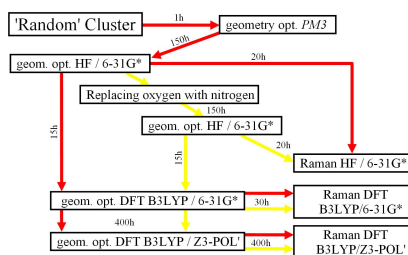


Figure 18: Schematic representation of the calculation procedure for the LISON clusters.

In order to monitor the influence of nitrogen in the case of the LISON films, modified  $\text{Li}_2\text{SO}_4$  clusters were generated by replacing oxygen atoms by nitrogen atoms in the optimised  $\text{Li}_2\text{SO}_4$  cluster configurations. Following another geometry optimisation at a Hartree Fock 6-31G\* level of theory, the vibrational spectra of these nitrogen containing clusters are calculated.

Taking the HF 6-31G\* geometries as starting points, DFT calculations are performed, using the B3LYP functional of Stevens *et al.* with the 6-31G\* basis set. Following a mandatory geometry optimisation the Raman spectra for the different systems are calculated.

Some selected LISON systems have been used for calculations with the much larger Z3POL basis set. The Z3POL basis set of Benkova *et al.* has been shown to allow very accurate Raman spectra calculations, both in terms of frequencies and intensities. As lithium is not defined within this basis set, we extend it by using the 6-311+G\* basis for this type of atom. We will refer to this modified basis set as Z3POL'. Figure 18 summarises the procedure in a schematic way for the more complex LISON calculations.

While the PM3 level calculations take only a relatively short time (approximately one hour for a cluster containing 28 atoms) the time needed for the higher level methods increases drastically. The HF calculations take up to 200 cpuh for the smallest clusters and exceed 5000 cpuh for the largest clusters<sup>1</sup>. Unfortunately the required new geometry optimisation after replacing some oxygen atoms by nitrogen in the lithium sulfate clusters can take equally long. On the other hand, the geometries found by HF theory seem to be reasonably good, as the successive optimisation using density

<sup>1</sup>The calculation time roughly scales with  $N^3$  where  $N$  is the number of atoms.

functional theory takes only a few iterations. The additional time for a B3LYP/6-31G\* calculation is about 50 cpuh for the small clusters. However, it does increase dramatically for the Z3POL' basis set. In table 10 in the appendix the total times of the different runs as well as the number of geometry optimisation iterations are listed. The number of iterations is mostly determined by the quality of the initial guess for the structure, while the conversion factor from iteration steps to run time depends mainly on the used theory, the basis set and the size of the system.

Several problems occurred during the calculations. While some of these problems are linked to intrinsic limitations of the used theories, others are directly linked to the properties of a glass.

One of the main problems in treating amorphous materials with ab initio calculations is the lack of a unique structure. The potential energy surface (PES) of a glass has numerous local minima, and only few of them are linked to structures that exist in the real material. When performing calculations on such glass systems, one faces the problem that most initial guesses of a structure will lead into one of the minimas of the PES in the course of the geometry optimisation. Filtering out the ones whose associated clusters are good representatives of the local structures of the LISON film or the lithium borate glass, is a task which either relies on knowledge of the system obtained from measurements of the real material or involves some sort of statistics, e.g. assuming that in the real glass the probability of finding a given local structure obtained from the calculations is given by its Boltzman factor  $p \sim \exp(-\frac{E}{k_b T})$ .

Unfortunately, the latter approach is not applicable to every system. It is not only the energy of a minimum which determines whether it is of relevance for the glass structure, but kinetic processes during the glass formation can prevent the system from reaching the energetically most favourable configuration (otherwise the system would crystallise).

Another major problem is the limited size of the clusters, restraining us to a situation where almost every atom lies on the surface. In fact, when using only four SO<sub>4</sub> groups, these even tend to arrange in a plane. That problem can hardly be avoided, as bulk-type clusters with negligible influence of the surface would be too large to be handable with the accessible resources.

Regarding the replacement of oxygen by nitrogen in the LISON clusters one has to take the uneven numbers of electrons of the nitrogen atoms into account, too. Therefore, an even number of nitrogen atoms has to be introduced, since the geometry optimisation of open shell systems (uneven number of total electrons) can often be very unreliable in HF calculations.

The analysis of Raman spectra obtained from these calculations has to be done with care as well. To obtain a smooth spectrum from the calculated Raman lines, each line  $j$  with Raman shift  $\omega_j$  and intensity  $I_j$  is replaced by a Gaussian peak function  $I_j \exp[-(\omega - \omega_j)^2/\Delta^2]$  with  $\Delta = 20 \text{ cm}^{-1}$ . In

addition, a rescaling of the calculated Raman shifts is generally necessary to obtain good agreement with the experimental spectra, depending on the particular material and method used. This is often accounted for by stretching the whole spectra by a factor of about 0.9 in case of HF calculations. For DFT calculations an optimal factor of 0.98 has been reported. These factors have been determined by adjusting a test set of about 1000 well defined calculated vibrational modes derived from several small gas molecules as well as a number of organic molecules with experimental data. As this test set did not contain any systems similar to the one of interest in this investigation, it is not clear whether these factors are a good choice here too. In fact, factors larger than 1.0 have been used to compare DFT spectra with experimental data in some studies [53]. Moreover, the calculated intensities cannot easily be compared with the experimental ones. On one hand the absolute Raman intensities were not determined during the experiments on the thin film glasses. On the other hand intensities from HF theory are known to be unreliable. Intensities obtained from DFT calculations are usually in better agreement with experiments.

It should be noted that the typical technical problems such as a non-converging SCF calculations or geometry optimisation runs (which end up cycling periodically between some configurations) occurred as well. In particular the approaches followed to take condensed phase effects into account by adding a solvent were not successful.

## 4.5 Comparison of methods

In order to check the general influence of the different calculation methods on the spectra, test-calculations with a single  $\text{Li}_2\text{SO}_4$  unit have been performed. The calculation procedure described earlier has been followed for an isolated molecule and for a molecule in a solvent environment. Figure 19 shows the corresponding (scaled) spectra. The most notable difference between the various methods and basis sets are the necessary scaling factors to align the  $\text{SO}_4$  symmetric breathing mode at  $1014\text{ cm}^{-1}$ . While the factors of 0.97 for the Hartree Fock 6-31G\* calculation and 1.09 for the DFT-B3LYP 6-31G\* calculation are still within a reasonable range of values suggested in literature, the factor for the DFT-B3LYP Z3POL' is surprisingly large with 1.34. This behaviour finds its equivalent in the geometries. While the oxygen-lithium distance does not change ( $1.86\text{ \AA}$ ) the oxygen-sulphur distance increases from  $1.48\text{ \AA}$  to  $1.52\text{ \AA}$  to  $1.60\text{ \AA}$  with the different methods. All scaling factors are slightly reduced when performing calculations using a self-consistent reaction field SCRf algorithm to simulate condensed phases influences (solvent THF, method IEFPCM<sup>6</sup>). Again this corresponds to a

---

<sup>6</sup>IEFPCM stands for integral equation formalism polarised continuum model and THF for Tetrahydrofuran which has a similar permittivity as lithium sulfate. For more details on the methods please see [45].

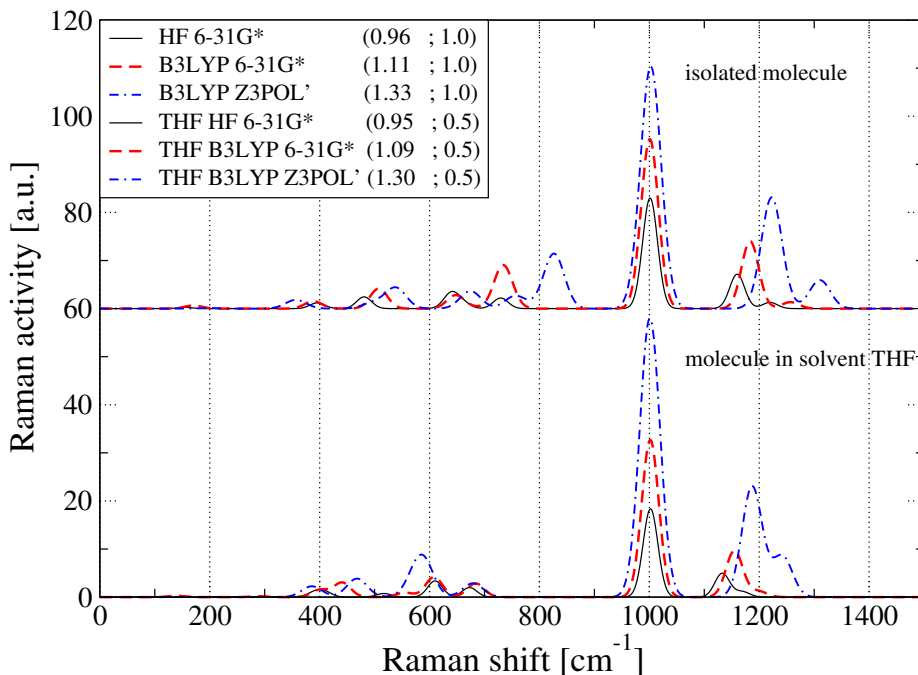


Figure 19: A comparison of Raman spectra of a single  $\text{Li}_2\text{SO}_4$  unit calculated with various methods. The two numbers give the scaling factor for the frequencies and the intensity. The spectra were scaled so that the  $\text{SO}_4$  symmetric breathing mode is aligned to  $1014 \text{ cm}^{-1}$ .

slightly decreased oxygen-sulphur distance. On the other hand, the lithium-oxygen distance increases dramatically in the presence of the solvent (from  $1.86 \text{ \AA}$  to  $2.00 \text{ \AA}$ ). This might be the reason for the failure of the geometry optimisation runs of larger clusters when including a solvent. For this reason (and the increased computational time needed) no further calculations with a solvent were done. Furthermore, with an increasing level of theory (HF 6-31G\* / DFT-B3LYP 6-31G\* / DFT-B3LYP Z3POL') the bands are generally shifted to higher energies (except the main band as that one was scaled to lie at  $1014 \text{ cm}^{-1}$ ).

#### 4.6 Evaluation of clusters by comparing vibrational spectra

As discussed above, one can expect many clusters to be bad representations of local structures of the real glass systems since they represent local minima of the PES which are not realised in reality. The question arises how one can select the correct ones. A promising approach is the comparison of vibrational spectra (Raman and infrared). Such spectra can be measured for almost every system. Additionally the Raman and infrared modes are mainly determined by the short and medium range order of a material which

is exactly what one can model with ab initio calculations (an exception are those low energy bands which have their origins in collective vibrations of a large number of atoms).

When comparing the calculated spectra with the measured ones, one has to bear the following in mind:

1. The measured Raman spectra for lithium sulfate are of rather poor quality, while the infrared spectra are dominated by the signal of the silicate substrate and influences from the film geometry.
2. Ab initio methods have systematic errors connected to the approximations made. Therefore the predicted frequencies are usually all too high or all too low. This is often accounted for by stretching the whole spectra by a factor (around 0.9 for HF and 0.98 for DFT/B3LYP).
3. The calculated relative Raman activities and infrared intensities from HF theory are often of bad quality.

#### 4.6.1 $\text{Li}_2\text{SO}_4$

Six initial lithium sulfate clusters converged successfully on all levels of theory. They consist of one, four and eight  $\text{Li}_2\text{SO}_4$  units. All Raman spectra show qualitatively the same features. The most dominant band lies between  $900\text{ cm}^{-1}$  and  $920\text{ cm}^{-1}$  where the frequency tends to increase with growing cluster size. This band can be associated with the  $\text{SO}_4$  symmetric breathing mode. While a number of further modes can be found with less intensity below  $700\text{ cm}^{-1}$  and between  $1000\text{ cm}^{-1}$  and  $1300\text{ cm}^{-1}$ , it is a characteristic of all spectra that there is an intensity gap between  $700\text{ cm}^{-1}$  and  $850\text{ cm}^{-1}$ .

Comparing these spectra with the experimental one, one can see that, while the qualitative structure of the calculated spectra is quite correct, the main bands are shifted to lower energies. This is obvious, too, when taking the crystal Raman modes of lithium sulfate into account. The symmetric breathing mode of the  $\text{SO}_4$  tetrahedra of the crystal is found at  $1014\text{ cm}^{-1}$ . One should expect to find it nearby in the glass as well. Therefore we rescale the energies of all calculated vibrational modes. The calculated  $\text{SO}_4$  breathing mode frequencies differ slightly from each other due to the different local surroundings of the  $\text{SO}_4^{2-}$  anions in the clusters. Taking the average of them and determining the quotient with the corresponding crystal mode frequency gives a stretching factor of 1.11. Using this factor yields theoretical spectra which appear to be shifted to higher frequencies. An optimal overlap of calculated and measured spectra is obtained with a slightly reduced factor of 1.09. This minor correction should not be surprising as some shift of the breathing mode frequency can be expected when considering the crystal and the film. To summarise, for the comparison all calculated spectra are stretched by this factor of 1.09. After rescaling, the spectra of the large

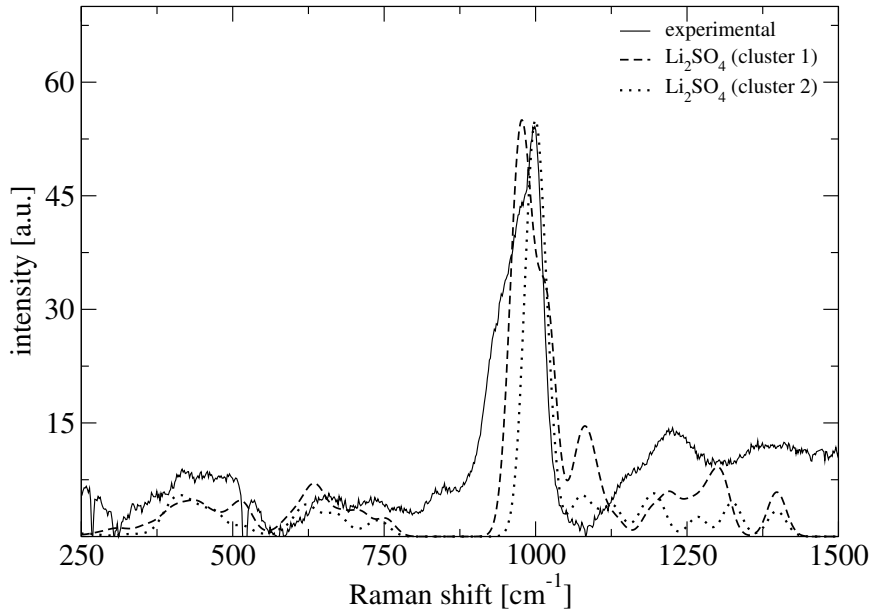


Figure 20: Comparison of two calculated Raman spectra for  $\text{Li}_2\text{SO}_4$  clusters with the experimental Raman data.

clusters resemble the measured spectrum quite well. Even the smallest ones are not too bad, except for a larger difference in intensity. One should note that a scaling factor of 1.09 is rather large and actually way off from numbers suggested in literature. On the other hand these numbers have been determined by comparing spectra for several small gas and organic molecules. These systems are rather far away from the inorganic glasses which are the subject of this work. So it is not to much of a surprise that different values are necessary here.

Two main differences between the measured and calculated Raman spectra can be seen in figure 20.

1. The measured spectrum shows a broad shoulder to lower energies from the main band at  $1002\text{ cm}^{-1}$ . This shoulder is absent in the calculated spectra.
2. In the experimental spectrum there is no band at  $1080\text{ cm}^{-1}$ , but still the large clusters have a Raman mode at that position.

The first difference might be due to the missing nitrogen. One should remember that the measured thin film is not a pure lithium sulfate system, but it contains a lot of nitrogen. A second influence probably comes from surface effects due to the limited size of the clusters.

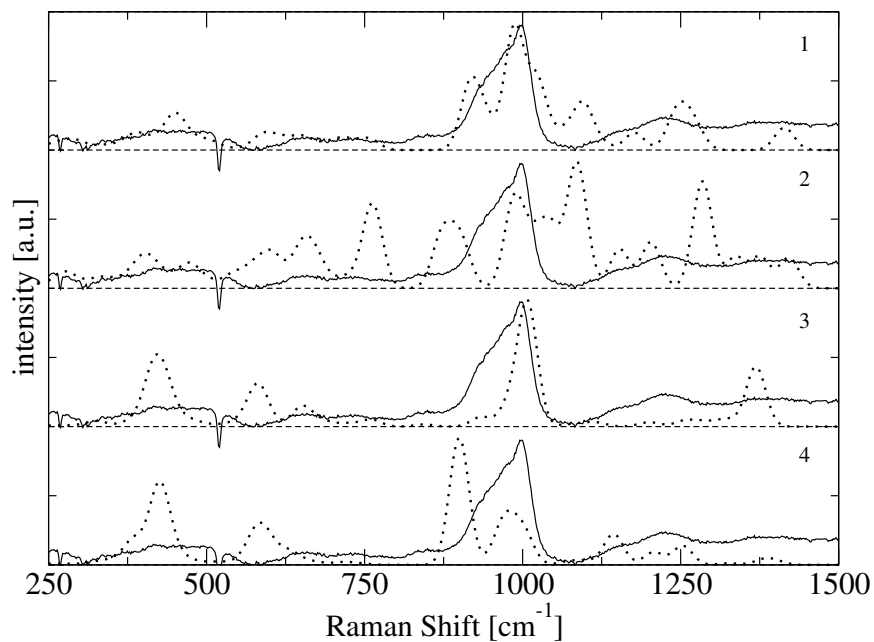


Figure 21: Comparison of four calculated Raman spectra (dotted lines) for LISON clusters with the experimental Raman data (solid lines).

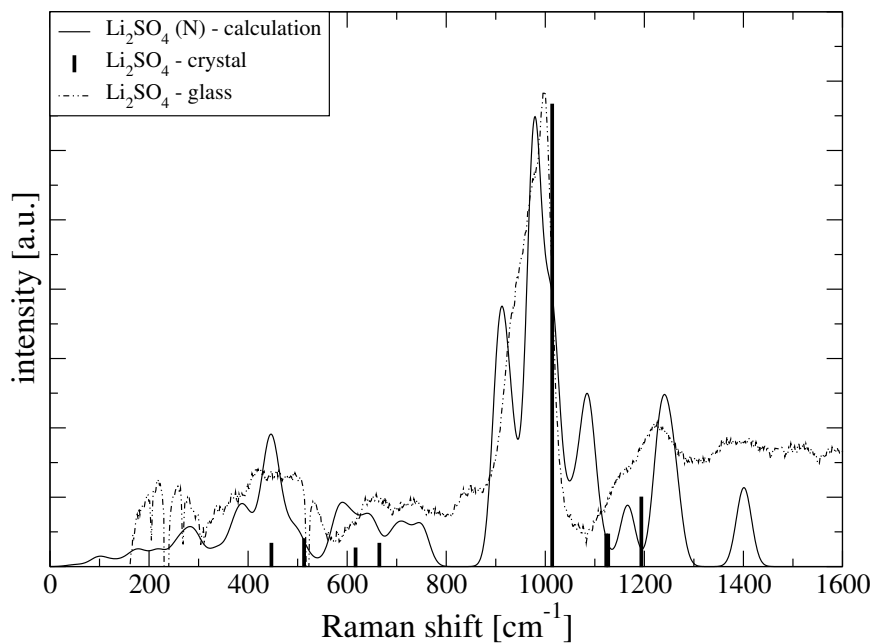


Figure 22: Raman spectrum of the LISON cluster with the best agreement of experimental and calculated spectrum. The crystal data is taken from [43].

### 4.6.2 LISON

Ten configurations with nitrogen atoms replacing oxygens are calculated. In the clusters with 28 and 56 atoms two and four oxygens, respectively, are replaced. In the small clusters with only 7 atoms one oxygen atom is replaced. The introduction of nitrogen into the system has a very strong influence on the spectra. This is not very surprising as at least half of the  $\text{SO}_4^{2-}$  anions are replaced by  $\text{SO}_3\text{N}^{2-}$ . This rather large amount of nitrogen is nevertheless in agreement with results from Rutherford backscattering experiments which showed for these films a ratio of about 2 : 1 for sulphur to nitrogen [54]. Numerous new bands appear in the Raman spectra. But while the clusters without nitrogen lead to very similar Raman spectra, the modified systems show a less homogeneous behaviour.

The spectra of the clusters shown in figure 21 are very different, and most of them compare poorly with the experimental data (not all calculated spectra are shown here, but these four are representative). The ones which fit best are actually the clusters with the lowest overall energy for their size. This suggests that the structures of these particular clusters are in good agreement with local structures found in the real material.

In fig. 22 the cluster with the best agreement of experimental and calculated spectrum is shown. In addition the crystal Raman lines, which were already used for the comparison of the measured Raman spectrum in sec. 3.3, are shown. Taking a closer look at this spectrum, we see that one of the main differences in the spectra of the calculated lithium sulfate clusters without nitrogen and the measured spectrum is explained. Below the Raman bands associated with the  $\text{SO}_4$  symmetric breathing mode additional bands are found due to the nitrogen. Those explain the broad shoulder observed in the Raman measurements.

### 4.6.3 $\text{Li}_2\text{O-B}_2\text{O}_3$

As in the case of the calculated Raman LISON spectra the IR spectra of the various lithium borate clusters are rather different, too (see figure 23). Again most of them do not compare well with the experimental data which was measured by E.I. Kamtisos *et al.* on bulk material [55]. To get an optimal overlap of the calculated spectra with the experimental one, it was necessary to rescale the spectra by a factor of 0.96. The optimal cluster (d) represents the measured spectra very well. The experimental spectrum exhibits four main bands which lie between  $1330\text{ cm}^{-1}$  and  $1500\text{ cm}^{-1}$ ,  $1150\text{ cm}^{-1}$  and  $1300\text{ cm}^{-1}$ ,  $915\text{ cm}^{-1}$  and  $1150\text{ cm}^{-1}$ , and between  $650\text{ cm}^{-1}$  and  $770\text{ cm}^{-1}$ . These four bands are well captured by according vibrational modes in the calculated spectrum. Even the relative intensities agree well with the measured ones.

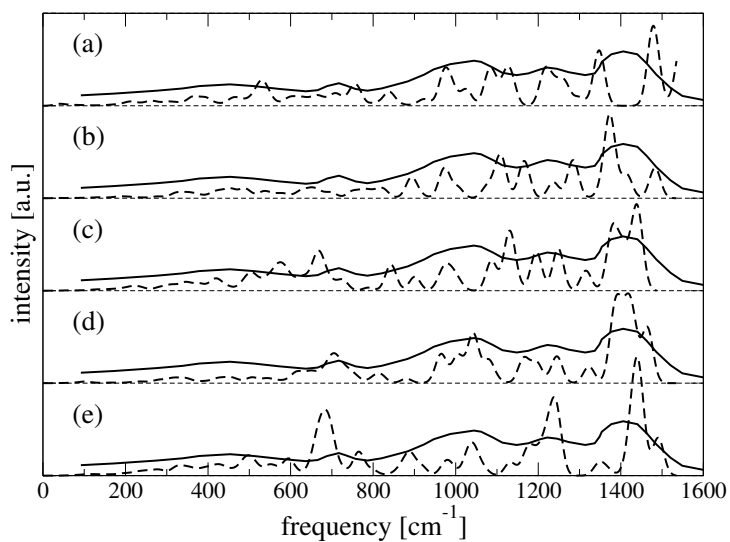


Figure 23: Comparison of 5 calculated IR spectra for  $\text{Li}_2\text{O-B}_2\text{O}_3$  clusters with experimental IR data.

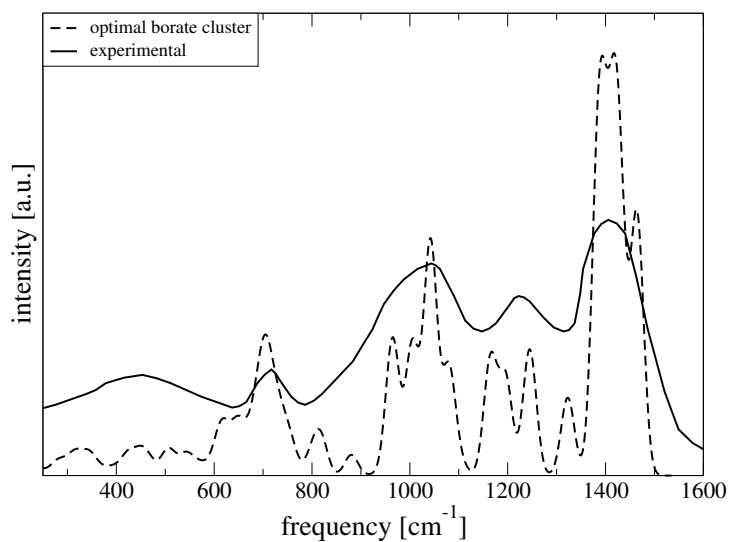


Figure 24: Comparison of the calculated IR spectra for the optimal  $\text{Li}_2\text{O-B}_2\text{O}_3$  clusters with experimental IR data.

Table 7: Bond lengths in LISON in Å. The Crystal data is that of a  $\text{Li}_2\text{SO}_4 \cdot \text{H}_2\text{O}$  crystal as reported by A. Larson [56].

Type	DFT	Crystal
S-O	$1.52 \pm 0.03$	1.48
O-O	$2.48 \pm 0.02$	2.40
Li-O	$1.95 \pm 0.04$	1.95
N-S	$1.60 \pm 0.06$	
N-N	$1.44 \pm 0.06$	
N-Li	$2.03 \pm 0.09$	
N-O	$2.57 \pm 0.06$	

## 4.7 Structural properties

### 4.7.1 LISON and the role of nitrogen

Figure 25 shows the radial distribution function (RDF) of the LISON clusters. The various contributions to the RDF are colour-coded and the most important peaks are labelled. In table 7 the bond lengths for LISON are listed, as obtained from the first neighbour shell peaks in the RDF. In addition the bond lengths as found in crystalline  $\text{Li}_2\text{SO}_4$  are given as reported by A. Larson [56]. One particular interesting feature of many LISON clusters is that they have a nitrogen-nitrogen bond which forms a bridge between two neighbouring  $\text{SO}_3\text{N}^{2-}$  anions. This is remarkable as these bonds are the result of the geometry optimisation and were not present in the initial configurations. Indeed the tendency to form such nitrogen bridges is rather strong. Table 8 shows that in 75% of the cases where two nitrogen atoms were closer than 3.5 Å in the initial configurations, nitrogen-nitrogen bonds form in the cause of the geometry optimisation. The corresponding bond length is  $1.47 \pm 0.01$  Å with one notable exception where a bond length of 1.30 Å occurred.

This observation explains why nitrogen incorporation allows the formation of an amorphous film from a  $\text{Li}_2\text{SO}_4$  target by sputtering. By connecting  $\text{SO}_3\text{N}^{2-}$  anions their reorientation and therefore a crystallisation of the film is hindered. It is possible that a network forms when the nitrogen content is high enough.

### 4.7.2 $\text{Li}_2\text{O-B}_2\text{O}_3$

Figure 27 shows the radial distribution function (RDF) of clusters which were saturated with hydrogen. The various contributions to the total RDF are coloured. A closer inspection of the boron-oxygen distances (see fig. 28) reveals that the hydrogen saturation is a good replacement for a continues

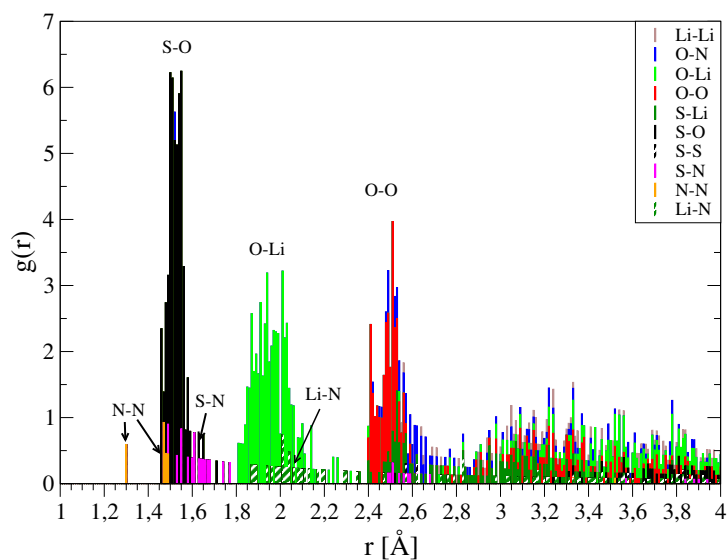


Figure 25: Radial distribution function of LISON.

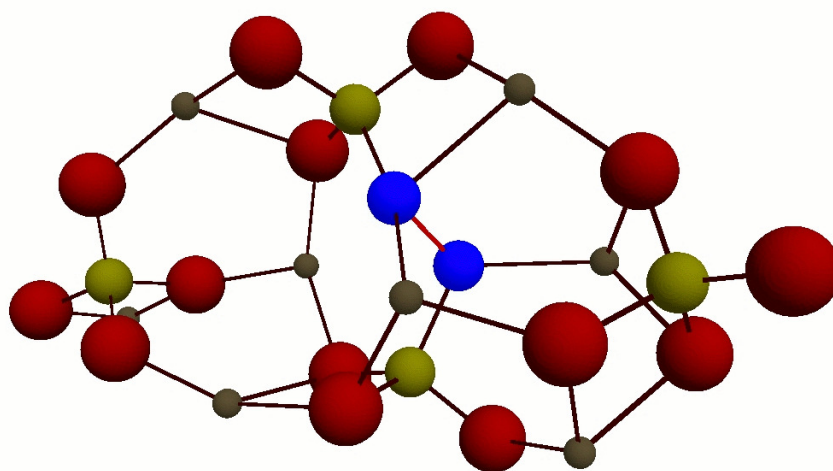


Figure 26: Atomic configuration of the optimal LISON cluster (corresponding to spectrum 1 in fig. 21). Oxygen atoms are marked in red (dark grey, large spheres), sulphur atoms in yellow (light grey, mid-size spheres), nitrogen atoms in blue (dark grey, mid-size spheres), and lithium atoms in silver (grey, small spheres).

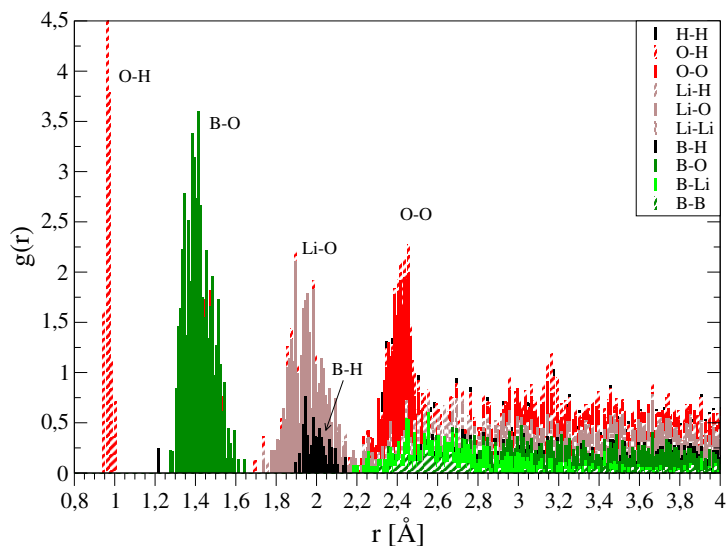


Figure 27: Radial distribution function of lithium borate clusters saturated with hydrogen.

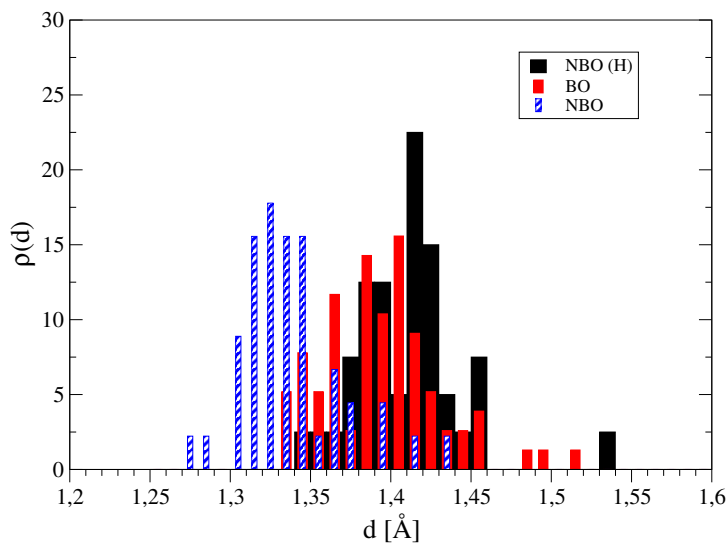


Figure 28: Bond length distribution of boron-oxygen bonds involving trigonal coordinated boron atoms  $[\text{BO}_3]$  in hydrogen saturated clusters. The abbreviations stand for: NB non-bridging; B bridging; H the oxygen atom has a bond to a hydrogen atom.

Table 8: Nitrogen-nitrogen distances before ( $d_0$ ) and after the geometry optimisation ( $d_{\text{end}}$ ).

Cluster-ID	N-Pair	$d_0$	$d_{\text{end}}$
LISON-4 (1-2)	1-17	3.214	1.470
LISON-4 (1-4)	1-23	4.288	3.105
LISON-4 (4-1)	1-17	7.245	6.796
LISON-4 (4-2)	6-18	5.233	4.630
LISON-8 (6-1)	54-55	3.11	1.465
LISON-8 (6-1)	52-53	2.69	3.513
LISON-8 (6-2)	53-54	3.320	3.323
LISON-8 (6-2)	52-55	3.171	1.298
LISON-8 (7-1)	54-55	3.430	1.485
LISON-8 (7-1)	52-53	3.163	1.466
LISON-8 (7-2)	48-49	3.133	1.478
LISON-8 (7-2)	51-50	7.020	7.122

network. Broken down into bonds involving tetrahedral coordinated boron [BO4] and trigonal coordinated boron atoms [BO3], the distribution of interatomic distances shows that non-bridging oxygen atoms (NBO) with a bond to a hydrogen atom have similar bond lengths ( $1.41 \pm 0.03$  Å [BO3];  $1.49 \pm 0.05$  Å [BO4]) to the boron atoms as bridging oxygen (BO) atoms ( $1.39 \pm 0.04$  Å [BO3];  $1.50 \pm 0.05$  Å [BO4]). In contrast NBO atoms without a saturating hydrogen atom have much shorter bonds to boron atoms ( $1.34 \pm 0.03$  Å [BO3];  $1.41 \pm 0.05$  Å [BO4]). This shows that the hydrogen atoms allow connected oxygen atoms to act as if they were incorporated into a continued network. Furthermore, these bond lengths are in agreement with data obtained from MD-simulations where the average bond lengths are  $1.37$  Å [BO3] and  $1.48$  Å [BO4]. These numbers are also in agreement with bond lengths in lithium borate crystals, where bond lengths of  $1.37$  Å [BO3] and  $1.49$  Å [BO4] have been reported [57].

In case of the clusters with a negative net charge as saturation scheme, the bond lengths suggest that the additional electron density is distributed over the whole cluster, instead of being localised on its surface as a replacement for a continued network. All bond lengths are increased by roughly  $0.4$  Å compared to the bond lengths found in the clusters which were saturated with hydrogen. The non-bridging oxygens have bond lengths of  $1.37 \pm 0.05$  Å [BO3] and the bridging oxygens have bond lengths of  $1.44 \pm 0.05$  Å [BO3]. Considering the numbers obtained for the crystalline system, these bond lengths suggest that a negative net charge is not suitable for taking into account the effect of the surrounding network. In table 9 the

## 4 AB INITIO CALCULATIONS

---

Table 9: Bond lengths in  $\text{Li}_2\text{O-B}_2\text{O}_3$  for hydrogen saturated clusters (DFT-H), clusters with a negative net-charge (DFT-e), MD data is taken from a simulation using the same procedure as presented in sec. 2.1.3 and the potential model of [15]. The crystal data is taken from [57]. The bond-type abbreviations stand for: BO3 trigonal coordinated boron; BO4 tetrahedral coordinated boron; BO bridging oxygen; NBO non-bridging oxygen; H the oxygen has a bond to a hydrogen.

Bond-type	DFT-H	DFT-e	MD	Crystal
B-O [BO3] BO	$1.39 \pm 0.04$	$1.44 \pm 0.05$	1.37	1.37
B-O [BO3] NBO-H	$1.41 \pm 0.03$			
B-O [BO4]	$1.49 \pm 0.05$		1.48	1.49
B-O [BO4] NBO-H	$1.50 \pm 0.05$			
B-O [BO3] NB	$1.34 \pm 0.03$	$1.37 \pm 0.05$		
B-O [BO4] NB	$1.41 \pm 0.05$			
Li-O	$1.96 \pm 0.09$	$1.92 \pm 0.06$		1.97
O-O	$2.41 \pm 0.06$	$2.41 \pm 0.05$		2.41

bond length comparison is summarised.

---

## 5 Summary and Outlook

### 5.1 Summary

This work presents the results of the agreement of diffusion paths in ion-conducting glasses determined by molecular dynamics (MD) simulations and bond valence (BV) calculations for a lithium silicate glass. Furthermore, it is shown that ab initio calculations of glassy clusters can reproduce experimental Raman and infrared spectra. This confirms that such clusters can be used for the development of effective force fields for MD or Monte-Carlo (MC) calculations.

Sites and diffusion paths for the mobile Li ions in the MD-simulations were identified based on a cluster analysis of the Li number density  $\rho(\mathbf{x})$ . It is shown that there exist sharp local maxima in  $\rho(\mathbf{x})$  which form the core of sites. While they only contain 1.4% of the system volume, the Li ions spend 75% of the time on them. By including intermediate escapes to the surrounding of the clusters, the total residence time on clusters was calculated. Clusters where the total residence time of a Li ion is ten times larger than the total hopping time to neighbouring clusters were assigned to be sites. Using this criterion, the concentration of vacant sites is 9%.

Then diffusion paths were determined by BV calculations following the original and a slightly altered BV scheme. A comparison with the MD paths showed that up to 50% of the MD diffusion path are captured (including most of the sites) by the BV paths. The quality of agreement could not be enhanced significantly by using the altered BV scheme. Furthermore, it is shown that most of the agreement between MD path and BV path is due to geometric constraints included in the BV scheme which correspond to a hard sphere model. An attempt to identify sites with the BV method revealed that it cannot distinguish between regions of high and low  $\rho(\mathbf{x})$  (see also fig. 14), and accordingly is not suitable to determine the sites.

Hartree Fock and density functional theory calculations of glassy LISON and lithium borate clusters were performed using the 6-31G\* basis set and in the case of DFT calculations the B3LYP functional was used. The calculated vibrational spectra of many configurations do not compare well with experimental data. This is due to the lack of a defined method to produce start configurations which are close enough to a good representation of the local structure of the real glass system. It is necessary to have such start configurations as in the case of the geometry optimisation routines only the next minimum is found. Nevertheless, the calculated vibrational spectra of some clusters compare well with experimental spectra. Additionally, structural data of the DFT clusters is compared to that of corresponding crystalline systems.

An investigation of the LISON structures reveals that nitrogen is replacing oxygen in the  $\text{SO}_4^{2-}$  tetrahedra. In the configurations that result in

Raman spectra in agreement with the experimental data we find nitrogen-nitrogen bridges between anions. This might be the underlying reason for the prevention of crystallisation of the LISON material during the sputtering process, as these nitrogen bridges restrain the reorientation of the anions and therefore stabilise an amorphous film structure.

## 5.2 Outlook

Most effective force fields for MD or MC simulations of glass systems are either phenomenological or were derived from ab initio calculations involving only a single basic unit of the glass structure. In contrast, cluster calculations, as the one presented in this work, can reproduce local structures of glass systems as well as their vibrational spectra. Potentially, this allows the derivation of effective force fields where not only nearest neighbour interactions but also the local structure is accounted for. This may also enable the direct development of potential models for more complex glasses which are of great interest for many applications.

One approach to derive potential parameters is to use direct parameter fitting. To this end one has to scan a part of the potential energy landscape (PES) around the minima in which the cluster configurations are. An effective way is probably to elongate the cluster  $i$  from its minimum configuration  $\mathbf{Q}_i$  along the normal vectors  $\mathbf{q}_{i,\nu}$  of the vibrational normal modes  $\nu$  and calculate the energy of these perturbed configurations within the framework of ab initio calculations ( $E_{AI}$ ) and according to a chosen effective force field model ( $E_{EFF}$ ). While one could in principle also use the force constants of the normal modes to calculate force field parameters, calculating the energy at several points along a normal vector ( $d\mathbf{q}_{i,\nu}$ ) potentially accounts for higher order terms of the PES. In the end the problem of finding optimal parameters  $\alpha_k$  for the force field model is a classical minimisation problem:

$$\sum_{i,\nu,d} [E_{AI}(\mathbf{Q}_i + d\mathbf{q}_{i,\nu}) - E_{EFF}(\mathbf{Q}_i + d\mathbf{q}_{i,\nu}, \alpha_k)]^2 \longrightarrow \min . \quad (69)$$

A further refinement could be to introduce weighing factors for the various normal modes. For example one could try to minimise the effect of the cluster surface by giving lower weights to vibrations which involve surface atoms moving along the normal vector of the surface.

This approach also allows for the development of effective force fields for systems where no suitable experimental data is available in order to derive potential parameters (e.g. LISON). Moreover, it is our hope that effective force fields derived in this way allow for quantitatively more accurate MD-simulation than the available force fields. Through analysis of the dynamics in such simulations it may be possible to develop quantitative coarse grained models for the conductivity in ion-conducting glasses. Through investigations as the one described in sec. 2.2 one can for example determine

elementary hopping rates between ion sites which in turn could be used in subsequent Monte-Carlo simulations which already allow for a qualitative description of conductivity effects as the MAE [58]. In the near future such a combination of methods may allow for a consistent multi-scale modelling of complex amorphous systems, bridging length scales from Ångstroms to micrometers and time scales of femto-seconds to seconds.

## A List of clusters

Table 10: List of all produced configurations which converged at least at a HF/6-31G\* level of theory. The start configurations were either produced with GaussView (GV) or taken from MD-simulations (MD). The cpu-hours used for the calculations are listed as well as the number of iterations in the various geometry optimisation runs. Some data is missing due to interrupted runs and therefore corrupted logs.

\* no HF/6-31G\* optimisation was performed.

Cluster	# atoms	start-conf.	HF		DFT	
			cpuh	iter.	cpuh	iter.
Li <sub>2</sub> SO <sub>4</sub> -4 (4)	28	GV	150	190	51	26
LISON-4 (1-2)	28	GV	27	34	16	
LISON-4 (1-4)	28	GV	64	88	12	
Li <sub>2</sub> SO <sub>4</sub> -4 (4)	28	GV	150	190	51	26
LISON-4 (4-1)	28	GV	132	109	22	
LISON-4 (4-2)	28	GV	92	72	22	
Li <sub>2</sub> SO <sub>4</sub> -8 (6)	56	GV	1094	202	1112	58
LISON-8 (6-1)	56	GV	1970	236	1064	56
LISON-8 (6-2)	56	GV			1673	85
Li <sub>2</sub> SO <sub>4</sub> -8 (7)	56	GV				
LISON-4 (7-1)	56	GV			2377	215
LISON-4 (7-2)	56	GV			3552	267
LiBO <sub>2</sub> -6 (1-e)	26	GV	43	259	24	14
LiBO <sub>2</sub> -6 (1-H)	30	GV	35	132	18	10
LiBO <sub>2</sub> -7 (2-e)	31	GV	45	177	22	18
LiBO <sub>2</sub> -7 (2-H)	37	GV	50	186	35	33
LiBO <sub>2</sub> -7 (3-e)	33	MD		201		
LiBO <sub>2</sub> -7 (3-H)	43	MD		229	90	150
LiBO <sub>2</sub> -20 (4-H)	112	MD	1085	368	~4000	153*
LiBO <sub>2</sub> -21 (5-H)	112	MD	~2000	249	~6000	183*
LiBO <sub>2</sub> -22 (6-H)	109	MD	~3000	507	~5000	162*

---

## B References

### References

- [1] K. H. Joo, P. Vinatier, B. Pecquenard, A. Levasseur, and H. J. Sohn, *Solid State Ionics* **160**, 51 (2003).
- [2] K. H. Joo, H. J. Sohn, P. Vinatier, B. Pecquenard, and A. Levasseur, *Electrochem. and Solid State Lett.* **7** [8], A256 (2004).
- [3] W. Dieterich and P. Maass, *Chem. Phys.* **284**, 439 (2002).
- [4] H. Lammert, M. Kunow, and A. Heuer, *Phys. Rev. Lett.* **90**, 215901 (2003).
- [5] J. Habasaki and Y. Hiwatari, *Phys. Rev. B* **69**, 144207 (2004).
- [6] M. Vogel, *Phys. Rev. B* **70**, 094302 (2004).
- [7] H. Lammert, A. Heuer, *Phys. Rev. B* **70**, 024204 (2004).
- [8] A. Heuer, H. Lammert, M. Kunow, *Z. Phys. Chem.* **218**, 1429(2004).
- [9] H. Lammert, A. Heuer, *Phys. Rev. B* **72**, 214202 (2005).
- [10] J. Habasaki and K. L. Ngai, *J. Chem. Phys.* **122**, 214725 (2005).
- [11] S. Adams and J. Swenson, *Phys. Rev. Lett.* **84**, 4144 (2000).
- [12] J. Swenson and S. Adams, *Phys. Rev. Lett.* **90**, 155507 (2003).
- [13] A. Hall, S. Adams, and J. Swenson, *Ionics* **10**, 396 (2004).
- [14] S. Adams and J. Swenson, *J. Phys.: Condensed Matter* **17**, 87 (2005).
- [15] C.-P. Varsamis, A. Vegiri, and E. I. Kamitsos, *Phys. Rev. B* **65**, 104203 (2002).
- [16] L. Verlet, *Phys. Rev.* **159**, 98 (1967)
- [17] W. Swope, H. Andersen, P. Berens, and K. Wilson, *J. Chem. Phys.* **76**, 637 (1982)
- [18] S. Nos, *Mol. Phys.* **52**, 255 (1984)
- [19] W. G. Hoover, *Phys. Rev. A* **31**, 1695 (1985)
- [20] L. Woodcock, C. Angell, and P. Cheeseman, *J. Chem. Phys* **65** [4], 1565 (1976)

## REFERENCES

---

- [21] S. Tsuneyuki, M. Tsukada, H. Aoki, and Y. Matsui, Phys. Rev. Let. **61** [7], 869 (1988)
- [22] B. W. H. van Beest, G. J. Kramer, and R. A. van Santen, Phys. Rev. Let. **64** [16], 1955 (1988)
- [23] J. Habasaki and I. Okada, Molecular Simulation **9**, 319 (1992).
- [24] T. F. Soules, J. Chem. Phys. **49**, 4032 (1980).
- [25] A. H. Verhoef and H. W. den Hartog, J. Non Cryst. Solids **182**, 221 and 235 (1995).
- [26] S. J. Plimpton, J. Comp. Phys. **117**, 1 (1995)
- [27] <http://lammps.sandia.gov/>
- [28] J. Habasaki, I. Okada, Y. Hiwatari, J. Non-Cryst. Solids **183**, 12 (1995).
- [29] R.D. Banhatti and A. Heuer, Phys. Chem. Chem. Phys. **3**, 5104 (2001).
- [30] A. Heuer, M. Kunow, M. Vogel, R.D. Banhatti, Phys. Chem. Chem. Phys. **4**, 3185 (2002).
- [31] The  $r^{-6}$  dependence can be motivated by the van-der-Waals interaction. However, since this term is used both for distances corresponding to covalent bonding as well as large distances, it in fact is not a van-der Waals interaction and often referred to as 'dispersive interaction'. Nevertheless, the amplitude factors  $c_i$ ,  $c_j$  are usually assumed to scale with the polarisabilities. This gives reason to include this term here only for the large oxygen ions.
- [32] J. Hoshen and R. Kopelman, Phys. Rev. B **14**, 3438 (1976).
- [33] L. Pauling, *The nature of chemical bond*, Cornell, (1967).
- [34] G. Donnay and R. Allman, Am. Mineral. **55**, 1003 (1970).
- [35] M.P. Allen and D.J. Tildesley, *Computer Simulation of Liquids*, Oxford University Press, New York, (1987).
- [36] Stefan Adams, Bindungswalenzmodelle für Struktur-Leitfähigkeits-Beziehungen in Festelektrolyten, habilitation thesis, Göttingen 2000.
- [37] <http://kristall.uni-mki.gwdg.de/softBV/>
- [38] In other BV studies an additional 'sign criterion' is often used in order to avoid an erroneous classification due to the limited cell resolution. In this case a cell is also marked as accessible if a Li ion at its centre fails to fulfil requirement (iii), but on the other hand  $d(\mathbf{x})$  at one of the

- centres of the nearest neighbouring cells has opposite sign. However, in our case the cell resolution is fine enough so that this problem plays no role for all relevant  $d_{\text{th}}$  considered in the subsequent analysis.
- [39] S. Adams, Proceedings of the Asian Solid State Ionics Conference, AC-SSI X, Kandy, Sri Lanka, 2006.
- [40] This definition of specificity deviates from the usual one, as it is, for example, often applied in medical studies. In such studies the specificity is given by the conditional probability  $\psi(\bar{\mathcal{P}}_{\star}^{\text{BV}}|\bar{\mathcal{P}}_{\star})$  with  $\bar{\mathcal{P}}_{\star}^{\text{BV}}$  and  $\bar{\mathcal{P}}_{\star}$  being the complements of  $\mathcal{P}_{\star}^{\text{BV}}$  and  $\mathcal{P}_{\star}$ , respectively. Both definitions are related by  $\psi(\mathcal{P}_{\star}|\mathcal{P}_{\star}^{\text{BV}}) = \psi(\mathcal{P}_{\star})\psi(\mathcal{P}_{\star}^{\text{BV}}|\mathcal{P}_{\star})/[\psi(\mathcal{P}_{\star})\psi(\mathcal{P}_{\star}^{\text{BV}}|\mathcal{P}_{\star}) + (1 - \psi(\mathcal{P}_{\star}))(1 - \psi(\bar{\mathcal{P}}_{\star}^{\text{BV}}|\bar{\mathcal{P}}_{\star})]$ , where  $\psi(\mathcal{P}_{\star})$  is the probability that a cell belongs to  $\mathcal{P}_{\star}$  (i.e. equal to the volume fraction given in table 4).
- [41] A. Hall, St. Adams, and J. Swenson, Phys. Rev. B **74** [17], 174205 (2006).
- [42] L. Fleiss, *Statistical methods for rates and proportions*, 2nd ed., Wiley & Sons, New York, (1981) pp. 212-236.
- [43] E. Cazzanelli and R. Frech, J. Chem. Phys. **79**, 2615 (1983); *ibid.* **81**, 4729 (1984); only the modes belonging to the  $A_g$  symmetry are considered (other representations have slightly shifted modes, but the size of the corresponding shifts are negligible in comparison with the width of the peaks obtained for the film).
- [44] E. K. U. Gross, E. Runge, and O. Heinonen, *Many-Particle Theory*, Adam Hilger, Bristol (1991).
- [45] C. J. Cramer, *Essentials of Computational Chemistry*, 2nd ed., Wiley & Sons, Hoboken, New Jersey (2004).
- [46] T. Uchino and T. Yoko, J. Chem. Phys. **105** [10], 4140 (1996).
- [47] T. Uchino and T. Yoko, Solid State Ionics **105**, 91 (1998).
- [48] R. M. Van Ginhoven, H. Jonsson and L. R. Corrales, Phys. Rev. B **71**, 024208 (2005).
- [49] J. Du and L. R. Corrales, J. Chem. Phys. **125**, 114702 (2006).
- [50] J. C. Mauro and A. K. Varshneya, J. Am. Ceram. Soc. **89** [7], 2323 (2006).
- [51] GaussView, Version 3.09, R. Dennington II, T. Keith, J. Millam, K. Eppinnett, W. L. Hovell, and R. Gilliland, Semichem, Inc., Shawnee Mission, KS, 2003.

## REFERENCES

---

- [52] Gaussian 03, Revision C.02, M. J. Frisch, G. W. Trucks, H. B. Schlegel, G. E. Scuseria, M. A. Robb, J. R. Cheeseman, J. A. Montgomery, Jr., T. Vreven, K. N. Kudin, J. C. Burant, J. M. Millam, S. S. Iyengar, J. Tomasi, V. Barone, B. Mennucci, M. Cossi, G. Scalmani, N. Rega, G. A. Petersson, H. Nakatsuji, M. Hada, M. Ehara, K. Toyota, R. Fukuda, J. Hasegawa, M. Ishida, T. Nakajima, Y. Honda, O. Kitao, H. Nakai, M. Klene, X. Li, J. E. Knox, H. P. Hratchian, J. B. Cross, V. Bakken, C. Adamo, J. Jaramillo, R. Gomperts, R. E. Stratmann, O. Yazyev, A. J. Austin, R. Cammi, C. Pomelli, J. W. Ochterski, P. Y. Ayala, K. Morokuma, G. A. Voth, P. Salvador, J. J. Dannenberg, V. G. Zakrzewski, S. Dapprich, A. D. Daniels, M. C. Strain, O. Farkas, D. K. Malick, A. D. Rabuck, K. Raghavachari, J. B. Foresman, J. V. Ortiz, Q. Cui, A. G. Baboul, S. Clifford, J. Cioslowski, B. B. Stefanov, G. Liu, A. Liashenko, P. Piskorz, I. Komaromi, R. L. Martin, D. J. Fox, T. Keith, M. A. Al-Laham, C. Y. Peng, A. Nanayakkara, M. Challacombe, P. M. W. Gill, B. Johnson, W. Chen, M. W. Wong, C. Gonzalez, and J. A. Pople, Gaussian, Inc., Wallingford CT, 2004.
- [53] A. P. Scott and L. Radom, *J. Phys. Chem.*, **100**, 16502 (1996).
- [54] Y. Hamon and P. Vinatier, private communication.
- [55] E. I. Kamitsos and G. D. Chryssikos, *J. Mol. Struct.* **247**, 1 (1991).
- [56] A. Larson, *Acta Cryst.* **18**, 717 (1965).
- [57] D. Louer, M. Louer, and M. Touboul, *J. Appl. Cryst.* **25**, 617 (1992).
- [58] R. Peibst, St. Schott, and P. Maass, *Phys. Rev. Lett.* **95**, 115901 (2005).

---

## C Publications and conference contributions

1. **Comparison of Ionic Sites and Diffusion Paths obtained by Molecular Dynamics Simulations and Bond Valence Analysis**  
C. Müller, E. Zienicke, St. Adams, J. Habasaki, and P. Maass,  
Phys. Rev. B **75**, 14203 (2007).
2. **Structure of Glassy Lithium Sulfate Films Sputtered in Nitrogen (LISON): Insight from Raman Spectroscopy and Ab Initio Calculations**  
C. R. Müller, P. Johansson, M. Karlsson, P. Maass, and A. Matic,  
arXiv:0706.2961 (2007) *preprint*
3. Talk: **Theory on Ion Conducting Glasses: Towards Multiscale Modeling**  
Christian Müller and Philipp Maass  
HI-CONDELEC steering committee meeting 2007, Helsinki
4. Talk: **Ab-initio calculations of atomic cluster configurations for ion conducting glasses**  
Christian Müller and Philipp Maass  
DPG Frühjahrstagung 2007, Regensburg
5. Talk: **Ab-initio Calculations**  
Christian Müller, Aleksandar Matic, and Patrick Johansson  
HI-CONDELEC steering committee meeting 2006, Athen
6. Poster: **Identification of Ion Sites in Glasses**  
Christian Müller, Hartmut Grille, Junko Habasaki, and Philipp Maass  
DPG Frühjahrstagung 2005, Berlin

## D Acknowledgment

Here I want to thank Prof. Philipp Maaß for his mentoring and the many intriguing discussions about physics.

I want to express my gratitude to Prof. Erich Runge, who was not only always able to spark interest in for me unknown problems in physics, but also agreed to be part of the examining committee.

I want to thank Aleksandar Matic and Patrik Johansson for the possibility to spend my internship at the Chalmers University, Göteborg, where I started to work on the ab initio cluster calculations.

I want to thank Egbert Zienicke, Stefan Adams, Junko Habasaki, and Maths Karlsson for their cooperation in parts of this work.

Next, I thank Wichard Beenken for the many fruitful and interesting discussions, especially concerning the MAPACC cluster.

I also want to thank Steffi Trott for eliminating the worst cases of 'denglish' in the early versions of this work, as well as proofreading it in its final state.

I am very grateful to all my colleagues of the two departments for theoretical physics at the TU Ilmenau and of the department for condensed matter physics at the Chalmers University.

And last but not least I thank my family for their continued support and love.

---

## **E Erklärung**

Hiermit erkläre ich, dass ich diese Arbeit selbstständig durchgeführt und abgefasst habe. Quellen, Literatur und Hilfsmittel, die von mir benutzt wurden, sind als solche gekennzeichnet.